Simultaneous multimodal imaging of metabolic and functional parameters of tumors; tumor heterogeneity, prediction of precision medicine effectiveness by radiomic analysis and machine learning algorithms

Nesrin Mansouri

Université Paris Cité

Université Paris Cité

École doctorale [Médicament, Toxicologie, Chimie, Imageries (MTCI), ED 563]

Paris-Centre de Recherche Cardiovasculaire, Inserm U970

Simultaneous multimodal imaging of metabolic and functional parameters of tumors; tumor heterogeneity, prediction of precision medicine effectiveness by radiomic analysis and machine learning algorithms

Par Nesrin MANSOURI

Thèse de doctorat de Imageries

Dirigée par Bertrand TAVITIAN

& Co-encadrant Mailyn Perez-Liva

Présentée et soutenue publiquement le 19/12/2023

Devant un jury composé de :

Angel ALBERICH, Prof.	Polytechnic University of Valencia	Rapporteur
Beatrice BERTHON, PhD-HDR	PSL Université Paris	Rapportrice
Jean Emmanuel BIBAULT, PhD-HDR	Université Paris Cité	Examinateur
Charlotte LUSSEY, Docteur en Medecine	Sorbonne Université	Examinatrice
Joaquin L. HERRAIZ, Full Prof.	Complutense University of Madrid	Examinateur
Laure FOURNIER, PH-HDR	Université Paris Cité	Examinatrice
Bertrand TAVITIAN, PH-HDR	Université Paris Cité	Directeur
Mailyn PEREZ LIVA, PhD	Complutense University of Madrid	Membre Invité et Co-Encadrant

Résumé

Titre: Imagerie multimodale simultanée des paramètres métaboliques et fonctionnels des tumeurs : hétérogénéité tumorale, prédiction de l'efficacité de la médecine de précision par algorithmes d'apprentissage automatique.

Mots clefs: *Imagerie multimodale, Apprentissage automatique, Paragangliome, Réponse au traitement, Tomographie par émission de positons dynamique (TEP), Doppler ultrasonore ultrarapide, Regroupement hiérarchique, Hétérogénéité intra-tumorale, Réseau de neurones U-Net.*

Résumé: *Traditionnellement, l'évaluation de l'efficacité des traitements s'est principalement appuyée sur les caractéristiques macroscopiques des tumeurs, telles que la taille ou la glycolyse, ce qui n'offre qu'un aperçu indirect des effets des thérapies de précision sur la biologie des tumeurs. Les modalités d'imagerie avancées offrent de nouvelles possibilités de visualiser des caractéristiques tumorales distinctes et d'extraire des descripteurs, améliorant ainsi notre compréhension de la réponse au traitement. En particulier, l'imagerie multimodale joue un rôle clé en permettant l'intégration de diverses techniques pour obtenir une vue d'ensemble détaillée du comportement de la tumeur.*

Notre étude présente un nouveau cadre d'apprentissage automatique qui exploite les caractéristiques d'imagerie métabolique, morphologique et vasculaire obtenues par tomographie par émission de positrons (TEP), échographie Doppler ultrarapide (UUDI) et tomodensitométrie (TDM). Ces caractéristiques ont été extraites et analysées à l'aide d'une analyse hiérarchique des grappes (HCA) dans un modèle murin de paragangliome traité avec le médicament anti-angiogénique sunitinib. Le modèle comprenait des souris traitées au sunitinib et des souris traitées au placebo, imagées à intervalles réguliers pour surveiller la réponse au traitement. Le HCA a classé les réponses en trois étapes, validées à l'aide d'un ensemble de données indépendantes. Le classificateur gaussien naïf de Bayes s'est avéré être le classificateur d'apprentissage automatique le plus performant, atteignant une précision d'apprentissage remarquable de 98,7%. Ces résultats soulignent le potentiel de la combinaison des marqueurs métaboliques, morphologiques et vasculaires pour redéfinir les trajectoires de réponse au traitement.

Au-delà de l'évaluation du traitement, notre recherche explore le paysage complexe de l'hétérogénéité intra-tumorale. Les tumeurs présentent diverses sous-régions avec des caractéristiques distinctes, ce qui nécessite des techniques d'imagerie non invasives. Notre approche implique un regroupement au niveau de l'individu et de la population, guidé par les caractéristiques réalistes de la dynamique moléculaire multimodale (TEP) et de l'imagerie vasculaire UUDI. En outre, un réseau neuronal 3D U-Net a identifié de manière autonome les sous-régions liées à la résistance au sunitinib, catégorisant avec succès les tumeurs en quatre sous-régions intra-tumorales distinctes, chacune présentant des profils métaboliques et vasculaires uniques. L'une de ces sous-régions a permis de prédire la résistance au traitement à un stade avancé avec une précision moyenne du coefficient de Dice de 85,37 %. Cette méthodologie innovante automatise l'identification des

sous-régions prédictives, ce qui nous permet de mieux comprendre l'impact de l'hétérogénéité intra-tumorale sur l'évaluation des traitements. L'analyse radiomique a été utilisée pour redéfinir les stades de réponse au traitement dans les groupes de contrôle et les groupes traités par le sunitinib et pour extraire les marqueurs des régions associées à la réponse au traitement. Les caractéristiques radiomiques ont permis de mieux comprendre les caractéristiques métaboliques et vasculaires, offrant une vision globale de l'hétérogénéité intra-tumorale au-delà des mesures traditionnelles. Par conséquent, l'analyse radiomique enrichit notre compréhension des réponses au traitement, positionnant la radiomique comme un complément précieux dans la médecine de précision pour les paragangliomes..

En conclusion, cette recherche fait progresser notre compréhension de la réponse au traitement du cancer, en tirant parti de l'imagerie avancée et de l'apprentissage automatique pour obtenir des informations précises. Elle identifie des sous-régions prédictives au sein des tumeurs et s'avère ensuite prometteuse pour les thérapies anticancéreuses personnalisées, faisant le lien entre la médecine conventionnelle et la médecine de précision afin d'améliorer potentiellement les résultats pour les patients.

Title: Simultaneous multimodal imaging of metabolic and functional parameters of tumors; tumor heterogeneity, prediction of precision medicine effectiveness by radiomic analysis and machine learning algorithms.

Keywords: *Multi-modal imaging*, *Machine learning*, *Paraganglioma*, *Treatement response*, *Dynamic Positron Emission Tomography (PET)*, *Ultrasound Ultrafast Doppler*, *Hierarchical clustering*, *Intra-tumor heterogenity*, *U-Net neural network*

Abstract: Traditionally, evaluating treatment efficacy has relied mainly on gross tumor features like size or glycolysis, offering only indirect insights into the effects of precision therapies on tumor biology. Advanced imaging modalities present novel opportunities to visualize distinct tumor characteristics and extract descriptors, enhancing our comprehension of treatment response. Specifically, multimodal imaging plays a key role, allowing the integration of diverse techniques for a detailed overview of tumor behavior. Our study presents a novel machine learning framework that exploits metabolic, morphological and vascular imaging features obtained from positron emission tomography (PET), ultrafast Doppler ultrasound (UUDI) and computed tomography (CT). These features were extracted and analyzed using hierarchical cluster analysis (HCA) in a mouse model of paraganglioma treated with the anti-angiogenic drug sunitinib. The model included sunitinib-treated and placebo-treated mice, imaged at regular intervals to monitor response to treatment. The HCA classified responses into three stages, validated using an independent data set. Notably, Bayes' naive Gaussian classifier proved to be the best-performing machine-learning classifier, achieving a remarkable learning accuracy of 98.7%. These results underline the potential of combining metabolic, morphological and vascular markers to redefine treatment response trajectories. Beyond treatment evaluation, our research delves into the complex landscape of intra-tumoral heterogeneity. Tumors are not uniform entities; they contain diverse subregions with varying characteristics. To unravel this complexity, we used the same non-invasive imaging techniques as above. Our method involves grouping at individual and population levels, driven by realist features extracted from multimodal molecular dynamics (PET) and vascular UUDI imaging. Additionally, a 3D U-Net neural network automatically identified subregions responsible for sunitinib resistance. We successfully divided tumors into four distinct intra-tumoral subregions, each characterized by a unique metabolic and vascular profiles. One of the 4 subregions was predictive of late-stage treatment resistance, identified with an average Dice coefficient accuracy of 85.37%. This innovative methodology automates the identification of predictive subregions within tumors, enhancing our understanding of intra-tumoral heterogeneity's impact on treatment evaluation.

Beyond treatment assessment, our research explores intra-tumoral heterogeneity's intricate landscape. Tumors exhibit diverse subregions with distinct characteristics, requiring non-invasive imaging techniques as mentioned. Our approach involves individual and population-level grouping, guided by realist features from multimodal molecular dynamics (PET) and vascular UUDI imaging. Additionally, a 3D U-Net neural network autonomously identified subregions linked to sunitinib resistance, successfully categorizing tumors into four distinct intra-tumoral subregions, each with unique metabolic and vascular profiles. One of these subregions predicted late-stage treatment resistance with an average Dice coefficient accuracy of 85.37%. This innovative methodology automates predictive subregion identification, advancing our understanding of intra-tumoral heterogeneity's impact on treatment evaluation.

Radiomics analysis was employed to redefine treatment response stages in both control and sunitinib-treated groups and to extract markers from the regions assosciated with treatment response.Radiomic features provided rich insights into metabolic and vascular characteristics, offering a comprehensive view of intra-tumoral heterogeneity beyond traditional metrics. Therefore, radiomics analysis enriches our understanding of treatment responses, positioning radiomics as a valuable addition in precision medicine for paragangliomas. In conclusion, this research advances our understanding of cancer treatment response, taking advantage of advanced imaging and machine learning to obtain precise information. It identifies predictive subregions within tumors and subsequently holds promise for personalized anticancer therapies, bridging conventional and precision medicine to potentially improve patient outcomes.

Acknowledgment

I express my profound gratitude to Prof. Bertrand TAVITIAN for his unwavering support throughout my research journey. His expertise in guiding and interpreting the biological aspects of my results has enriched the depth of my work. Prof. Tavitian's generosity in sharing medical knowledge, coupled with enlightening discussions, has shaped the trajectory of my research. I am also thankful for his mentorship in academic writing, refining the clarity and precision of my publications.

I extend my deepest gratitude to Dr. Mailyn PEREZ-LIVA for her transformative mentorship over the past three years. Despite the geographical distance, her commitment and dedication have been inspirational. Her guidance and support were instrumental in translating abstract ideas into tangible research outcomes. Dr. Mailyn went above and beyond, facilitating a three-month research stint in Spain to accelerate my work. I am profoundly thankful to Prof. Joaquin for his ongoing support and insightful guidance.

Special thanks to Prof. Angel Alberich, and Prof. Beatrice BERTHON for agreeing to review my PhD thesis, reading it, and providing important remarks to help this work reach its final version. Thanks also to Profs. Jean Emmanuel BIBAULT, Charlotte LUSSEY, Joaquin L. HERRAIZ, and Laure FOURNIER for agreeing to examine this work.

First and foremost, I extend my deepest gratitude and everlasting memory to my beloved father, Dr. Atef MANSOURI. His unwavering support and encouragement from my earliest days have been my guiding light. I want to convey to him that his enduring faith in my abilities and his sacrifices have made this journey possible, as he always used to say, "If my daughter can't do it, no one can." Though he is not physically here to witness the culmination of this achievement, his spirit resonates in every chapter of my thesis. I carry forward his wisdom, resilience, and love for knowledge that he instilled in me. This accomplishment is dedicated to the memory of my father, whose influence remains alive in my heart and in the fabric of my academic pursuits.

I am profoundly thankful to my mother, who planted the seeds of love and value for education in my spirit. Her remarkable sacrifice of leaving her home and country to be by my side during the final steps of my journey speaks volumes about her unwavering support and dedication. Thanks to my fiancée for always believing in me and for being my pillar of support and for standing with me through both the successes and the hurdles. I am truly grateful to have you by my side. To my two brothers, your love and support mean the world. This PhD thesis is dedicated to you all.

Contents

List of Figures

List of Tables

List of Abbreviations

ACC Accuracy. xiv, 52, 58, 59

AI Artificial Intelligence. ix, x, xiii, 14, 20–22, 25, 34–36

AUC Area Under Curve. 32, 33, 37, 52, 58

CAD Computer Aided Diagnosis. 38

CAFs Cancer-associated fibroblasts. 2

CCC Concordance Correlation coefficient. xvii, 88, 90–92

CE contrast-enhanced. 39

CNNs Convolutional Neural Networks. 37

CT Computed Tomography. xiv, 10, 11, 13, 21–24, 29–34, 37–39, 45, 46, 48–51, 53, 54, 56, 57, 61, 64

DCE Dynamic Contrast Enhanced. 32, 33, 37

DL Deep Learning. 37

DMSO Dimethyl Sulfoxide. 43

DT Decision Tree. xiv, 52, 58, 59

ECM Extracellular Matrix. 2

FBN Fixed Bin Number. 86, 91

FBS Fixed Bin Size. 86, 91

FDG Fluorodeoxyglucose. 11, 31, 39, 40, 44, 56

GANs Generative Adversarial Networks. 17

GNB Gaussian naive Bayes. xiv, 16, 17, 52, 58, 59

GPU Graphics Processing Units. 34

HCA Hierarchical Clustering. xiv, 17, 18, 48, 51, 52, 56–58

HIF Hypoxia-Inducible Factor. 9, 10

IBSI Imaging Biomarker Standardization Initiative. 86

ICC Intraclass Correlation coefficient. xvii, 88, 90, 91

ITH Intra-Tumor Heterogeneity. 37, 38

MIBG Meta Iodo Benzyl Guanidine. 30, 31

ML Machine Learning. 14, 17–20, 23, 25, 26

MRI Magnetic Resonance Imaging. 13, 14, 21–24, 29–33, 37

MTV Metabolic Tumor Volume. 36

NCI National Cancer Institute. 22

NGTDM Neighboring Gray Tone Difference Matrix. 39

NIRF Near-Infrared Fluorescence. 29

NN Neural Network. 52

NSCLC Non-Small Cell Lung Cancer. 37–39

PBS Phosphate-Buffered Saline. 43

PCC Pheochromacytoma. 7, 9

PERCIST PET Response Criteria in Solid Tumors. 34, 61

PET Positron Emission Tomography. ix, x, xiv, 11, 13, 14, 22, 23, 25, 29, 31, 37–40, 45, 46, 49, 50, 53, 54, 57, 61, 64

PETRUS PET Registered Ultrafast Sonography. xvii, xviii, 44, 48, 49, 58, 60, 86, 89, 97

PGL Paraganglioma. ix, 7–10, 25, 26, 31, 32

PPGL Pheochromocytoma and Paraganglioma. 8, 9, 30–32

RECIST Response Evaluation Criteria in Solid Tumors. 34, 36, 61

RF Random Forest. 15, 52

ROI Region of Interest. 23, 87

SDH Succinate Dehydrogenase. 8, 9, 31

SDHB Succinate Dehydrogenase complex subunit B. 8–10, 31

SOMs Self-Organizing Maps. 17

SUV Standardized Uptake Value. 11, 36, 39, 40, 46, 49, 50, 53, 54, 56, 57

SVM Support Vector Machine. xiv, 15, 16, 52, 59

TLG Total lesion glycolysis. 36

TME Tumor Microenvironment. ix, xiii, 2–6, 25

UKCCCR United Kingdom Coordinating Committee on Cancer Research. 43

US Ultrasound. 33

UUDI Ultrafast Ultrasensitive Doppler. xvii, 25, 45–51, 53, 56, 61

VEGF Vascular Endothelial Growth Factor Receptor. 9, 10, 32, 37

VOI Receptors of Vascular Endothelial Growth Factor. 32, 48–50

WHO World Health Organization. 7, 33, 34

Chapter 1

Introduction

1.1 Background and Motivation

1.1.1 Tumor Definition

A tumor is an irregular cluster of tissue that emerges when abnormal cells in the body undergo uncontrolled growth and division. Typically, cells follow a well-regulated cycle of growth, replication, and eventual death to maintain the body's functions. However, in the case of tumors, this orderly process is disrupted, resulting in the formation of a mass of tissue referred to as a tumor. Tumors can occur in various tissues and organs throughout the body and can be broadly categorized into two types: benign and malignant. Benign tumors are not cancerous and do not invade nearby tissues or spread to other parts of the body. Malignant tumors, on the other hand, are cancerous and have the ability to invade surrounding tissues and spread to distant parts of the body through a process called metastasis.

Cancer can occur in virtually any tissue or organ in the body, and it is classified based on the type of tissue it originates from. Different types of cancer can have distinct behaviors, growth rates, and responses to treatment. Common risk factors for cancer include genetic predispositions, exposure to carcinogens (cancer-causing substances), family history of cancer, and certain lifestyle factors such as smoking, poor diet, lack of physical activity, and excessive sun exposure [4].

Cancer can have serious health consequences and may require various treatments, including surgery, radiation therapy, chemotherapy, targeted therapy, immunotherapy, and other specialized approaches. Early detection and prompt treatment can significantly improve the chances of successful outcomes for individuals diagnosed with cancer [5, 6].

1.1.2 Tumor Microenvironment (TME) composition

The TME refers to the complex and dynamic ecosystem that exists within and around a tumor mass. It consists of various components, including cancer cells, immune cells, fibroblasts, blood vessels, Extracellular Matrix (ECM), and signaling molecules. The interactions between these components play a crucial role in tumor growth, progression, and response to therapies. Key components of the TME include Fig.5.1 [7]:

1. **Cellular Components:**
    - **Cancer Cells:** The primary cells that make up the tumor mass. They have altered genetic and molecular characteristics that drive uncontrolled growth [8].
    - **Immune Cells:** These include various types of immune cells, such as T cells, B cells, macrophages, and dendritic cells. Immune cells can have both pro-tumor and anti-tumor effects depending on their activation state and interactions with cancer cells [9].
    - **Fibroblasts:** Cancer-associated fibroblasts (CAFs) are stromal cells that play a role in tissue repair and wound healing. CAFs can support tumor growth by producing growth factors that promote angiogenesis (the formation of new blood vessels) and remodeling the ECM [10].
    - **Endothelial Cells:** These form blood vessels and play a role in angiogenesis, supplying nutrients and oxygen to the tumor [7].
    - **Stem Cells:** Multipotent cells that have the potential to differentiate into various cell types and contribute to tumor heterogeneity [8].
2. **ECM:** is a complex network of proteins and carbohydrates that provide structural support to cells. It influences cell behavior, migration, invasion, and signaling. In the TME, the ECM can be altered, affecting tumor cell behavior and promoting metastasis [11].
3. **Signaling Molecules:** Various signaling molecules, such as cytokines, growth factors, and chemokines, are present in the TME. These molecules mediate interactions between different cell types and influence tumor progression and immune responses [8].
4. **Hypoxia:** Many tumors have regions of low oxygen (hypoxia) due to inadequate blood supply. Hypoxic conditions can promote tumor aggressiveness, resistance to therapy, and angiogenesis [12].

The TME is now recognized as a critical factor in cancer development and treatment. Therapies that target components of the TME, such as immune checkpoint inhibitors [13], anti-angiogenic agents [14], and drugs that inhibit specific signaling pathways [15], have shown promise in treating certain types of cancer. Understanding the intricate interactions within the TME is essential for developing more effective and personalized cancer therapies.

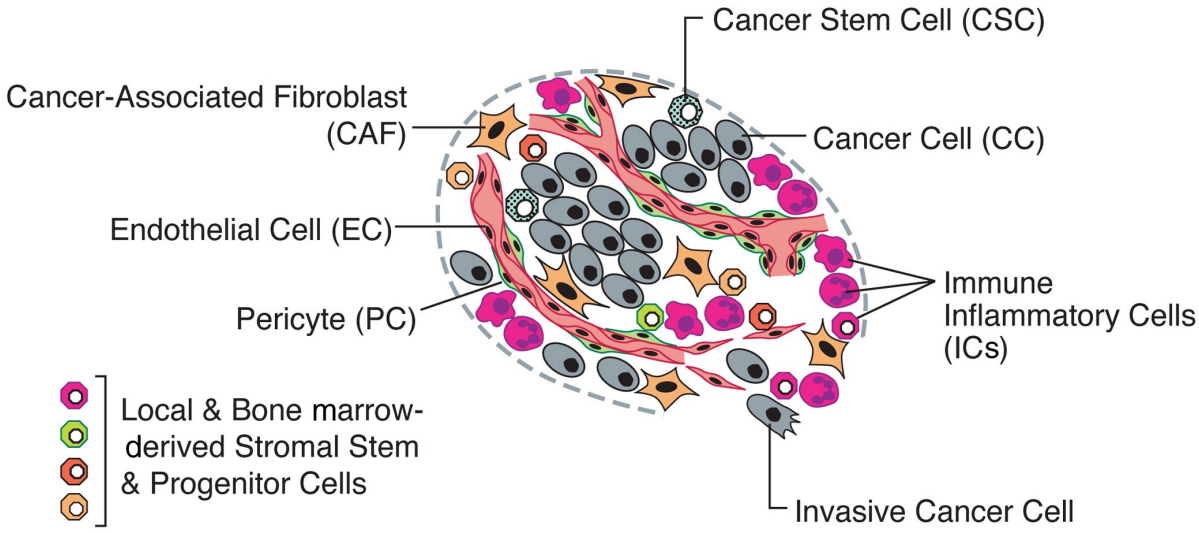

Figure 1.1: TME of cancer. Adapted from [7].

1.1.3 Hallmarks of Cancer

Cancer hallmarks are a set of distinct characteristics or biological traits that collectively define the behavior of cancer cells. These hallmarks were originally proposed by researchers Douglas Hanahan and Robert Weinberg in a seminal paper published in 2000, and they have since been expanded and refined. The hallmarks of cancer provide insights into the underlying mechanisms that drive the development and progression of malignancies. The Hallmarks of Cancer currently embody eight hallmark capabilities and two enabling characteristics [7] Figure 1.2.

- **Sustaining Proliferative Signaling:** Cancer cells often acquire mutations that allow them to continuously receive signals for growth and division, enabling them to proliferate uncontrollably.
- **Evading Growth Suppressors:** Cancer cells can evade the body's mechanisms that normally inhibit cell growth, allowing them to bypass natural checks on their proliferation.
- **Resisting Cell Death (Apoptosis):** Cancer cells can evade programmed cell death (apoptosis), a process that eliminates damaged or abnormal cells, thereby enabling their survival.
- **Enabling Replicative Immortality:** Cancer cells can maintain their ability to divide indefinitely, which is typically not possible for normal cells.
- **Inducing Angiogenesis:** Cancer cells can stimulate the formation of new blood vessels (angiogenesis) to ensure a sufficient supply of nutrients and oxygen to support their rapid growth.

- **Activating Invasion and Metastasis:** Cancer cells can invade surrounding tissues and spread to distant sites in the body (metastasis), enabling the establishment of secondary tumors.

Additional Emerging Hallmarks:

- **Deregulating Cellular Energetics:** Cancer cells often undergo metabolic changes, favoring pathways that support their energy demands and growth.
- **Avoiding Immune Destruction:** Cancer cells can evade detection and destruction by the immune system, allowing them to thrive despite the body's defenses.
- **Tumor-Promoting Inflammation:** Chronic inflammation in the TME can contribute to cancer development and progression.
- **Genome Instability and Mutation:** Cancer cells frequently exhibit genetic instability and mutations, contributing to their adaptability and heterogeneity.

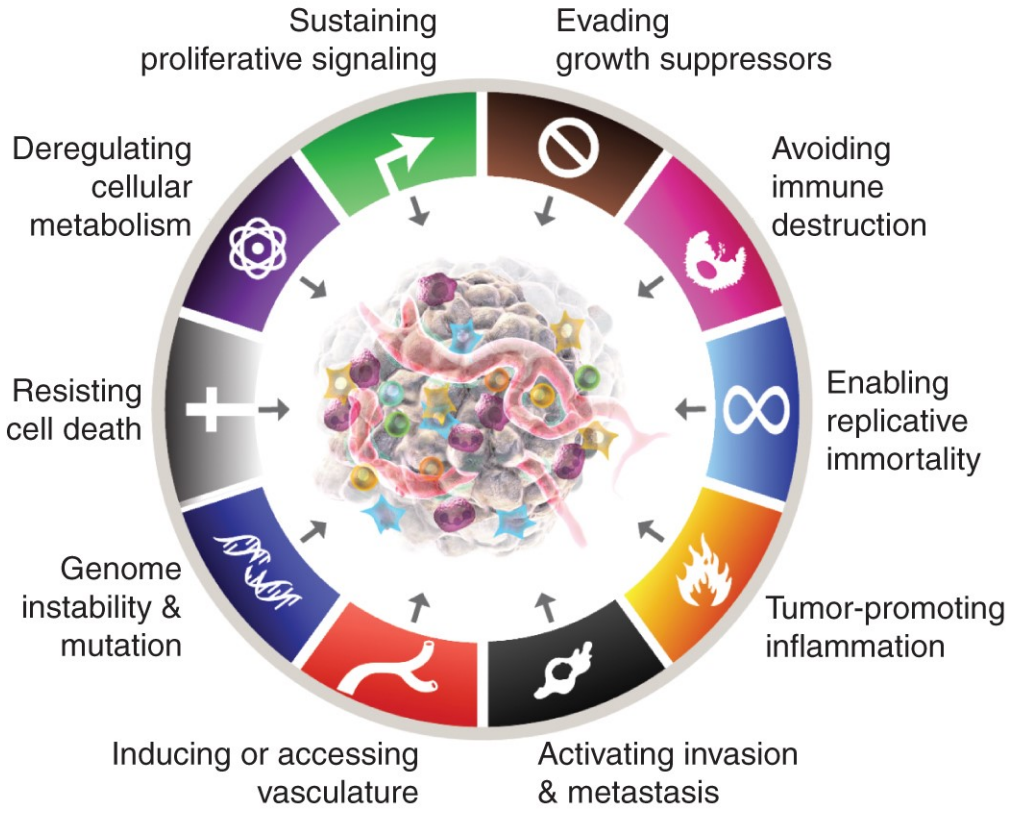

Figure 1.2: Hallmarks of cancer. Adapted from [7].

These hallmarks are interconnected processes that collectively contribute to the development and progression of malignancies. These interrelationships create a complex web

of interactions within cancer cells and their microenvironment. Understanding these interconnections is crucial for devising effective strategies to diagnose, treat, and manage cancer. Several examples highlight the intricate relationships between different hallmarks of cancer. One example, Tumor promotes angeogenesis. To illustrate, TME, composed of various cell types and extracellular components, plays a role in angiogenesis. Stromal cells can secrete factors that promote blood vessel formation, supporting tumor growth. The same factors that promote angiogenesis can also enhance invasion and metastasis forming another example of cancer hallmarks interrelationship. The last mentioned interrelation facilitates the spread of cancer cells to distant sites. Another important example, is the relationship between tumor vascularization (angiogenesis) and metabolism [7]. For cancer cells to multiply, they rely on the nourishment and oxygen supplied through tumor blood vessels. However, any reduction in the availability of blood vessels results in a shortage of nutrients and the onset of oxidative stress, ultimately giving rise to a condition of hypoxia [16]. Cancer cells have the capability to adjust their metabolic processes in response to stress conditions [17]. The interconnected nature of these hallmarks underscores the complexity of cancer biology and emphasizes the need for comprehensive and multidisciplinary approaches to understanding and treating cancer.

Role of intra-tumor (metabolic and vascular) heterogenity in cancer progression

Metabolic and vascular heterogeneity are two interconnected aspects of the TME that play critical roles in cancer progression, treatment response, and overall disease outcome. Both metabolic and vascular heterogeneity contribute to the complex and dynamic nature of tumors.

Metabolic Heterogeneity:

Metabolic heterogeneity refers to the variations in metabolic processes and pathways within different regions of a tumor. Tumor cells often adapt their metabolism to meet the demands of rapid proliferation and survival [7]. Key metabolic alterations include shifts in glucose metabolism (Warburg effect [18]), changes in amino acid utilization, and alterations in lipid metabolism. Metabolic heterogeneity can arise due to factors such as differences in nutrient and oxygen availability, mutations, and microenvironmental conditions. Metabolic heterogeneity highly contributes to resistance against cancer therapies. Cells with distinct metabolic profiles might respond differently to treatments, leading to the survival of therapy-resistant subpopulations. Additionaly, novel treatment strategies arises targeting specific metabolic vulnerabilities. For example, drugs that disrupt metabolic pathways essential for tumor growth and survival are being investigated as potential therapeutic options.

Vascular Heterogeneity:

Vascular heterogeneity refers to variations in blood vessel structure, function, and distribution within tumor . Tumors often develop abnormal blood vessel networks due to rapid growth and inadequate oxygen/nutrient supply [19]. These vessels can be leaky, tortuous, and poorly organized, leading to heterogeneous blood flow and oxygen levels across different tumor regions.

Vascular heterogeneity can directly affect the tumor development [20, 21]. It affects the availability of nutrients and oxygen to tumor cells. Regions with poor blood supply may experience hypoxia (low oxygen levels), which can influence tumor cell behavior, including resistance to therapies. Additionally, regular blood vessel networks can limit the effective delivery of cancer treatments, such as chemotherapy and immunotherapy, to all parts of the tumor. This can result in inadequate drug exposure and treatment resistance. Furthermore, Abnormal blood vessels contribute to the spread of cancer cells by providing pathways for metastatic cells to enter the bloodstream and reach distant sites.

Interplay between Metabolic and Vascular Heterogeneity:

Metabolic and vascular heterogeneity are interconnected. For instance, regions of hypoxia can influence metabolic adaptations, such as increased glycolysis, to generate energy in the absence of oxygen [22]. Additionally, metabolic factors, such as lactate production, can affect the TME and contribute to angiogenesis (formation of new blood vessels).

Understanding the interplay between metabolic and vascular heterogeneity is crucial for developing effective therapeutic strategies. Combining treatments that target both metabolic vulnerabilities and vascular abnormalities may enhance treatment responses and improve patient outcomes. Personalized approaches that consider the specific metabolic and vascular characteristics of individual tumors hold promise for more precise and impactful cancer therapies.

1.1.4 Importance of early detection and accurate staging in improving cancer treatment outcomes and survival rates

The early detection and accurate staging plays a pivotal role in cancer management. Immense impact could be well explained in cancer treatment.

Optimal Treatment Planning: Early detection allows for the identification of cancer at an earlier, more treatable stage. When cancer is detected early, it is often smaller in size and has not yet spread to nearby lymph nodes or distant organs. This makes it more amenable to localized treatments such as surgery, radiation therapy, or targeted therapies. Accurate staging helps determine the extent of the cancer's spread and guides the selection of the most appropriate treatment approach.

Less Aggressive Treatments: Early-stage cancers often require less aggressive treatments compared to cancers that are diagnosed at advanced stages. This can lead to reduced side effects, better quality of life during and after treatment, and quicker recovery.

Preservation of Organ Function: Early detection and treatment can help preserve the normal function of affected organs. For example, a smaller tumor may be easier to remove surgically without causing significant damage to surrounding tissues or organs.

Higher Success Rates: Cancers detected at an early stage generally have better treatment outcomes and higher survival rates. The chances of successful treatment, complete remission, and long-term survival are significantly improved when cancer is identified before it has a chance to grow extensively or metastasize (spread to other parts of the body).

Reduced Risk of Recurrence: Treating cancer at an early stage reduces the risk of recurrence. When cancer is caught and treated early, there is a higher likelihood of eliminating all cancer cells from the body, which reduces the chances of the cancer coming back.

Improved Prognosis: Accurate staging provides important prognostic information, helping healthcare providers predict the likely course of the disease and the patient's chances of survival. This information is valuable for making informed treatment decisions and setting realistic expectations.

Access to Targeted Therapies: Early detection and accurate staging allow for the timely use of targeted therapies. These therapies are designed to specifically target cancer cells based on their unique characteristics, minimizing damage to healthy cells and improving treatment effectiveness.

1.2 Paraganglioma (PGL)

1.2.1 Definition

PGL and Pheochromacytoma (PCC) are rare neuroendocrine tumors arising from the adrenal medulla, situated on top of the kidneys, and the extra-adrenal paraganglia, respectively [23]. PCCs are tumors of the sympathetic system that frequently secrete catecholamines like noradrenaline and/or adrenaline. PGLs are categorized based on their origin within the autonomic nervous system ganglia, being either parasympathetic or sympathetic.

Parasympathetic PGLs do not secrete catecholamines. PGLs of the sympathetic type often exhibiting elevated levels of noradrenaline release [23]. The majority of PCCs and PGLs can be effectively treated through surgical intervention [24]. However, around 15-20% of these tumors have the potential to metastasize. The World Health Organization (WHO) acknowledges that all PCCs and PGLs possess the potential for distant spreading and therefore recommends avoiding the term 'malignant' in such cases. Instead, the use of 'metastatic tumor' is preferred over 'malignant tumor' [23]. The presence of metastases is relatively rare, occurring in less than 10% of parasympathetic PGLs, up to 25% of PCCs, and ranging from 40-70% in sympathetic PGLs ([25], [26], [27]). Patients diagnosed with metastatic tumors often exhibit advanced disease, leading to a compromised lifespan. Metastatic pheochromocytomas and paragangliomas commonly metastasize to the lymph nodes, skeletal framework, pulmonary tissues, and the liver, exhibiting varying degrees of aggressiveness. The occurrence of metastases can be detected upon initial diagnosis or subsequently following the identification of the primary tumor ([28], [29] & [27]).

1.2.2 PGL Localization

PCCs and PGLs are distributed throughout the paraganglia, spanning from the neck to the pelvis as illustrated in Figure 1.3 [30, 31]. The primary location for parasympathetic paraganglia is the head and neck area, particularly highlighted in Figure 1.3-A. Tumor formation

is closely related to specific nerves, such as the glossopharyngeal nerve in the carotid bodies, as well as the jugular and tympanic paraganglia situated in the middle ear (known as glomus jugulare and glomus tympanicum). Sympathetic paraganglia, on the other hand, are situated within the chest, abdomen, or pelvis, depicted in Figure 1.3-B.

PGLs are commonly found within the prevertebral and paravertebral connective tissues, along the inferior hypogastric plexuses, and within the urinary bladder wall. Notably, the larger instances of PGLs include the bilateral adrenal medullas and the organ of Zuckerkandl. These growths may also manifest in various locations such as the gallbladder, liver, specific branches of the abdominal vagus nerve, and even in unexpected areas like the orbit, mandible, paranasal sinuses, thyroid gland, parathyroid gland, mediastinum, lungs, heart, gastrointestinal tract, pancreas, and mesentery.

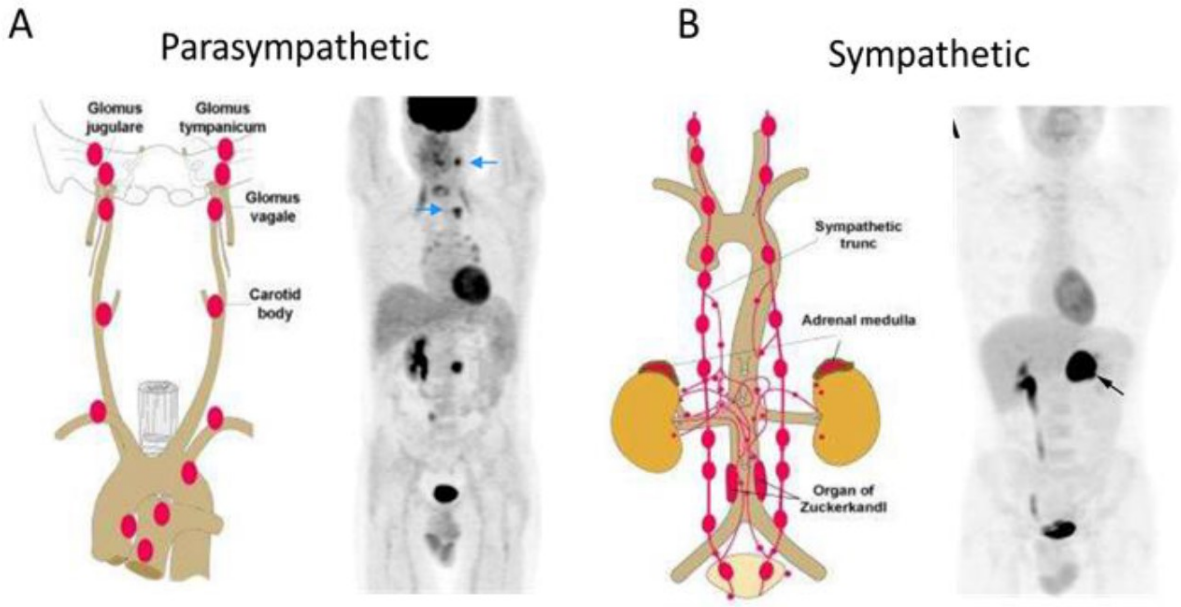

Figure 1.3: Localization of parasympathetic (A) and sympathetic (B) paragangliomas. Adapted from ([30], [31]).

1.2.3 Genetic PGL

Pheochromocytoma and Paraganglioma (PPGL) is recognized as a tumor that is heavily influenced by genetic factors. To date, research has unveiled the identification of over 20 susceptibility genes associated with this condition ([32], [33], [34], and [35]). Changes in certain autosomal genes responsible for encoding Succinate Dehydrogenase (SDH) enzymes have emerged as the predominant contributors to hereditary PHEO/PGL. These genes consist of succinate dehydrogenase complex subunit A (SDHA), subunit B (Succinate Dehydrogenase complex subunit B (SDHB)), subunit C (SDHC), subunit D (SDHD), and succinate dehydrogenase complex assembly factor 2 (SDHAF2). These genetic alterations are now acknowledged as potentially accounting for around half of the genetic mutations in

phaeochromocytomas and PGLs, as indicated in Figure 1 ([36], [37], [38] and [39]). The subsequent most prevalent germline mutations are associated with conditions such as von Hippel-Lindau syndrome (VHL), multiple endocrine neoplasia type 2 (RET), and neurofibromatosis type 1 (NF1).

Recent insights reveal that mutations in numerous other genes, though individually infrequent, can also give rise to hereditary tumor syndromes exhibiting PCC/PGL. Examples of these genes include MDH2 [40], GOT2 [41], SLC25A11 [42], DLST [33], MET [43], MERTK [43], H3F3A [43] , DNMT3A [32].

SDHB mutations

Mutations in the SDHB gene contribute to a heightened risk of metastatic progression in PPGL, thereby serving as a key predictor of malignancy in affected patients ([44], [45]). Approximately half of individuals with SDHB-mutated PPGL experience metastatic disease, and a germline SDHB mutation is identified in 36% of those with metastatic PGL ([44], [37], and [46]). Initial investigations suggested that metastatic PPGL cases with SDHB mutations had a more unfavorable prognosis compared to non-SDHB cases ([47], [48]). However, a large international study involving 169 patients with metastatic PPGL has challenged this concept. This recent study revealed that the SDHB status was no longer a prognostic indicator for worse outcomes [49]. This shift in perspective could be attributed to the significant increase in follow-up care and surveillance established for individuals carrying SDHB mutations over the past decade ([50], [49]).

1.2.4 Tumorigenesis of PGL

Tumorigenesis of PGLs with SDHB mutations is a complex process [51]. The SDH enzyme complex, also known as Complex II of the mitochondrial respiratory chain, plays a critical role in cellular respiration. It is responsible for converting succinate to fumarate in the citric acid cycle (Krebs cycle) and also participates in the electron transport chain. Mutations in the SDHB gene disrupt the normal function of the SDH complex. These mutations are typically inherited in an autosomal dominant manner, meaning that individuals with one mutated SDHB allele have an increased risk of developing PGLs. The loss of function of SDHB leads to various cellular changes that contribute to tumorigenesis. The inhibition of Hypoxia-Inducible Factor (HIF) prolyl hydroxylases by succinate leads to the stabilization and accumulation of proteins, particularly HIF-2α [52]. HIF is a transcription factor that regulates the expression of genes involved in angiogenesis, cell proliferation, and glucose metabolism in response to hypoxia (low oxygen levels). Elevated HIF levels in cells with SDHB mutations drive the expression of genes that promote angiogenesis and cell proliferation. These pathways are critical for tumor growth and survival. The dysregulation of HIF and other downstream signaling pathways, along with additional genetic and epigenetic alterations, can lead to the formation of PGLs. The stabilization of HIF-2α in SDHB-associated PGLs results in the upregulation of pro-angiogenic factors, such as Vascular Endothelial Growth Factor Receptor (VEGF). VEGF is a key regulator of angiogenesis and plays a central role in the formation of new blood vessels. The increased expression of VEGF in these tumors stimulates the growth of blood vessels within the tumor. These

tumors are typically highly vascularized, which is a hallmark of their biology. PGLs with SDHB mutations are associated with an increased risk of metastasis, particularly to lymph nodes and distant organs.

In summary, the vascularization of SDHB-associated PGLs is closely linked to the accumulation of succinate, the stabilization of HIF-2α, and the subsequent upregulation of pro-angiogenic factors like VEGF. This vascularization pattern contributes to the aggressive behavior of these tumors, including their propensity for metastasis. Understanding the molecular mechanisms underlying vascularization in SDHB-associated PGLs is important for the development of targeted therapies and improved management of these tumors.

The highly vascularized nature of SDHB-associated PGLs has led to investigations into anti-angiogenic therapiessuch as sunitinib as potential treatment options. Sunitinib is a tyrosine kinase inhibitor that targets multiple receptors involved in angiogenesis and tumor growth. It primarily inhibits receptors like VEGF and platelet-derived growth factor receptor (PDGFR). These receptors are crucial for the formation of new blood vessels, making sunitinib an anti-angiogenic therapy.

1.3 Non-Invasive Imaging

In the course of this thesis, we delve into the intricacies of PGL tumors, specifically focusing on their unique characteristics and the advancements in medical imaging techniques that play a crucial role in assessing the treatment response of PGL tumors to the antiangiogenic drug sunitinib. To embark on this comprehensive exploration, we first establish a foundational understanding of the physics behind the non-invasive medical imaging modalities that are particularly pertinent to the context of PGL tumors under the influence of sunitinib treatment. This section helps us grasp the fundamental principles of the current imaging technologies with a major focus on the ones employed in this thesis.

1.3.1 Computed Tamography

Computed Tomography (CT) is a medical imaging technique that uses X-rays to create detailed cross-sectional images of the body's internal structures. A CT scanner consists of an X-ray source and a detector array. The X-ray source emits a controlled and narrow beam of X-rays, which passes through the body. As the X-ray beam passes through the body, it is attenuated (absorbed or scattered) to varying degrees by different tissues and structures. The detector array on the opposite side of the patient records the intensity of the X-rays that have passed through. This creates a set of one-dimensional X-ray projections. The gantry containing the X-ray source and detector rapidly rotates around the patient. During this rotation, multiple sets of X-ray projections are acquired from different angles around the body. Modern CT scanners can acquire hundreds of these projections in a matter of seconds. The acquired X-ray projections are sent to a computer. In a process called reconstruction, sophisticated mathematical algorithms (usually filtered back-projection or iterative reconstruction) are used to combine the projections and reconstruct a two-dimensional image

(slice) of the body at each angle. The reconstructed images consist of small units called voxels (volumetric pixels), which represent tiny volume elements in the body. Each voxel corresponds to a specific position in three-dimensional space.The CT scanner continues to rotate and acquire slices at different depths within the body. These slices are stacked together to create a three-dimensional volume dataset. The resulting three-dimensional dataset can be visualized in various ways, including axial (cross-sectional), coronal (frontal), and sagittal (side) views. Radiologists and healthcare professionals use these images to diagnose medical conditions, plan surgeries, and monitor treatment progress.

1.3.2 Positron Emission Tomography (PET) imaging

PET is a cutting-edge molecular imaging technique that employs radiotracers to observe and measure the distinctive biological properties of tumors. The underlying principle of PET is rooted in the emission of positrons by radionuclides during their decay process. These emitted positrons then combine with electrons, leading to the generation of two gamma rays with an energy of 511 keV, positioned at a 180° angle from each other [53]. To capture these emitted gamma rays, a circular array of detectors is utilized. Radionuclides suitable for PET imaging are found in both clinical and research contexts, encompassing fluorine-18 [18F], carbon-11 [11C], zirconium-89 [89Zr], gallium-68 [68Ga], and copper-64 [64Cu]. Notably, for clinical purposes, 18F is the most prevalent choice due to its advantageous half-life (T1/2 = 1.8 h), efficient production of positrons, and heightened detection sensitivity, thus making it highly favored [54].

Thanks to advancements in nuclear medicine, a diverse range of radiopharmaceuticals are now accessible for clinical use to assess the distinct biological characteristics of tumors. For instance, 18F-Fluorodeoxyglucose (FDG) is employed to gauge tumor metabolism [53], 18F-FMISO examines hypoxia [55], 18F-FLT probes tumor cell proliferation [56], 18F-labeled amino acids delve into protein synthesis [57], and 15O–water studies blood flow within tumors [58]. Moreover, the scope of PET imaging has expanded through its integration with tumor-specific monoclonal antibodies, known as immune-PET. This amalgamation has spurred the exploration of numerous monoclonal antibodies and radionuclides, paving the way for the development of immune-PET tracers [59]. Additionally, novel avenues involve utilizing peptides and other compounds that target receptors, such as nanobodies or bispecific antibodies, to craft innovative immune-PET tracers [59]. This approach holds great potential by dynamically tracking the expression of tumor antigens, thereby offering a promising method to evaluate the effectiveness of targeted cancer therapies.

The inherent strengths of PET imaging encompass its exceptional sensitivity and measurable imaging factors, like the Standardized Uptake Value (SUV). Through the fusion of anatomical and functional imaging data in PET-CT, the evaluation of tumors' molecular characteristics becomes achievable, accompanied by meticulous corrections for anatomical structures.

1.3.3 Magnetic Resonance Imaging (MRI)

Magnetic Resonance Imaging (MRI) is a medical imaging technique based on the principles of nuclear magnetic resonance. Operating within a strong magnetic field, MRI captures detailed cross-sectional images of the body's internal structures. The process involves the alignment of hydrogen nuclei, predominant in the human body, through exposure to the magnetic field. Subsequent application of radiofrequency pulses causes these nuclei to absorb and release energy, generating signals that are captured by radiofrequency coils. The incorporation of gradient coils introduces spatial variations, facilitating the localization of signals in three-dimensional space. Computer algorithms then reconstruct these signals into highly detailed images, providing exceptional soft tissue contrast. MRI finds extensive applications, encompassing neuroimaging for brain and spinal assessments [60, 61], musculoskeletal imaging for orthopedic evaluations [62, 63], and cardiac imaging for heart assessments [64, 65]. Its non-ionizing radiation, versatility, and ability to offer unparalleled soft tissue visualization contribute to its pivotal role in diagnostic medicine. Despite its advantages, MRI is associated with challenges, including prolonged scan durations, the lack of portability in equipment, high associated costs, vulnerability to movement artifacts, and constraints in achieving real-time scanning capabilities. Therefore, Ultrafast Ultrasound Doppler is preferred over MRI in scenarios requiring real-time assessment of dynamic processes like blood flow, primarily due to its cost-effectiveness and accessibility.

1.3.4 Ultrafast Ultrasound Doppler

Ultrafast Doppler [66] uses high-frequency sound waves, or ultrasound, to create images and assess blood flow. These ultrasound waves are emitted by a transducer, which is placed on the patient's skin. multiple transducer elements are organized in a two-dimensional array. This array allows for the simultaneous emission and reception of ultrasound waves from multiple locations on the patient's body [67]. The ultrasound beams are emitted and directed toward the region of interest, such as a blood vessel. When the ultrasound waves encounter moving red blood cells within the vessel, they undergo a change in frequency due to the Doppler effect. The key innovation in Ultrafast Doppler is its ultrafast data acquisition capability. It can acquire a large number of data points or samples in very short time intervals (on the order of microseconds). The received ultrasound signals, which contain information about the velocity and direction of blood flow at various locations within the imaging plane, are processed in parallel. Each element of the transducer array processes its own data. The processed data is then used to create real-time color Doppler images. In these images, blood flow is color-coded to indicate its velocity and direction. For example, blood flow toward the transducer may be displayed in red, while flow away from the transducer may be displayed in blue. Ultrafast Doppler can be integrated with B-mode ultrasound imaging, which provides anatomical context. This fusion of functional and structural information enhances the diagnostic value of the imaging.

This technique offers numerous benefits, including wide availability, absence of radioactivity, and cost-effectiveness. These advantages make it highly suitable for repeated utilization in clinical settings. Through the Doppler technique, ultrasound becomes capable

of evaluating blood flow within tumors. Notably, by introducing contrast agents like microbubbles, dynamic contrast-enhanced ultrasound can track changes over time in both hemodynamic factors (like perfusion and flow velocity) and morphological factors (such as blood volume and vascular variations) within a specific tumor, relative to its condition before treatment. The potential significance of these parameter changes in monitoring the response to anti-angiogenic therapies has been the subject of investigation [68, 69].

1.3.5 Multi-modal Imaging

Definition

Multi-modal medical imaging refers to the integration of information from two or more different imaging techniques in the field of medicine to provide a more comprehensive and accurate assessment of a patient's condition. By combining data from various imaging modalities, medical professionals can obtain a more detailed understanding of anatomical structures, physiological processes, and disease progression. For example, PET is often combined with CCT to provide both metabolic and anatomical information. PET detects radioactive tracers that highlight areas of high metabolic activity (such as cancer cells), while CT provides detailed structural images.

Significance of Multimodal Imaging in Cancer

Multimodal imaging plays a crucial role in the field of oncology by providing a more comprehensive and accurate assessment of cancer [70, 69]. Cancer is a complex disease with varying anatomical, functional, and molecular characteristics, and utilizing multiple imaging modalities can greatly enhance our understanding of the disease. Here's how multimodal imaging improves cancer diagnosis, staging, treatment planning, and monitoring:

- Accurate Diagnosis: Different imaging modalities capture different aspects of cancerous tissues. Combining modalities like CT, Magnetic Resonance Imaging (MRI), and PET allows clinicians to see both anatomical details and metabolic activity. This aids in distinguishing between benign and malignant tumors and provides a more accurate diagnosis.

- Staging and Localization: Multimodal imaging helps stage the extent of cancer spread. For instance, combining PET with CT or MRI can provide information about the primary tumor as well as the presence of metastases in other parts of the body, aiding in accurate cancer staging.

- Characterization of Tumor Heterogeneity: Tumors can have varying cell types, structures, and activity levels within them. Multimodal imaging allows for the identification and characterization of these heterogeneous regions, which is crucial for personalized treatment planning.

- Treatment Planning: By integrating information from various modalities, clinicians can better plan cancer treatments. For instance, combining MRI and PET data can guide the precise targeting of radiation therapy or aid in surgical planning by identifying critical structures to avoid.
- Monitoring Treatment Response: Multimodal imaging enables real-time monitoring of treatment response. By comparing images before and after treatment, clinicians can assess changes in tumor size, metabolism, and blood flow, helping to determine the effectiveness of the chosen treatment regimen.
- Predicting Treatment Outcome: The combination of anatomical, functional, and molecular information allows clinicians to predict how a tumor might respond to specific treatments. This aids in selecting the most appropriate therapeutic approach for individual patients.
- Early Detection and Recurrence Monitoring: Integrating different modalities can enhance the sensitivity of cancer detection, especially for small lesions or early-stage cancers. Additionally, multimodal imaging aids in monitoring for cancer recurrence after initial treatment.
- Research and Drug Development: Multimodal imaging is invaluable in preclinical research for studying cancer in animal models and evaluating potential new treatments. It allows researchers to track disease progression and treatment effects in a comprehensive manner

1.4 Artificial Intelligence (AI) for Cancer Imaging and Multimodal imaging

1.4.1 Define AI

AI refers to the simulation of human intelligence processes by computer systems [71]. It encompasses the development of algorithms, software, and machines that can perform tasks that typically require human intelligence, such as understanding natural language, recognizing patterns, solving complex problems, and making decisions. AI aims to replicate human cognitive functions in a way that enables machines to learn from experience, adapt to new situations, and perform tasks autonomously. AI technologies are built on various principles and techniques, including:

Machine Learning (ML): is a subset of artificial intelligence that focuses on the development of algorithms and models that enable computers to learn from data and make predictions or decisions without being explicitly programmed for every specific task [72]. ML systems aim to improve their performance over time through experience, much like how humans learn from their experiences.

ML can be categorized into several types, each with its own characteristics and applications Figure1.4:

1. Supervised Learning: In supervised learning, the algorithm is trained on a labeled dataset, where the input data is paired with corresponding correct output labels. The algorithm learns to map input data to the correct output by identifying patterns and relationships. It can then make predictions on new, unseen data. Examples include image classification, spam email detection, and medical diagnosis. Supervised learning algorithms could be Linear and Logestic Regression, Decision Trees, Random Forest (RF), Support Vector Machine (SVM), Naive Bayes, Gradient Boosting Algorithms, etc... Within the scope of this thesis, we will only provide an overview of the applied supervised algorithms:

    - RF: is an ensemble learning method based on decision trees. It constructs multiple decision trees and combines their predictions to provide a final output. This ensemble approach helps to improve the overall accuracy and robustness of the model. RF creates a "forest" of decision trees by training each tree on a random subset of the dataset, allowing for diverse models [73]. The randomness is introduced in two main ways: bootstrapping, which involves sampling with replacement to create multiple subsets of the data, and random feature selection, which involves selecting a subset of features for each tree.
        (a) Tree Construction: Each decision tree in the RF is grown independently. At each node of the tree, a subset of features is randomly selected, and the best split is determined based on criteria such as Gini impurity or information gain. This process continues until a stopping criterion is reached, usually defined by a maximum tree depth or a minimum number of samples in the nodes. The trees aim to create partitions that best segregate the data in each subset.
        (b) Prediction Aggregation: For classification tasks, the final prediction in a RF is determined through a voting process, where the most popular prediction among the individual trees is selected. In regression tasks, the average prediction from each tree is considered as the final output. This ensemble approach reduces overfitting and variance by combining predictions from multiple diverse trees, leading to a more accurate and robust model.
        (c) Feature Importance: RF assesses the importance of features by calculating the information gain or decrease in impurity at each split in the trees [74]. It measures how much each feature contributes to improving the model's predictions. This feature importance information can help identify the most relevant features for making accurate predictions and provide insights into the dataset.
        (d) Advantages: RF offers various advantages, including its ability to handle high-dimensional data, resistance to overfitting, robustness against noise and outliers, and ease of interpretability due to its intuitive nature [75]. Additionally, the ensemble approach makes it a powerful and widely used algorithm across various fields, including finance, healthcare, and e-commerce, for tasks such as classification, regression, and feature selection.

    RF's ability to aggregate predictions from diverse decision trees, its robustness against overfitting, and its feature importance evaluation make it a valuable tool in predictive modeling across a range of applications.

- SVM: is a robust and versatile machine learning algorithm designed for both classification and regression tasks. At its core, SVM seeks to find the optimal hyperplane that effectively separates data points of different classes in feature space. The key distinguishing factor of SVM is its emphasis on maximizing the margin, which is the distance between the hyperplane and the nearest data points of each class.

  The workflow of SVM involves defining a hyperplane that acts as a decision boundary. This hyperplane is positioned to maximize the margin, providing the algorithm with better generalization capabilities when dealing with new, unseen data. The data points that lie closest to the hyperplane, known as support vectors, play a crucial role in determining the optimal hyperplane.

  SVM is not limited to linear decision boundaries. It employs the kernel trick, a technique that transforms the input space into a higher-dimensional space, allowing SVM to find nonlinear decision boundaries. This flexibility is particularly valuable when dealing with complex, nonlinear relationships within the data.

  In practical applications, SVM has proven effective across various domains. In image classification, SVM excels in tasks such as facial recognition [76]. In cancer detection [77] and classification [78]. In radiology, SVM can analyze images from modalities like X-rays, CT scans, and MRIs to distinguish between healthy and cancerous tissues [79]. Its capacity to handle high-dimensional data is crucial when dealing with the intricate structural details inherent in medical images.

  Despite its strengths, SVM does come with considerations. It can be computationally intensive, especially with large datasets. Careful parameter tuning, particularly regarding the choice of kernel parameters, is crucial for optimal performance. Furthermore, SVM lacks a natural probabilistic interpretation in its classification decisions.

  In summary, SVM is a powerful algorithm recognized for its ability to handle both linear and nonlinear relationships in data. Its emphasis on maximizing the margin, support for complex decision boundaries, and versatility in various applications make SVM a valuable tool in the machine learning landscape.

- Gaussian naive Bayes (GNB): is a probabilistic classification algorithm based on Bayes' theorem, named after the Reverend Thomas Bayes [80]. It assumes that the features used to describe an observation are conditionally independent, given the class label. Bayes' Theorem calculates the probability of a hypothesis (class - A) given the observed evidence (features - B):

$$P(A/B) = \frac{P(B/A) \times P(A)}{P(B)} \tag{1.1}$$

  GNB works as follows: First, we calculate the prior probability by determining the probability of each class occurring without considering the features. Second, we calculate the Likelihood for each feature given the class by calculating the probability of observing that feature. Third, we multiply both the prior probability of the class and the likelihood of each feature given that class. Finally, we assign the class with the highest product as the predicted class.

GNB simplicity and speed make it particularly suitable for various applications, including text classification (spam filtering, sentiment analysis) [81], medical diagnosis [82], and recommendation systems [83]. Notably, it excels with high-dimensional data and requires a relatively small amount of training data to produce effective results. However, it has limitations, such as the assumption of feature independence, which may not hold in all cases, and sensitivity to irrelevant features. Despite these constraints, Naive Bayes stands as a versatile and efficient algorithm, especially valued in natural language processing tasks.

2. Unsupervised Learning: Unsupervised learning involves working with unlabeled data. The algorithm's goal is to find inherent patterns or structures within the data, such as clustering similar data points together. Common techniques include clustering and dimensionality reduction, which are used in customer segmentation, anomaly detection, and data visualization. Examples of unsupervised algorithms could be K-means, Hierarchical clustering, Principal Component Analysis, Self-Organizing Maps (SOMs), Generative Adversarial Networks (GANs), etc ...

   In the context of this thesis we will provide a coincise explanation of the unsupervised techniques used:

   - Hierarchical Clustering (HCA) is a technique used in unsupervised ML and statistical analysis to group data points into clusters based on their similarities [84]. This method is particularly useful when you want to discern natural groupings within a dataset without any prior information about the groups. The process organizes the data into a tree-like hierarchical structure known as a dendrogram. There are two primary types of HCA: agglomerative and divisive. In our thesis we focus on the agglomerative type.

     Agglomerative Clustering: This method starts with each data point as an individual cluster and then merges the closest clusters iteratively until all data points belong to one single cluster [84]. The steps involved in agglomerative clustering are:

     (a) Distance Calculation: Initially, the algorithm computes the pairwise distances between all data points. These distances can be measured using various methods, such as Euclidean distance, Manhattan distance, or correlation distance, depending on the nature of the data.
     (b) Initialization: Each data point is treated as an individual cluster.
     (c) Merge Closest Clusters: The algorithm identifies the closest clusters based on the chosen distance metric and merges them into a single cluster. This process continues until all data points are within a single cluster.
     (d) Dendrogram Construction: Throughout the merging process, the algorithm constructs a dendrogram, which represents the merging process and can help in visualizing the cluster hierarchy.

     The choice of the distance metric and linkage method significantly impacts the final clustering results. Common linkage methods include single linkage (based on the minimum distance between clusters), complete linkage (based on the maximum distance between clusters), and average linkage (based on the average distance between clusters).

HCA's key advantage is its ability to show the relationship between clusters at different levels of granularity. The dendrogram provides a visual representation that can help determine the optimal number of clusters, aiding in the interpretation and analysis of the data's inherent structure [85].

Once the clusters are formed, further analysis can be performed to understand the characteristics of each cluster, enabling insights into natural groupings and patterns within the data, which can be invaluable in various fields like biology, marketing, and social sciences.

- K-means [86] is a popular unsupervised ML algorithm used for clustering data into groups based on similarity. It is an iterative algorithm that partitions a dataset into K distinct clusters, where K is a predetermined number. Here's a detailed explanation of the K-means algorithm:
  (a) Initialization: The algorithm starts by randomly selecting K data points from the dataset as the initial centroids of the clusters. These centroids represent the centers of the clusters.
  (b) Assignment of Data Points to Clusters: Each data point in the dataset is then assigned to the nearest centroid based on a chosen distance metric, commonly using Euclidean distance. The distance is calculated between each data point and the centroids, and the data point is assigned to the cluster with the nearest centroid.
  (c) Update Centroids: After assigning all data points to clusters, the algorithm recalculates the centroids for each cluster. The new centroids are calculated as the mean of all data points assigned to that cluster. This step aims to reposition the centroids at the center of the data points within each cluster.
  (d) Iterative Process: Steps 2 and 3 are repeated iteratively, with data points reassigned to the nearest centroids and centroids recalculated based on the new assignments. This process continues until the centroids no longer change significantly or until a predetermined number of iterations is reached.
  (e) Convergence: The algorithm converges when the centroids stabilize, meaning that the assignment of data points to clusters and the positions of centroids no longer change significantly between iterations.

  K-means clustering aims to minimize the sum of squared distances between data points and their respective cluster centroids. However, the initial selection of centroids can impact the final clustering result. Consequently, the algorithm might produce different clusterings with different initializations. To mitigate this, multiple runs with different initializations can be performed, and the best result in terms of clustering can be selected based on a defined criterion, such as minimizing intra-cluster distance and maximizing inter-cluster distance. K-means is widely used for various applications in data analysis, including image segmentation [87, 88], customer segmentation [89], and document clustering [90]. It is computationally efficient and relatively easy to implement, making it one of the most commonly used clustering algorithms in practice

3. Semi-Supervised Learning: This is a combination of supervised and unsupervised learning [91]. It utilizes a small amount of labeled data along with a larger amount of

unlabeled data for training. Semi-supervised learning is useful when obtaining large amounts of labeled data is difficult or expensive.

4. Reinforcement Learning: Reinforcement learning involves training agents to make a sequence of decisions in an environment to maximize a cumulative reward [92]. The agent learns by receiving feedback based on its actions. This type of learning is applied in areas like robotics, game playing (e.g., chess or Go), and autonomous systems.

5. Deep Learning: Deep learning is a subset of ML that uses neural networks with many interconnected layers to learn intricate patterns from data [93]. Deep learning has achieved remarkable success in tasks such as image and speech recognition, natural language processing, and autonomous driving.

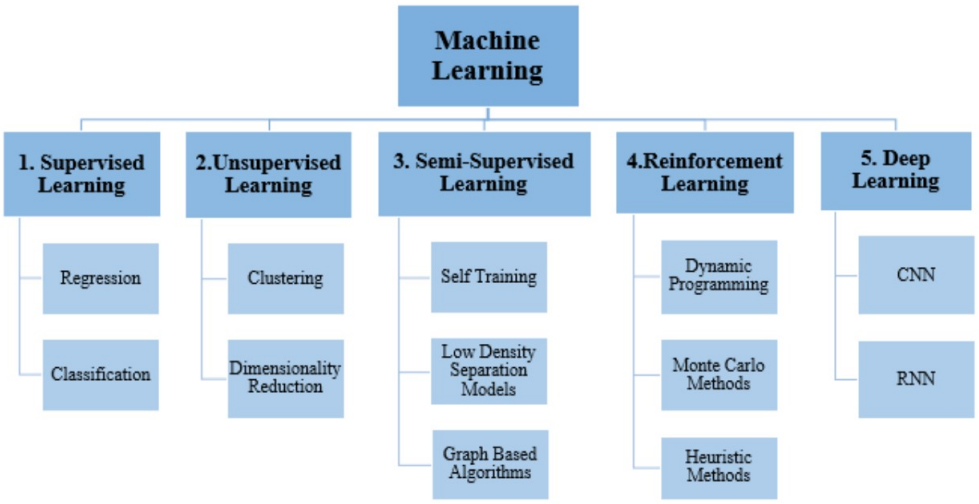

Figure 1.4: Various categories of machine learning and a range of algorithms. Adopted from [94]

ML processes typically involve these steps [72]:

1. Data Collection: Collect relevant data that the algorithm will learn from. High-quality data is essential for building accurate models.

2. Data Preprocessing: Clean, preprocess, and transform the data into a suitable format for training. This can involve tasks like handling missing values, normalization, and feature engineering.

3. Feature Selection/Extraction: Choose relevant features (input variables) that will contribute to the model's performance. In some cases, feature extraction techniques automatically derive informative features from the data.

4. Model Selection: Choose an appropriate ML algorithm or model architecture based on the problem at hand and the characteristics of the data.

5. Training: Feed the algorithm with the training data and the corresponding labels (if applicable). The algorithm learns to adjust its internal parameters to minimize the difference between predicted outputs and actual labels.

6. Validation and Hyperparameter Tuning: Evaluate the model's performance on validation data and fine-tune hyperparameters (parameters that are not learned during training) to optimize performance.

7. Testing and Deployment: Test the trained model on new, unseen data to assess its generalization capability. Once satisfied with the performance, deploy the model to make predictions on real-world data.

ML has had a transformative impact across various industries, including healthcare, finance, marketing, and more. However, successful implementation requires careful consideration of data quality, model selection, validation, and ethical considerations, as well as ongoing monitoring and maintenance of the deployed models.

1.4.2 Growing importance of AI in various healthcare domains

In the context of medical imaging, AI and ML technologies have become increasingly important and impactful. AI algorithms can automate time-consuming and repetitive tasks in medical imaging, such as image analysis and segmentation. This not only saves time for radiologists and clinicians but also reduces the risk of human error.

- Automation and Efficiency: AI algorithms can automate time-consuming and repetitive tasks in medical imaging, such as image analysis and segmentation. This not only saves time for radiologists and clinicians but also reduces the risk of human error.

- Enhanced Diagnosis: AI can aid in early and accurate disease detection by analyzing large amounts of imaging data. ML algorithms can learn patterns associated with specific diseases, helping identify subtle abnormalities that might be missed by human observers.

- Quantitative Analysis: AI can provide quantitative measurements of various anatomical and pathological features, enabling more precise and standardized assessments. This is especially useful in tracking disease progression and treatment response.

- Personalized Treatment: AI can assist in tailoring treatment plans based on individual patient characteristics. By analyzing patient data and medical images, AI can help predict treatment outcomes and guide personalized therapeutic strategies.

- Image Enhancement and Reconstruction: AI algorithms can improve the quality of medical images by reducing noise, enhancing contrast, and even reconstructing high-quality images from low-quality or limited data.

- Radiomics and Feature Extraction: AI can extract and analyze a multitude of features from medical images that might not be readily visible to the human eye. These

features, known as radiomic features, can provide valuable insights into disease characteristics and prognosis.

- Real-time Decision Support: AI systems can provide real-time decision support to clinicians by quickly analyzing images and providing diagnostic suggestions or highlighting areas of concern.
- Integration of Multi-modal Data: AI can integrate data from various imaging modalities and other patient information sources, offering a comprehensive view of the patient's condition and aiding in more informed decision-making.
- Research and Drug Development: AI can assist in drug development by analyzing the effects of potential treatments on cell cultures or animal models, thereby accelerating the process of identifying promising drug candidates.
- Reducing Variability: AI can help reduce inter- and intra-observer variability by providing consistent and standardized measurements and interpretations of medical images.

1.4.3 Role of AI in revolutionizing cancer imaging and patient care

AI is at the forefront of revolutionizing cancer imaging, significantly enhancing accuracy, efficiency, and effectiveness in various aspects of cancer diagnosis, staging, treatment planning, and monitoring. In this context, AI is reshaping cancer imaging in several key ways:

AI algorithms analyze medical images like mammograms, CT scans [95], and MRIs to detect subtle early signs of cancer [96], improving the prospects of successful treatment. Computer-aided detection systems powered by AI assist radiologists in highlighting potential abnormalities, ensuring no suspicious regions are overlooked. Additionally, AI can automatically segment tumors [97], healthy tissues, and organs in medical images, providing precise and consistent measurements for diagnosis and treatment planning. AI-driven image enhancement techniques also elevate image quality, facilitating the identification of subtle features and anomalies.

Radiomics, another AI-driven approach, analyzes an extensive array of quantitative features extracted from medical images to reveal patterns correlated with disease characteristics, prognosis, and treatment response ([98], [99]). This empowers the prediction of disease outcomes and the creation of individualized treatment plans. AI combines imaging data with genetic and clinical information to optimize tumor targeting while minimizing harm to healthy tissues, and it assists in radiation therapy planning by determining the ideal dose distribution for maximum treatment efficacy.

AI further assesses treatment response by analyzing sequential imaging data, enabling clinicians to make timely adjustments to treatment plans. It rapidly detects changes in tumor size, shape, and metabolic activity, providing early insights into treatment efficacy. AI expedites drug discovery by analyzing vast datasets to identify potential drug candidates and predict their effectiveness in targeting specific cancer pathways. It also optimizes patient selection for clinical trials by identifying those most likely to respond to new therapies.

AI techniques enable 3D visualization and reconstruction of complex tumor structures, aiding surgeons in planning minimally invasive procedures and optimizing surgical outcomes. Additionally, AI-driven automation reduces human error and variability in image interpretation, leading to more consistent and reliable diagnoses. It accelerates the analysis of large volumes of medical images, allowing radiologists to focus on more complex cases and provide faster turnaround times for patients.

AI supports researchers in analyzing large-scale imaging datasets to discover new insights into cancer biology, progression, and treatment response. Successful AI integration into cancer imaging necessitates rigorous validation, continuous AI model training, and close collaboration between radiologists, oncologists, and AI experts. Responsible implementation ensures that AI technologies effectively contribute to improved patient outcomes, reduced healthcare costs, and the advancement of our understanding of cancer.

1.5 Radiomics

1.5.1 Definition

Radiomics is a multidisciplinary field that sits at the intersection of medical imaging, computer science, and statistics. Its primary objective is to rapidly extract comprehensive and large number of quantitative features from medical images and subsequently analyze these features to derive clinically relevant information ([98], [99]). These images are obtained through various modalities like CT, MRI, PET, and others. Radiomics aims to uncover hidden information within these images that might not be apparent through visual inspection alone. This information can provide insights into disease characteristics, progression, and treatment response. While radiomics has the potential to be utilized across numerous medical conditions, its most advanced state is within oncology, primarily due to the backing it receives from initiatives such as the National Cancer Institute (NCI) Quantitative Imaging Network and other endeavors under the NCI Cancer Imaging Program [99].

In the cancer imaging context Quantitative features extracted from images, encompassing attributes such as intensity, shape, size or volume, and texture, provide insights into the unique tumor characteristics and the microenvironment it resides in([99], [100]). These insights are different from the information obtained from clinical reports, laboratory tests, and genomic or proteomic analyses. By combining these features with other data sources, they can be linked to clinical outcomes and utilized to enhance evidence-based clinical decision-making support.

Radiomics seems to provide an abundant array of imaging biomarkers, which have the potential to assist in various aspects of cancer-related tasks such as detection, diagnosis, prognosis evaluation, treatment response prediction, and disease status monitoring.

1.5.2 The radiomics process

The implementation of radiomics is often breaked down into several steps Figure1.5 [101, 102]:

1. **Quantittative Imaging:** Radiomics begins with the acquisition of high quality and standardized medical images, which could be from various imaging modalities such as CT, MRI, PET, and more. These images provide detailed information about the internal structures of the human body. Radiomics research needs extensive data for meaningful outcomes, like other data-driven approaches. That's why many studies use past data where images were taken with varying settings. These differences can affect how dependable the extracted radiomics features are ([103]).
2. **Region of Interest (ROI) Selection:** The following step involves outlining tumor boundaries (tumor segmentation), which can be done through automated algorithms or by a skilled radiologist.
3. **Feature Extraction:** Once the ROIs are defined, a large number of quantitative features are extracted from these regions. These features can be broadly categorized into several groups:
    - Intensity-based Features: These features are derived from the pixel or voxel intensities within the ROI. They include statistics such as mean, median, standard deviation, etc.
    - Shape Features: These features describe the geometric characteristics of the ROI, such as volume, surface area, compactness, and sphericity.
    - Texture Features: Texture features capture the spatial arrangement of pixel intensities within the ROI. They can describe patterns like smoothness, coarseness, or contrast variations.
    - Spatial Features: These features analyze the spatial relationships between different regions within the ROI, providing insights into how different structures interact.
    - Statistical Features: These features quantify statistical distributions and relationships within the ROI.
4. **Feature Selection and Dimensionality Reduction:** Since radiomic feature sets can be quite large, not all features might be relevant for a specific clinical task. Feature selection and dimensionality reduction techniques are applied to identify the most informative and reproducable features and reduce the risk of overfitting.
5. **Statistical Analysis and Modeling:** The extracted and selected features are then analyzed using various statistical and ML methods. These analyses aim to uncover correlations, patterns, and relationships between the features and clinical outcomes, such as disease diagnosis, prognosis, and treatment response.
6. **Model Development:** Radiomics can be used to develop predictive models that use the quantitative features to predict specific clinical outcomes. These models can range from simple regression models to more complex ML algorithms.

7. **Clinical Applications:** The insights gained from radiomics analyses can aid clinicians in making more informed decisions. For example, radiomics-based models might help differentiate between benign and malignant tumors, predict patient survival rates, assess treatment response, and guide personalized treatment plans.

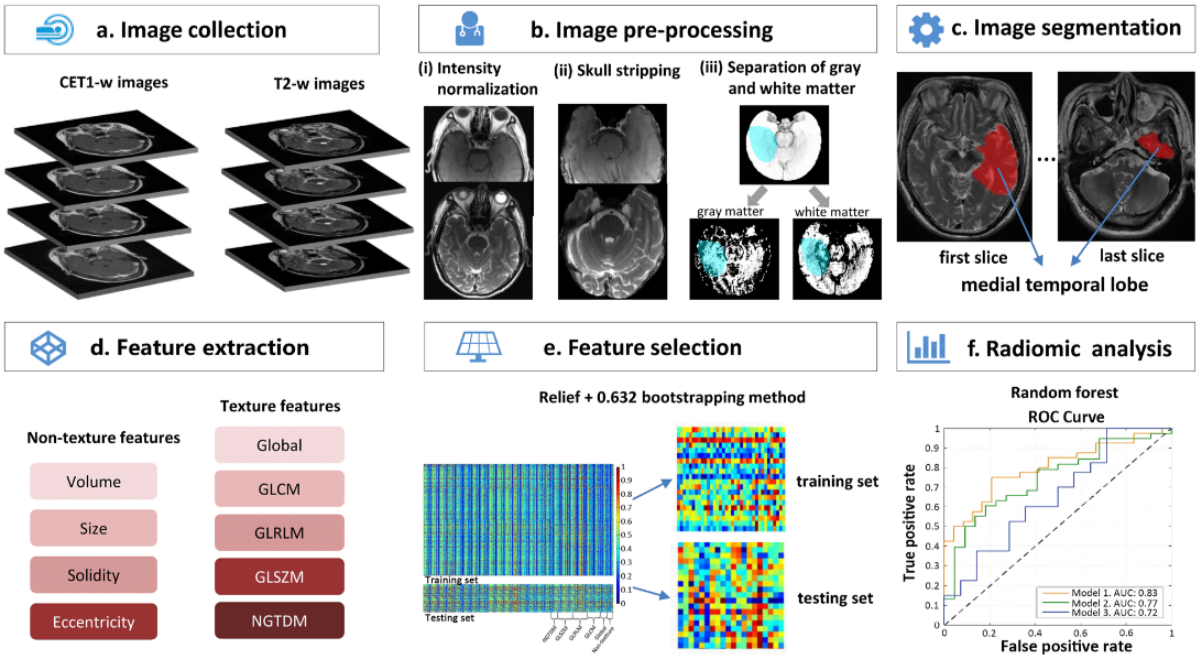

Figure 1.5: Radiomics Process [102]

1.5.3 Role of radiomics in providing valuable information about tumor characteristics and patient outcomes

Radiomics plays a crucial role in providing valuable insights into tumor characteristics and predicting patient outcomes [101, 104]. On the level of tumor characterization radiomics allows for a comprehensive analysis of the quantitative features extracted from medical images, such as CT scans or MRIs. These features capture various aspects of the tumor's appearance, shape, and texture that might not be discernible to the naked eye. By quantifying these subtle characteristics, radiomics can aid in differentiating between tumor types, grading tumors, and identifying specific molecular or genetic traits associated with the tumor. Moreover, radiomics detects heterogenity assesement. Tumors often exhibit internal heterogeneity, meaning different parts of the tumor have distinct characteristics. Radiomics can quantify this heterogeneity by analyzing the spatial distribution of pixel intensities within the tumor. This information is valuable for treatment planning, as heterogeneous tumors may respond differently to therapies and have varying prognoses. Additionaly, radiomics improves treatment response prediction. Radiomics features can provide early insights into how a tumor is responding to treatment. Changes in these features over time can indicate whether the tumor is shrinking, growing, or remaining stable.

This helps clinicians make timely adjustments to treatment plans, optimizing patient care. Radiomics improves personalized treatment planning as well. By combining radiomics data with other patient-specific information (clinical history, genetics, etc.), clinicians can tailor treatment strategies to each patient's unique profile [105]. This leads to more precise and effective therapies, minimizing potential side effects. Finally, radiomics features can serve as non-invasive biomarkers that provide valuable information about the tumor's biology and behavior. This reduces the need for invasive procedures to obtain similar insights.

1.6 Research Problem and Specific Research Questions

The research problem at the core of this thesis is the imperative to enhance our understanding of the dynamic and multifaceted nature of sunitinib resistance in PGL tumors. While sunitinib, an anti-angiogenic drug, offers promise as a treatment option, its effectiveness varies among patients, and resistance often emerges. This specific issue highlights the need to move beyond traditional growth characteristics of tumors. The central problem is the insufficient comprehension of the intricate interplay between vasculature and other metabolic parameters within PGL tumors, particularly in the context of anti-angiogenic therapy. This knowledge gap hampers the development of personalized and effective treatment strategies for PGL patients, necessitating a deeper exploration of the vascular and metabolic dimensions of these tumors.

Research questions:

1. What vascular and metabolic parameters within PGL tumors are associated with the development of resistance to sunitinib, and how can these parameters be reliably quantified through multi-modal imaging techniques?
2. How do the identified tumor sub-region(s) driving resistance to sunitinib, particularly those with distinct vasculature and metabolic characteristics, impact the overall prognosis and treatment response of PGL patients receiving sunitinib therapy?
3. Can ML algorithms be effectively trained to automate the classification of treatment response and tge identification of high-risk subregions within PGL tumors based on vasculature and metabolic data, and how does this automation impact the precision and efficiency of analysis?
4. How can radiomics-based features extracted from multi-modal medical imaging data (e.g., PET, Ultrafast Ultrasensitive Doppler (UUDI)) be utilized to quantify and characterize the tumor's heterogeneity, vasculature, metabolic attributes, and other characteristics, and which of these radiomic features are most indicative of sunitinib treatment response in PGL patients?

Now that we have established the fundamental concepts encompassing TME specifically metabolic and vascular characteristics, specifically focusing on PGL, as well as the pivotal role of multimodal imaging, AI, ML and radiomics in cancer treatment, it is crucial

to shift our attention towards the primary objectives of this thesis. The integration of these interdisciplinary fields forms the bedrock of our research, aiming to explore the potential applications of ML algorithms in studying treatment response of PGLL tumors.

Thesis Objectives

Main Objective:

This thesis is dedicated to providing a thorough examination of the responses exhibited by paraganglioma (PGL) tumors to precision treatment with sunitinib, with a primary emphasis on incorporating advanced machine learning techniques. Employing molecular-dynamic PET, vascular UUDI, and morphological CT images, the research navigates the intricate interplay between metabolic heterogeneity and vasculature, aiming to pinpoint key subregions responsible for driving resistance to sunitinib. The central objective is to unravel the nuanced dynamics of how PGL tumors evolve over time in response to sunitinib therapy, moving beyond conventional growth metrics. By gaining a deeper understanding of the tumor's characteristics through multi-modal imaging and machine learning, the study aspires to contribute transformative insights into the precision treatment landscape for PGL.

Key Objectives:

Objective 1. Employ multi-modal tumor imaging and machine learning techniques to track and understand how PGL tumors evolve over time in response to sunitinib therapy. This includes exploring various imaging modalities, such as molecular-dynamic PET and vascular UUDI, to gain a nuanced perspective of the tumor's characteristics.

Objectif 2. Partition PGL tumors into metabolically consistent subregions using clustering algorithms. This objective aims to better understand tumor heterogeneity and identify subregions driving resistance to sunitinib. Integration of this data enhances the accuracy of pinpointing high-risk areas within PGL tumors.

Objective 3. Develop and apply a 3D-U-Net network tailored to the specific requirements of PGL tumor analysis. This network will automate the identification of high-risk subregions based on the complex interplay between metabolic and vascular characteristics, potentially revolutionizing the precision of response assessment.

Objective 4. Explore the utility of radiomic features for predicting treatment response in PGL tumors. Assess which radiomic features are most indicative of sunitinib treatment re-

sponse and how these features correlate with changes in metabolic and vascular parameters over time.

In summary, the thesis aims to bridge the knowledge gap regarding sunitinib resistance in PGL tumors, with a focus on the intricate interplay between metabolic heterogeneity and vascular parameters. The research aspires to lead to more effective and personalized treatment strategies for individuals impacted by PGL, ultimately advancing the landscape of precision treatment in the context of PGL.

Chapter 2

Review of Literature

2.1 Overview of Medical Imaging in Cancer Diagnosis

2.1.1 Review the different molecular imaging modalities commonly used in cancer diagnosis and their strengths and limitations (e.g. PET, etc.)

Molecular imaging serves as a noninvasive medical imaging technique, facilitating the visualization, analysis, and quantification of biological activities occurring at the molecular and cellular tiers within tumors ([106], [107]). Unlike conventional imaging methods that primarily capture structural disparities in tissues or organs, molecular imaging unveils the functional behaviors or manifestation status of particular molecules within a tissue or organ. This is achieved by utilizing medical imaging technologies, whether with or without the incorporation of tracers, substances that can spotlight distinct molecules. By employing these methods, a deeper understanding of the complex molecular mechanisms that govern physiological functions becomes evident. This provides a unique viewpoint into the progression of diseases, the reactions to treatments, and the efficiency of interventions.

Starting from the discovery of magnetic resonance spectroscopy in 1966 [108], moving through the creation of the first Single Photon Emission Computed Tomography instrument in 1976 [109], followed by the introduction of the first whole-body MRI scanner in 1977[110], and using luciferase as a tool to monitor gene expression in live organisms in 1986 [111], along with the development of Near-Infrared Fluorescence (NIRF) imaging in 1994 [112] – these milestones have paved the way. The culmination occurred when the first PET-CT system, effectively combining functional and anatomical imaging, became a clinical reality in 1998 [113]. Building upon this, human usage of photoacoustic imaging was initiated in 2002 [114], followed by the proposal of NIR-II imaging in 2009 [115]. These significant historical advancements collectively have propelled the evolution of molecular imaging Fig.2.1.

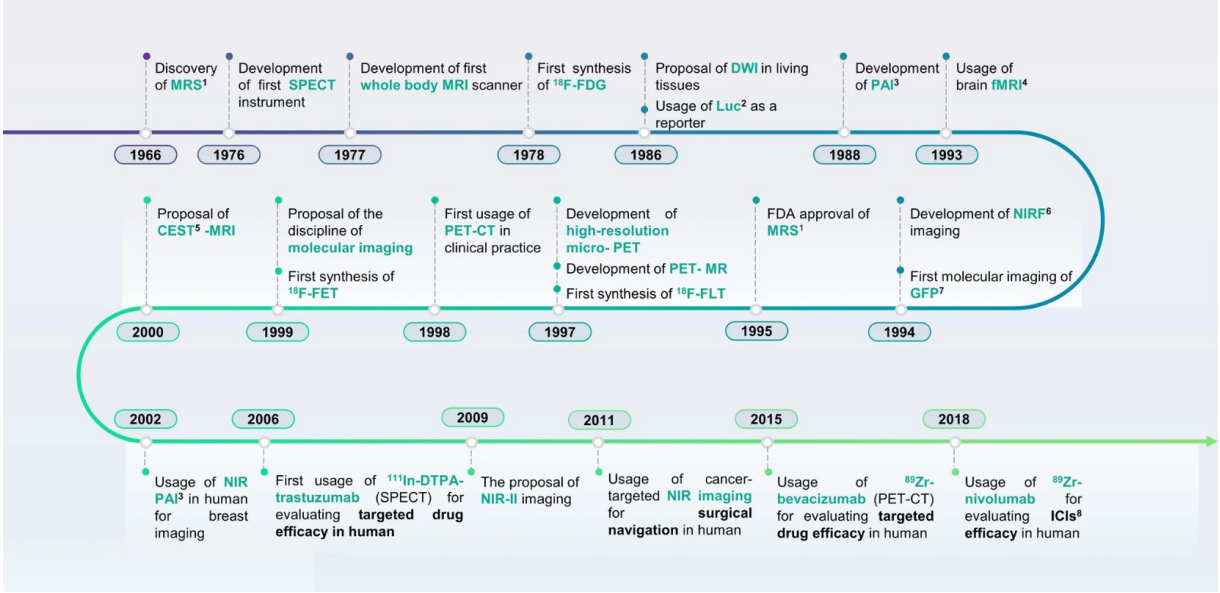

Figure 2.1: The historic steps in molecular imaging technology. Adopted from [1]

2.1.2 Imaging of PGL

Imaging is crucial in the evaluation of paraganglioma tumors due to their diverse locations and potential hormonal activity. It plays a vital role in precisely locating and characterizing these rare neuroendocrine tumors, staging them to guide treatment decisions, and monitoring treatment response and long-term outcomes. Imaging also aids in planning surgical interventions, guiding procedures, and assessing the risk for familial paraganglioma syndromes, ultimately improving patient care in the management of these tumors.

Anatomical vs. functional imaging

According to the clinical guidelines of the Endocrine Society, the primary method recommended for investigating the localization of biochemically confirmed PPGL is a CT of the abdomen and pelvis [24]. Existing literature suggests that both CT and MRI are suitable for preoperative localization but are inadequate for diagnosing metastatic PPGL and are therefore suboptimal for follow-up purposes.

In a study conducted by Maurea and colleagues, CT and MRI demonstrated significantly higher sensitivity (100%) compared to the 82% sensitivity of 123I-Meta Iodo Benzyl Guanidine (MIBG) scintigraphy in the preoperative assessment. After surgery, the sensitivity of MRI and 123I-MIBG scintigraphy was 85%, surpassing that of CT at 77%. Notably, 123I-MIBG scintigraphy exhibited exceptional specificity, achieving 100% accuracy in both pre- and postoperative evaluations [116].

However, in more recent investigations that directly compared functional imaging methods, 123I-MIBG scintigraphy was found to be less effective than other imaging techniques

in detecting PGL or metastatic disease, particularly in cases involving SDHx-related tumors. Rufini et al. conducted a prospective study of 12 patients with known or suspected recurrent PGL after tumor resection. They found that 18F-DOPA PET-CT showed a sensitivity of 100%, in contrast to 123I-MIBG scintigraphy, which had a sensitivity of 75% [117]. Notably, the sensitivity of 123I-MIBG scintigraphy was reported to be less than 50% in patients with SDHx mutations, which presents a significant limitation [24, 118].

In a recent multicenter retrospective study by Rao et al., it was suggested that additional 123I-MIBG scintigraphy imaging, when added to CT or MRI, does not provide a benefit in the preoperative setting and might even lead to incorrect clinical decisions. The authors recommended reserving the use of 123I-MIBG scintigraphy for cases where treatment with 131I-MIBG is planned [119].

Customized Selection of Imaging Methods

Observations from clinical practice reveal that the sensitivity of functional imaging varies depending on the underlying hereditary syndrome. In an extensive comparative study conducted by Timmers and colleagues, various imaging techniques were evaluated for their sensitivity. This study involved 52 patients, including 20 with non-metastatic PPGL, 28 with metastatic PPGL, and four patients in whom PPGL could be ruled out. Each patient underwent a comprehensive set of anatomical and functional imaging assessments, with the exception of a few cases. Specifically, three patients with metastatic PPGL did not undergo 123I-MIBG scintigraphy, and one patient with metastatic PPGL did not undergo 18F-FDG PET/CT. The results of this study led the authors to propose specific imaging choices based on the hereditary syndrome.

For cases of metastatic PGL with an unknown hereditary syndrome, the authors recommend 18F-FDA PET as the imaging modality of choice. In contrast, for SDHB mutation carriers, they suggest using 18F-SDH or 18F-FDA PET. Additionally, for non-SDHB mutation carriers, the authors advocate for the use of 18F-DOPA or 18F-FDA PET instead of 18F-FDG PET. In a separate study by Timmers and colleagues, various functional imaging methods were compared in 30 patients with SDHB-associated PPGL. Notably, 18F-FDG-PET/CT demonstrated a sensitivity of nearly 100% in patients with SDHB mutations, implying that 18F-FDG PET is the preferred imaging approach for SDHB-associated metastatic PGL [120, 31].

Imaging of Angiogensis (Ultrafast Doppler and Others)

Tumor growth relies on angiogenesis, and targeted anti-angiogenic therapies are essential for managing tumor progression and metastasis. To assess the efficacy of these treatments, in vivo imaging techniques are employed, with three main categories of modalities: non-optical methods (e.g., CT, MRI, ultrasound, and PET), optical methods (including fluorescence, multiphoton, and laser speckle contrast imaging), and hybrid methods (such as photoacoustic imaging).

Dynamic-enhanced CT and MRI (Dynamic Contrast Enhanced (DCE)-MRI)

CT relies on X-ray attenuation for visualization, allowing the imaging of large vessels like the coronary artery [121] with resolutions down to 1 m [122]. Dynamic-enhanced CT involves acquiring 3D volumes post-contrast injection, facilitating the calculation of parameters like blood flow, blood volume, mean transit time, and capillary permeability to explore tissue microcirculation [123]. Relationships between CT perfusion parameters and tumor angiogenesis have been established, making it useful for diagnosing PGLs [124]. However, CT perfusion exposes patients to ionizing radiation.

MRI is based on proton behavior in a magnetic field, providing excellent soft tissue contrast. Dynamic contrast-enhanced MRI uses contrast agents to estimate angiogenesis by measuring changes in blood volume. Quantification involves various parameters, including Ktrans and incremental Area Under Curve (AUC), preferred for describing the effects of antiangiogenic drugs in solid tumors [125]. While Dynamic contrast-enhanced MRI has been less explored in PGLs, it has potential limitations such as lengthy scanning times, non-portable equipment, cost, sensitivity to motion artifacts, and lack of real-time scanning capabilities. Its application in a PPGL mouse model is currently under investigation.

Functional radiotracers of angiogenesis

In molecular imaging, targeted molecular approaches are used to characterize vessels expressing VEGF receptors (Type 1, 2, and 3), integrins, and matrix metalloproteinases . Receptors of Vascular Endothelial Growth Factor (VOI)1 and VOI2 play distinct roles in angiogenesis, with VOI2 being associated with cancer and poor prognosis [126, 127], making it a target for specific radiotracers [128]. For example, radiolabeled bevacizumab has been employed to study the impact of antiangiogenic treatments[129]. VOI-2 can also be linked to microbubbles for enhanced sonography in angiogenesis visualization [130]. However, these approaches are not widely adopted.

Integrin-specific radiotracers are more commonly used, especially those targeting αv β3 integrins. These glycoproteins are expressed on growing vessel endothelial and tumor cells [131]. Radiotracers containing the RGD domain, such as 18F-Galacto-RGD and 18F-Fluciclatide, have been used to image angiogenesis [132]. However, the molecular mechanism of radiotracer-integrin uptake is not fully understood and can be influenced by factors like integrin activation status.

While nuclear imaging and MRI are effective, they are costly and can involve high doses of contrast agents, which may be toxic. In contrast, ultrasound and optical methods are more affordable, with ultrasound being readily available to clinicians and offering deeper tissue penetration compared to optical methods.

Ultrasonography for Assessing Tumor Angiogenesis

Ultrasonography has a rich history in clinical practice, dating back to the 1970s, and has

seen significant advancements, such as the introduction of Doppler imaging for blood flow assessment and elastography for tissue stiffness visualization. While ultrasound imaging was initially underestimated in oncology patient care due to its limitations compared to techniques like CT and MRI [133], it has since gained recognition for its clinical utility. These limitations included high inter-operator variability, a restricted field of view, and an inability to provide information on lung and bone conditions. However, advances in US technology, particularly with GPUs, have led to its reevaluation as a cost-effective, highly available, and repeatable imaging method. Significant clinical progress has been made since 2012, particularly in contrast-enhanced Ultrasound (US), molecular US for diagnosis and therapy monitoring, and focused US and sonoporation for therapy [66].

Before 2012, Doppler US was primarily used to visualize arterioles and venules, and microbubbles in CEUS were essential to image capillaries. Imaging tumor vascularization posed challenges due to tumor heterogeneity and variable arterial pressure. The first Doppler US examination of tumor angiogenesis successfully differentiated between benign and malignant breast tumors [134]. Doppler US allowed for non-invasive evaluations of responses to anti-angiogenic drugs and therapeutic efficacy [135]. Correlations between Doppler flow and microvascular density measured by histology established links between functional and anatomical parameters under anti-angeogenic treatment [136], although not consistently [137]. Recent developments in 3D vascularization imaging with high-frequency US allowed for specific vascular measurements.

Doppler US is currently used for tumor diagnosis in various cancer types and monitoring the effects of AA treatments in preclinical studies. Dynamic Contrast Enhanced US has been successfully used in clinical settings to evaluate tumor responses to anti-angiogenic therapy [138, 139].Dynamic Contrast Enhanced US provides functional and quantitative information about solid tumor perfusion using microbubble agents. These microbubbles can be targeted in preclinical studies and non-targeted in clinical practice. DCE-US quantifies blood volume (BV), blood flow (BF), and Mean Transit Time (MTT = BV/BF). DCE-US offers rapid acquisition compared to DCE-CT and DCE-MRI, with parameters like AUC at day 30 correlating with overall survival and freedom from progression under anti-angiogenic treatment [140, 141]. Additionally, MTT has shown potential as an early DCE-US biomarker, correlating with freedom from progression, particularly in metastatic colon and breast cancer[141], possibly due to vessel normalization during which vessels have shorter branches and shunts, theoretically enhancing drug delivery efficiency [142].

2.1.3 Different criteria to evaluate metabolic tumor response: PERCIST and RECIST

In the era of precision oncology, monitoring the tumor response, after anti-cancer treatment, is a vital step to be early carried for taking the 'go' vs 'no go' decision. Monitoring tumors is essential to detect drug resistance that can occur at any time during the treatment and can vary from one patient to another. Various methods have been developed to assess the response to treatments since 1976 where original reports were written by Moertel after the physical examination. In 1979 the first standard treatment response criteria: WHO

criteria was developed [143]. It uses 2 dimensional measurement to measure the size of the lesion by multiplying the longest diameter to its perpendicular diameter. It classifies the response to complete, partial, no change and progressive disease. In spite of that, WHO criteria didn't succeed to have a fully standardized response assessment since it was not explicit on the following factors: how small a lesion could be measured, how progression should be defined, and how many tumor foci should be measured. In 2000 the use of 'WHO' criteria dropped with the arrival of the Response Evaluation Criteria in Solid Tumors (RECIST) [144]. RECIST specified the number of lesions to assess (up to 10 target lesions, up to 5 per organ), it based the lesion measurement on 1 dimension of the long axis of the tumor, and it specified the minimum size of the lesions to be assess (typically 1 cm using CT scan). RECIST criteria got revised in 2008 to release its new version RECIST 1.1. By that time, the use of imaging modalities got spread wider and new drug classes were developed based on greater understanding of the tumor biology. On the light of this, it became clear that there is no response criteria to be generalized for all tumors. For example, RECIST showed low reliability in non-small cell lung cancer, prostate cancer, gastrointestinal stromal tumor, soft tissue sarcoma [145]. In 2009 with the wider availability of PET scan, PET Response Criteria in Solid Tumors (PERCIST) got released where the response to therapy is assessed as a continuous variable and expressed as percentage change in SUL peak (or sum of lesion SULs) between the pre- and post-treatment scans [146].

2.2 Artificial Intelligence (AI) in Medical Imaging

2.2.1 Review of AI Techniques for Medical Image Processing in Cancer

AI refers to a branch of computer science that aims to replicate human-like intelligence and capabilities in machines [147]. The origin of AI can be traced back to the early 20th century, with significant developments occurring in subsequent decades. In 1943, the first publication on AI surfaced, involving a neural network model applied to chess. The formal establishment of AI as an academic discipline occurred in 1957, marking the beginning of its evolutionary journey toward its contemporary understanding. However, the history of AI has also been marked by periods of stagnation referred to as "AI winters." These were characterized by reduced funding and enthusiasm for AI research due to unmet expectations and challenges. One such period occurred in the 1970s through the 1990s, primarily attributed to setbacks in machine translation and the limitations of neural networks for solving complex problems. Despite these setbacks, AI experienced a revival in the late 1990s and early 2000s, driven by advancements in computational power, algorithmic innovations, and the availability of large datasets. During this period, machine learning methods like support vector machines gained prominence for various pattern recognition applications. However, the superior performance of neural networks in certain domains, as demonstrated by ([148] and [149]), sparked renewed interest in AI's potential. The convergence of technological advancements, such as fast Graphics Processing Units (GPU)s, the development of sophisticated AI models, and the rise of "big data," contributed to a resurgence of interest and investment in AI ([148] and [150]) . It emerged as one of the pivotal tech-

nologies with far-reaching applications across industries, including healthcare. Medicine underwent a similar transformation, becoming more technology-driven, efficient, and digitized. Within medicine, imaging experienced remarkable progress, with the integration of AI technologies. The application of AI to medical imaging gained substantial attention, as AI-powered tools could enhance diagnostic accuracy, streamline workflows, and support clinical decision-making. Interestingly, AI's integration into medical imaging began earlier in radiology than in nuclear medicine Fig.2.2. This distinction can be attributed to several factors. Radiology traditionally offered larger and more accessible datasets, making it conducive to AI development. Additionally, the higher standardization in radiological procedures compared to the greater variability in nuclear medicine contributed to AI's earlier success in radiology.

Therefore, AI's integration with medicine, particularly in medical imaging, highlights its capability to reshape healthcare by enhancing diagnostics, tailoring treatments, and optimizing data handling. The growing use of AI in medical imaging is a dynamic field positioned to revolutionize patient care and elevate the precision of diagnostics.

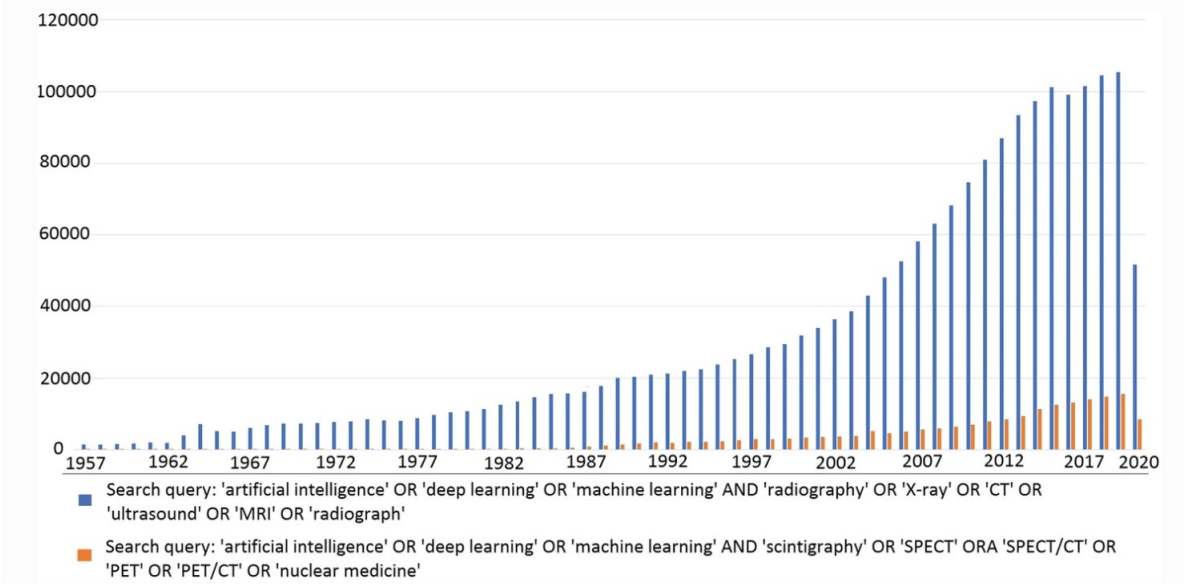

Figure 2.2: Evolution of Research Publications in AI-Driven Applications for Radiology and Nuclear Medicine Imaging over Time. Adopted from [2]

Machine learning can be employed in various ways to progress and enhance cancer imaging. Fig. 2.3 outlines the typical clinical pathway for a cancer patient and emphasizes specific perspectives of imaging where AI systems can make a beneficial difference [151]. In this thesis we will be focusing on the Disease progression block.

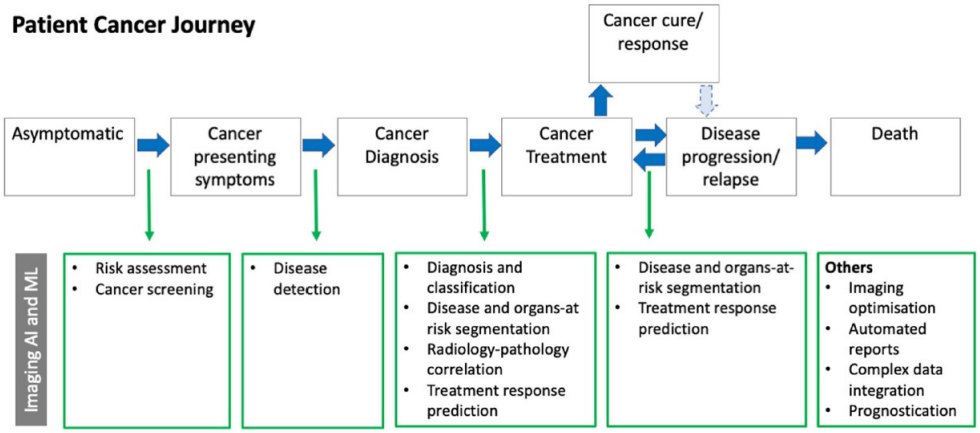

Figure 2.3: In the usual course of events, a patient who initially shows no symptoms will eventually develop cancer, manifesting signs that typically prompt the diagnosis of the disease. After undergoing proper disease staging, cancer treatment initiates, with the potential for a favorable response or even a complete cure. Nevertheless, certain patients may experience a relapse or continued progression despite ongoing treatment, necessitating additional therapeutic interventions. Sadly, some patients may ultimately lose their battle against the disease. Adopted from [3]

Extracting and analyzing quantitative information from nuclear imaging data is a standard practice. Traditional semi-quantitative parameters like SUV, Metabolic Tumor Volume (MTV), Total lesion glycolysis (TLG), and absolute quantitative values (e.g., glomerular filtration rate, coronary blood flow) are obtained through the application of appropriate image correction and reconstruction algorithms, combined with tracer kinetic modeling techniques [152]. Features manually extracted from images can be incorporated into AI-based systems, enhancing personalized medicine by supporting diagnosis and treatment guidance [153].

2.2.2 AI Applications in Medical Imaging for Cancer Staging, Treatment Response Prediction, and Targeted Therapy Assessment

AI is well-suited to address the challenges posed by modern targeted therapies, which often deliver significant clinical benefits not effectively captured by RECIST-based endpoints, relying on the assumption of uniform tumor shrinkage. Targeted therapies produce unique response patterns that confound these endpoints, contributing to high clinical trial failure rates and drug development costs. AI's capacity to quantify various biological response processes, beyond tumor size, is pivotal in addressing this need. Artificial intelligence, through advanced imaging and data analysis techniques, can capture and analyze a broader spectrum of information from medical images. It can discern subtle alterations in tumor morphology, texture, and density, providing a more comprehensive view of the tumor's response to treatment. This ability is especially valuable in scenarios where tumors may

not shrink significantly but still exhibit positive responses, such as decreased vascularity, increased necrosis, or alterations in cellular structure. Moreover, artificial intelligence has been employed to forecast cancer outcomes, including local and distant control and survival, across various treatment modalities, such as radiotherapy, chemotherapy, targeted molecular therapy, and immunotherapy.

In the context of predicting treatment response, [154] introduced a machine learning algorithm to identify the optimal prognosis index for brain metastases, primarily in Non-Small Cell Lung Cancer (NSCLC) patients. They employed seven clinical and qualitative features and seven supervised machine learning algorithms to predict patient prognosis. Their approach, Mutual Information and Rough Set with Particle Swarm Optimization, outperformed conventional statistical methods, achieving the highest accuracy in survival prediction with an AUC of 0.978 ± 0.06.

Furthermore, deep learning, including the U-Net segmentation algorithm, has been employed to identify numerous survival-related PET and CT features with significant prognostic value. These features correlated strongly with 2- and 5-year overall survival and disease-specific survival, and spatially corresponded with regions indicating a higher likelihood of metastasis or recurrence [155].

AI analysis of quantitative imaging data has the potential to enhance the evaluation of responses to targeted therapy. For instance, in a study involving NSCLC tumors treated with bevacizumab, a monoclonal antibody targeting VEGF, a reduction in fluorodeoxyglucose uptake revealed a higher number of patients responding to treatment compared to traditional CT criteria (73% vs. 18%). Remarkably, in this study, neither PET nor CT was correlated with overall survival (PET, $P = .833$; CT, $P = .557$) [156].

Deep Learning (DL) can also be applied for the analysis of medical images across different time points to forecast treatment response. For instance, Convolutional Neural Networks (CNNs) were employed in breast dynamic contrast-enhanced MRI (DCE-MRI) to evaluate the response to neoadjuvant chemotherapy. In this application, the inputs encompassed variations across contrast time points and treatment examination times [157]. [158] conducted research to investigate the potential of deep learning using CNNs with pre- and post-treatment CT scans of patients with bladder cancer. Their aim was to aid in evaluating treatment response and, additionally, to enhance the prediction of a tumor's prognosis, which is valuable for making treatment decisions and estimating survival outcomes.

2.2.3 Assessing Intra-tumor Heterogeneity Through Medical Imaging

Medical imaging also plays a crucial role in quantifying the intra-tumor characteristics. Studies involving the sequencing of multiple, distinct samples from the same tumor have revealed that Intra-Tumor Heterogeneity (ITH) is a common occurrence in solid tumor cancers. Intra-tumor spatial variations could involve different factors like cellularity, angiogenesis, the extracellular matrix outside blood vessels, and regions of necrosis. Tumors that have a lot of these variations tend to be associated with a worse outlook for patients,

possibly due to their aggressive nature or resistance to treatment [159, 160]. Trying to understand these variations through random tissue samples or biopsies is challenging because they don't capture the full range of differences in how tumors look and behave. So, finding a non-invasive way to study these differences within a tumor could be very useful in the era of personalized medicine. This could help doctors identify patients with a poor prognosis who might benefit from more aggressive treatments. Therefore, looking at the diversity within tumors is a crucial aspect of medical imaging that could be measured and enhance the way we typically report on tumors.

To date, several Computer Aided Diagnosis (CAD) for sub-regional analyses based on radiology imaging features have shown to significantly improve diagnostic performance. In breast cancer,[161], proposed an unsupervised clustering algorithm for 4-D imaging that integrates Markov-Random Field image segmentation with time-series analysis to characterize kinetic ITH. In sarcoma, [162] showed that heterogeneity analysis is a strong independent predictor of patient outcome. In lung cancer,[163, 164] performed a multi-level segmentation based on PET and CT images to identify high risk sub-region that better improved the lung cancer prognosis. Additionally, [165] showed that sub-regional image features analysis of PET/CT predicts patients survival better than those from the whole tumor in nasopharyngeal carcinoma. However, to the best of our knowledge, to date, the possibility that sunitinib resistance in PPGL could be conditioned by particular intra-tumor regions rather than by a global action of the tumor has not been explored. In another study of 54 patients with NSCLC undergoing PET-CT staging, a heterogeneous texture on the non-contrast-enhanced CT component of the PET-CT was a predictor of poorer survival; in particular, patients with coarse texture uniformity $<$0.624 did not survive more than 2.5 years [166]. Similarly, in a study of 21 patients with primary esophageal cancer undergoing PET-CT staging, advanced stage tumors demonstrated greater heterogeneity at filter values 1.5–2.0. Survival was also poorer for more heterogeneous tumors, particularly for coarse texture uniformity $<$ 0.8477 (odds ratio = 4.45, 95 % Confidence Interval 1.08–18.37, p = 0.039) [166].

2.3 Radiomics in Cancer Imaging

The transition from traditional semi-quantitative parameters to radiomics in medical imaging is driven by the pressing need for a more advanced and comprehensive approach to image analysis. Traditional semi-quantitative parameters, while valuable, often provide a limited and somewhat subjective perspective on the information contained within medical images. They typically involve manually assessing a few specific visual characteristics, which can introduce interobserver variability and may not capture the full complexity of the underlying tissue or pathology.

Radiomics, on the other hand, revolutionizes image analysis by harnessing the power of advanced computational techniques. It enables the extraction of a multitude of quantitative features from medical images, encompassing not just simple measurements but also intricate textures, shapes, and statistical properties. This quantitative richness offers a far more detailed and objective view of the imaged structures, making it an indispensable tool

for improving diagnostic accuracy and treatment planning.

In metabolic imaging, textural features have shown superior performance in predicting treatment outcomes compared to simple SUV measures like SUVmax and SUVmean, as demonstrated by various studies [162, 167, 168]. For instance, [169] conducted a study involving fifty-three NSCLC patients and compared the predictive capabilities of maximum and mean SUV with four Neighboring Gray Tone Difference Matrix (NGTDM)-derived textural features. They discovered that coarseness, busyness, and contrast, derived from NGTDM, exhibited better discrimination between responders and nonresponders to chemoradiotherapy compared to the aforementioned SUV metrics. Furthermore, coarseness emerged as an independent predictor of overall patient survival. In another study by [170] multiple multivariate models were developed to forecast pathologic responses to preoperative chemoradiotherapy in twenty esophageal cancer patients. Their findings revealed that models incorporating combined radiomic features significantly enhanced pathologic response prediction, surpassing models built solely on maximum SUV, metabolically active tumor volume, and longest diameter.

In the context of anatomical imaging [100], the prognostic potential of 440 shape, intensity, and textural features in CT imaging was assessed, focusing on survival prediction for over 420 lung cancer patients within a discovery dataset. These features' prognostic value was subsequently validated across three independent datasets, encompassing one lung cancer cohort (225 patients) and two head-and-neck cancer cohorts (231 patients). The findings not only affirmed the applicability of radiomic features in predicting outcomes and characterizing intra-tumor heterogeneity but also indicated the transferability of prognostic ability between different disease types, such as from lung to head-and-neck cancer.

In the context of vasculature imaging, Recent investigations have established a robust link between the heterogeneity of tumor vasculature and contrast-enhanced (CE)-CT, as documented in studies by [171, 172] identified a significant correlation between tumor blood flow, assessed through CE-CT, and the metabolically active tumor volume. This highlights the potential of CE-CT radiomics in quantifying the intricate tumor phenotype influenced by angiogenesis in cancer. For instance, [173] proposed that if the fractal dimension, extracted from CE-CT, effectively characterizes tumor heterogeneity, it might also serve as a predictor of patient survival in hepatocellular carcinoma. Their findings indicated that patients with longer survival tended to exhibit lower fractal dimension values in the arterial phase CE-CT images, suggesting its potential as a prognostic marker [173].

2.3.1 Radiomics for PGL tumor

While research on radiomics in patients with PPGL has been limited, recent studies have demonstrated its potential in distinguishing subclinical pheochromocytoma from lipid-poor adenoma, a challenging task for conventional imaging analysis [174, 175]. These encouraging findings provide a robust basis for the utilization of radiomics in predicting the metastatic potential of PPGL. Another study explored the utility of FDG-PET/CT-based radiomics in characterizing and genetically orienting pheochromocytomas before surgical

intervention. Radiomics, is employed to differentiate between subclinical pheochromocytomas and lipid-poor adenomas. The study presents promising results, suggesting that radiomics can help predict the metastatic potential of pheochromocytomas, providing a valuable foundation for further applications in pre-surgical assessment and genetic guidance for these tumors [176].

2.3.2 Radiomics Analysis of Intra-tumor Heterogeneity in Cancer Imaging

Within the realm of radiomics for intra-tumor heterogeneity, these studies present compelling perspectives. The investigation in esophageal cancer taps into textural features from baseline 18F-FDG PET images, demonstrating their potential as robust predictors of treatment response, surpassing traditional metrics like maximum SUV [**ixier2011intratumor**]. This advancement holds promise for refining tailored treatment strategies, ultimately enhancing outcomes. A parallel exploration in cervical cancer conducts a comprehensive temporal analysis, particularly emphasizing textural features' role in characterizing intratumor metabolic heterogeneity [168]. By scrutinizing how metabolic patterns evolve over time, the study uncovers valuable insights for predicting treatment responses and disease progression, offering a tailored treatment approach. Meanwhile, a distinct study introduces the concept of "Functional 4-D clustering," exploring intra-tumor heterogeneity in dynamic medical imaging [161]. The focus lies on its application in FDG PET scans, assessing whether these dynamic changes, when analyzed through radiomics, can serve as valuable prognostic biomarkers for breast cancer. This approach, by quantifying intra-tumor variations, holds the potential to revolutionize breast cancer prognosis and therapy.

Nonetheless, a persistent challenge in radiomics pertains to the interpretability of these features [153]. The interpretability of these features is profoundly influenced by the computational method employed, whether it involves conventional parameters, first-order descriptors, shape and size characteristics, or more advanced techniques such as Laplacian or wavelet features. Another significant challenge is the quality and variability of medical imaging data, as even slight variations in acquisition parameters and image quality can impact the reliability of radiomic features. Standardization is another issue, with the lack of consistent protocols making it difficult to compare results across different studies and institutions, hindering the establishment of universal benchmarks. Moreover, the need for large datasets for training and validation poses a limitation, as smaller sample sizes can lead to overfitting, reducing the generalizability of radiomic models. Additionally, the integration of radiomics into routine clinical practice faces regulatory, technical, and workflow challenges. Ensuring data privacy and security and developing interpretable AI models are other key considerations. Finally, the cost and resource requirements, as well as the need for longitudinal data, are aspects that must be taken into account to fully harness the potential of radiomics for improving patient care and advancing medical research

2.4 Preceding Study

In a previous study led by Caterina Facchin, a former PhD student in our research team, she utilized PET/CT/UUDI co-registration to delve into the intricate dynamics of Sdhb-/- tumors [69]. The results unveiled a rapid expansion in these tumors, characterized by heightened glycolysis and increased vascularization. The initial administration of sunitinib showed promising outcomes, effectively restraining tumor growth, inhibiting vessel development, and reducing FDG uptake during the early weeks (W1-2). However, subsequent imaging painted a compelling picture of an observable escape from sunitinib treatment, indicated by an increase in FDG uptake at W3, followed by a resurgence in both tumor growth and vascular development at W4-5.

A notable finding was the concentration of blood vessels in the active, sugar-consuming regions of the tumors, with their volume showing an increase during the escape from sunitinib. This observation implies a dynamic adaptation of the tumor vasculature in response to treatment. Importantly, early alterations in total lesion glycolysis and maximum vessel length at W1 emerged as crucial predictive indicators of resistance to sunitinib. These findings shed light on the nuanced interplay between tumor metabolism, vascularization, and therapeutic response, providing valuable insights into potential predictive markers for treatment resistance.

Chapter 3

PETRUS and Database Generation

3.1 Database Generation

3.1.1 Animal Modal

The database utilized in this thesis is derived from experiments previously conducted by a former Ph.D. candidate within my research team [69]. The animal experiments were conducted in compliance with ethical guidelines and received approval from the French Ethical Committee under reference number 16-098, following the regulations outlined in the French law of animal experimentation, specifically n°2013-118. The allograft mouse model was established by performing subcutaneous injections of immortalized mouse chromaffin cells, which carried a homozygous knockout of the Sdhb gene ($Sdhb^{-/-}$, clone 8). These cells were propagated in the fat pad of nude female mice, totaling 27 mice from Janvier Labs in France. The mice were housed and maintained under controlled conditions, including a temperature of 24°C, relative humidity of 50%, and a 12/12-hour light/dark cycle. They had unrestricted access to both food and water. Tumor volume was assessed daily using the formula: ½ × long diameter × (short diameter)². When the tumor volume reached 140 mm³, mice bearing $Sdhb^{-/-}$ tumors were randomly allocated into two distinct groups (as depicted in Figure 3.1). In one group (comprising 16 mice), an antiangiogenic treatment involving sunitinib malate (CliniSciences, A10880-500) was administered. Sunitinib malate was prepared by dissolving it at a concentration of 10 mg/mL in a mixture of Dimethyl Sulfoxide (DMSO) and PBS (in a ratio of 1:4). For the control group (comprising 8 mice), a solution of DMSO-Phosphate-Buffered Saline (PBS) (1:4) was prepared. The sunitinib-treated group received a daily oral gavage of sunitinib at a dosage of 50 mg/kg for a continuous period of 6 weeks, with each dose administered in a volume of 200 μL. The vehicle-treated group received an equivalent volume of the DMSO-PBS solution through oral administration. In cases where the tumor volume surpassed the recommendations set by United Kingdom Coordinating Committee on Cancer Research (UKCCCR) or when indications of advanced cancer disease became evident [177], humane euthanasia was carried out.

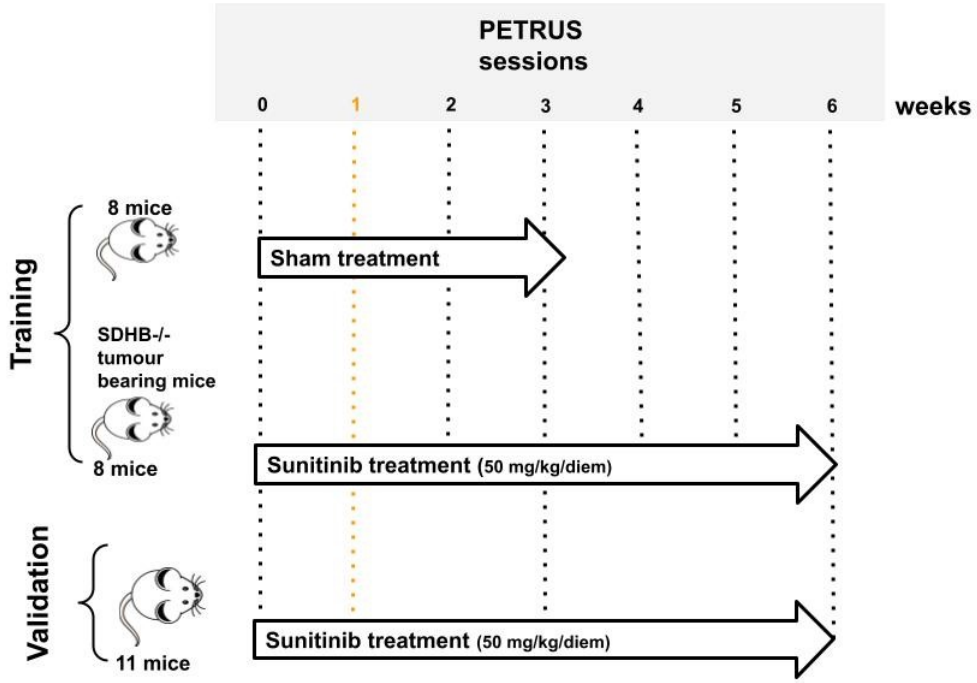

Figure 3.1: Database generation process. Mice in the training group were divided into two groups: sunitinib-treated and sham-treated. Eight mice from each group were scanned with PETRUS before and after 1, 2, and 3 weeks of treatment. Sinitinib-treated mice were also imaged at 4, 5, and 6 weeks of treatment. Mice of the independent validation set were sunitinib-treated and scanned at baseline and at weeks: 1, 3, and 6 of the treatment (adopted from [178]).

3.1.2 PETRUS acquisitions

The impact of sunitinib was assesed using PET Registered Ultrafast Sonography (PETRUS) device [179, 180], 3.2. PETRUS allows for simultaneous acquisition of tissue metabolism using [^{18}F]FDG Positron Emission Tomography, Computed Tomography (CT) and Ultrafast Ultrasound Doppler Imaging (UUDI) [179]. Thus, it simultaneously reads the cellular metabolism activity alongside micro-vascular architecture within the tumor, ensuring unimpaired physiological conditions for both sets of spatially co-registered features [69].

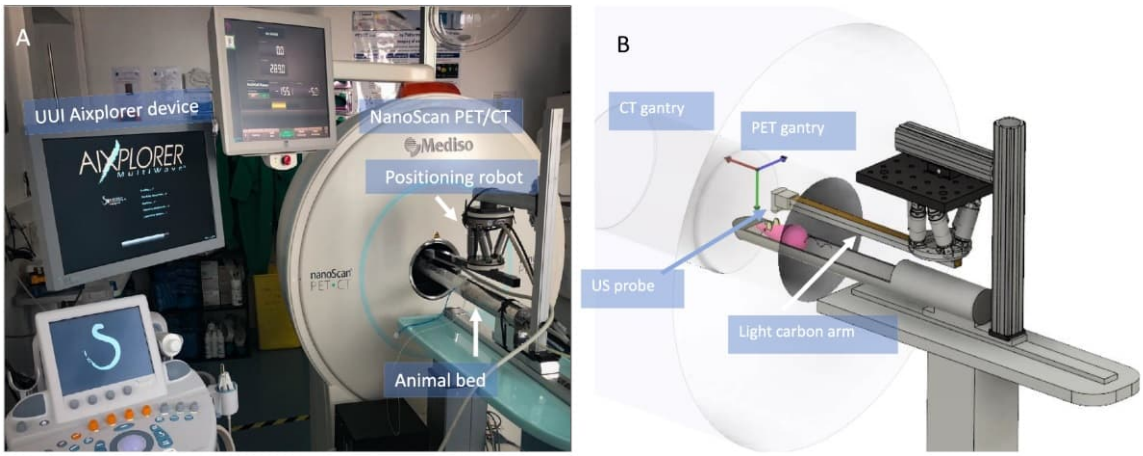

Figure 3.2: The PETRUS imaging device during acquisition. (A) Photo of PETRUS Device, (B) Schematic illustration of the setup employed for imaging mice with $Sdhb^{-/-}$ tumors. (adopted from [181]).

CT Acquisition

The CT scans were obtained in a semi-circular mode with the following parameters: 39kV voltage, 720 projections in a full scan, 300 ms per projection, and 1:4 binning. Subsequently, CT data were reconstructed using the filtered back projection technique (filter: Cosine; Cutoff: 100%) [182], resulting in a pixel size and slice thickness of 0.23 mm.

PET Acquisition

PET acquisition started 30 seconds before injection of 10 MBq of 18F-FDG in 0.2 mL saline into the mouse tail vein. List-mode PET data were collected during 60.5 min, binned using a 5-ns time window, a 400- to 600-keV energy window, and a 1:5 coincidence mode, i.e. each detector associated with the five opposite detectors. Data were reconstructed by the TeraTomo reconstruction engine (3D-OSEM based manufactured customized algorithm, Mediso medical imaging systems, Hungary). A 31-frame dynamic sequence was chosen with the following time sequence: exclusion of 20 s; 10 frames of 5 s, 5 frames of 10 s, 2 frames of 15 s, 3 frames of 60 s, 5 frames of 120 s, 3 frames of 5 min, 3 frames of 10 min.

UUDI Acquisition

The UUDI system utilizes in-house MATLAB scripts from The MathWorks in Natick, MA, USA, to execute plane wave beamforming for both transmission and reception. UUI images were captured as 2D planes measuring 12.8 x 20 mm^2 , with each plane being spaced 0.1 mm apart, all while operating in Ultrafast Ultrasound Doppler mode. The complete tumor volume image is formed by stacking together individual planes, ranging from 70 to 200

planes in total. Each of these planes was generated by averaging 300 temporal frames acquired at a frame rate of 500 frames per second. Each frame comprised images from 11 tilted plane waves, evenly distributed between -10 and 10 degrees. The Ultrafast Power Doppler volume represents the volume occupied by red blood cells flowing within the vessels. To distinguish signals originating from the tissue and blood, a spatiotemporal filter based on singular value decomposition was applied [183]. Subsequently, the power, which is equivalent to the square of the signal amplitude, was integrated over the 300 frames for each slice. Ultimately, this process yielded a 3D volume depicting vascularization, with a resolution that varies depending on the ultrasound probe's elevation focusing capability. To enhance the image quality, we conducted deconvolution on the 3D volume using a blurring kernel estimation. The kernel's calculation involved the use of the blind deconvolution method [184], applied to a B-mode 3D volume containing crossed 80-μ m copper wires immersed in water. This blurring kernel was then employed in a Lucy-Richardson deconvolution process to achieve an isotropic spatial resolution of approximately 100 μm^3 across the entire tumor.

3.1.3 Image and Data Processing

Before conducting image analysis, a precise co-registration process was carried out to align the 3D volumes of X-Ray CT, dynamic PET, and UUDI. This co-registration involved the utilization of a phantom submerged in a water bath, featuring three 80 µm copper wires that were visible in both CT and UUDI volumes, as detailed in [179].

The delineation of tumors on the CT images was carried out with reference to the fat pad surrounding the tumor. To measure the glucose metabolism in a Volume of Interest (VOI) in the PET image, we calculated the Standardized Uptake Value of Glucose (SUV) using the following formuma:

$$Standardized\,Uptake\,Value\,of\,Glucose\,(SUV) = \frac{Concentration\,of\,the\,radiotracer\,in\,the\,VOI\,(\frac{KBq}{cc})}{Injected\,dose(KBq)/\,Body\,mass(g)}$$

Subsequently, PET and UUDI volumes were subjected to cropping based on a standardized criterion derived from the segmentation of the PET image. The semi-automatic definition of PET segmentation was accomplished using iso-contours at a 30% threshold of the SUV peak [185], employing the last-time frame (50-60 minutes post-injection). The cropping of UUDI volumes was performed utilizing the mask generated from the PET segmentation. For quantifying 18F-FDG accumulation, both the mean SUV and maximum SUV (Max SUV) were calculated. Max SUV was determined as the average SUV of the five hottest pixels within the segmented tumor, a more precise criterion compared to maximum SUV based on a single pixel [186]. The software employed for quantifying PET parameters was the PMOD package (PMOD Technologies Ltd, Zürich, Switzerland).

Chapter 4

Machine Learning of Multi-Modal Tumor Imaging Reveals Trajectories of Response to Precision Treatment

In this chapter, we delve into the comprehensive research presented in the paper entitled "Machine Learning of Multi-Modal Tumor Imaging Reveals Trajectories of Response to Precision Treatment." This paper represents a significant milestone in our quest to unravel the intricacies of how tumors respond to precision treatments. The work outlined in this chapter builds upon the key insights and methodologies introduced in the paper. The central focus of this chapter is to provide an in-depth exploration of how advanced imaging techniques, coupled with cutting-edge machine learning algorithms, can revolutionize our understanding of treatment responses in the realm of precision medicine. The paper's findings have set the stage for this exploration by highlighting the potential of various imaging modalities to offer unprecedented insights into the dynamic and multifaceted nature of tumor responses to treatment.

Throughout this chapter, we will embark on a journey through the various imaging modalities utilized in the study, such as Positron Emission Tomography (PET), Ultrafast Ultrasound Doppler (UUDI), and Computed Tomography (CT). These imaging techniques are instrumental in capturing the complex interplay of metabolic, morphological, and vascular aspects within tumors.Furthermore, we will delve into the novel Machine Learning (ML) framework proposed in the paper, which plays a pivotal role in deciphering the wealth of data generated by these imaging modalities. The framework's ability to analyze and interpret this multi-modal data is at the heart of our pursuit to redefine our understanding of precision treatment responses.

In summary, this chapter represents a deep dive into the core findings, methodologies, and implications of the paper titled "Machine Learning of Multi-Modal Tumor Imaging Reveals Trajectories of Response to Precision Treatment." It is an essential component of our ongoing efforts to advance the field of precision medicine by shedding light on the intricate dynamics of tumor responses to treatment.

4.1 Materials and Methods

Figure 4.1 shows the pipeline of the framework implemented in this study that progresses from the acquisition of multi-modal image volumes to the definition of individual trajectories of response to treatment. Each element of this diagram will be described in the following sections.

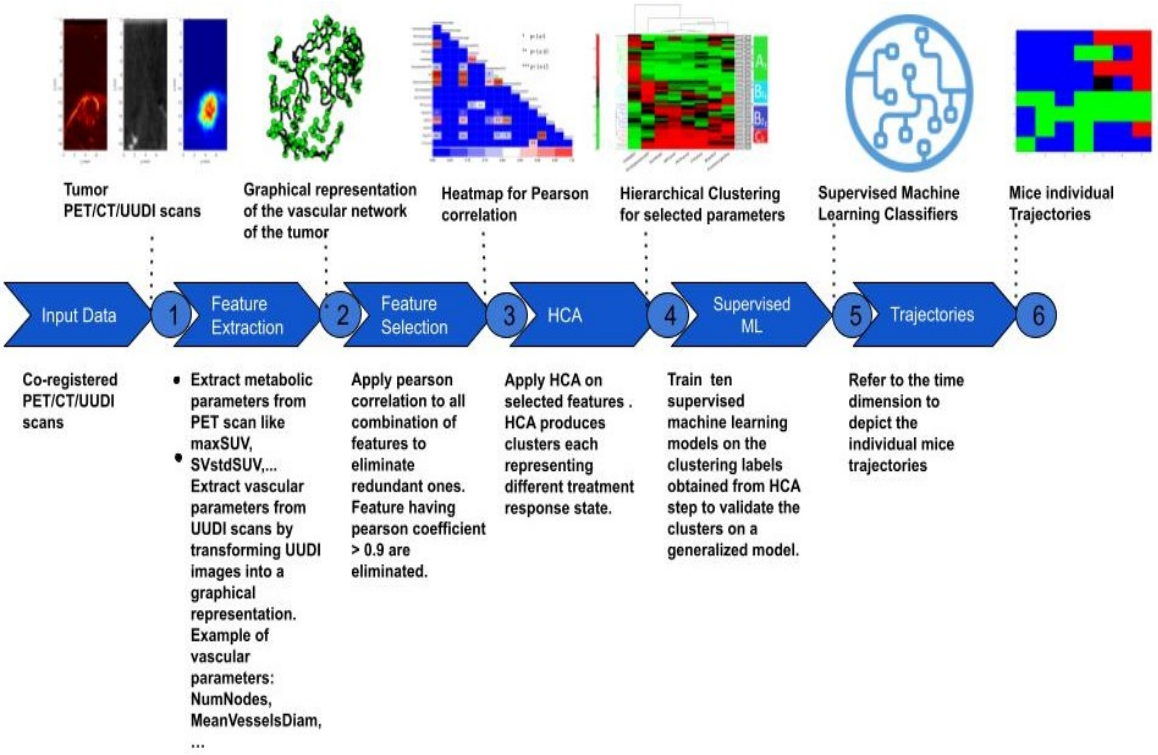

Figure 4.1: Process diagram showing the framework pipeline. Images were co-registered and processed to extract features describing the metabolic, vascular, and anatomical components of tumor development. A Pearson correlation study was performed to remove redundant features. Longitudinal features were combined, and hierarchical clustering HCA analysis was applied to obtain clusters and classes representing different stages of tumor evolution. The clusters and classes identified with HCA were used with 10 different supervised machine-learning classifiers for model generalization and final validation. Finally, time-wise concatenation of the identified stages was performed to form the individual trajectories of tumor evolution for each animal.

4.1.1 Description of Database Formation

Each PETRUS acquisition comprised three image volumes registered in a common time and space reference frame that defined a multiparametric cube surrounding the animal tumor. The features describing the metabolic, vascular, and anatomical characteristics of the tumor were extracted from the PET, UUDI, and CT images, respectively (Table 4.1). A Volume Of

Interest (VOI) covering the whole tumor was defined on the PET images by segmenting voxels with an FDG standard uptake value (SUV) greater than 30% of the tumor's peak SUV at 50–60 minutes post-injection [185]. This VOI was used to create a binary mask that was applied to the three spatiotemporal registered volumes. From the masked PET image, the following metabolic features were extracted: mean, coefficient of variance, minimum and maximum of standard uptake values (MeanSUV , CVstdSUV , MinSUV , MaxSUV), and PET volume (PETVolume). The masked UUDI volume was filtered using a Hessian-based vessel enhancement filter, and vessels were segmented using predefined thresholds [187] and skeletonized using an iterative ordered thinning-based skeletonization method [188, 189]. The skeletonized mask of vessels was transformed into a graph of nodes and edges representing the vascular network of the tumor. Using this graph, the following features describing the topology of the tumor vascularization were calculated: mean, minimum and maximum vessel length (MeanVesselsLength, MinVesselsLength, MaxVesselsLength), mean vessels tortuosity (Tort), which is the shortest distance between nodes divided by the vessel length), vessels length dispersion (VesselsLength-Disp), which is the standard deviation of the vessels length divided by the mean of the vessels length, number of nodes (NumNodes), density of nodes (DensityNodesinUSV), mean vessels diameter (MeanVesselsDiam) and ultrasound volume (USVolume), which is the number of voxels of the vascular skeleton multiplied by the voxel volume. The quantification of PETRUS images was performed using MATLAB version R2021b. The CT volume (CTVolume) was delineated from the fat pad surrounding the tumor.

The working database assembled all 15 features extracted from the imaging modalities, as well as a unique record number that defined the mouse, the week of the imaging session (where week zero (W0) is the pre-treatment imaging session and W1-6 is the rest of the treatment weeks), and the treatment group assignment (CON for sham-treated mice; SUNI for sunitinib-treated mice). Data were divided into 3 subgroups, (i) $D^{suni}_{training}$ containing the SUNI mice in the training group, aggregating a total of 54 records (ii) $D^{con}_{training}$ containing the CON mice from the training group, forming a total of 27 records, and (iii) $D^{suni}_{validat}$ containing the SUNI mice from the validation group forming a total of 28 records.

Table 4.1: PET/CT/UUDI extracted features.

Parameter	Modality	Abbreviation	Unit	Description
Mean Standardized Uptake Value	PET	MeanSUV	a.u.	Average of the Standardized Uptake of FDG in the VOI
Max Standardized Uptake Value	PET	MaxSUV	a.u.	Average of the 5 hottest pixels in the tumor VOI
Min Standardized Uptake Value	PET	MinSUV	a.u.	Minimum Standard Uptake of FDG in the VOI

Standardized Uptake Value of FDG dispersion	PET	CVstdSUV	a.u.	Coefficient of variance of the Standardized Uptake Value
PET volume	PET	PETvolume	mm^3	Number of voxels in the VOI × volume of a voxel
Computed Tomography Volume	CT	CTVolume	mm^3	Tumor volume defined by the CT scan
Number of Nodes	UUDI	NumNodes	nodes	Sum of all Nodes.
Number of Nodes / Vessels Volume	UUDI	DensityNodesinUSV	nodes/ mm^3	Number of nodes per unit of vessel volume.
Maximum Vessels Length	UUDI	MaxVesselsLength	mm	Average of the maximum length of all the vessels
Mean Vessels Length	UUDI	MeanVesselsLength	mm	Average of the length of all the vessels
Minimum Vessels Length	UUDI	MinVesselsLength	mm	Average of the min length of all the vessels
Length Vessels Dispersion	UUDI	VesselsLengthDisp	a.u.	Coefficient of variance of the mean vessel length
Mean Vessels Tortuosity	UUDI	Tort	a.u.	Average of all tortuosities. The tortuosity is the ratio between the length of a vessel (as an arc) and the straight-line length between its initial and final points
Mean Vessels Diameter	UUDI	MeanVesselsDiam	mm	Average of all mean Diameter

Vessels Volume	UUDI	USVolume	mm^3	Tumor blood volume defined by the Ultrasound Doppler scan

4.1.2 Feature Selection

Feature selection is an important pre-processing step that affects the accuracy and decreases the training time of any classifier. By removing non-useful or redundant features, the dimensionality of the feature space can be reduced, an essential step to improve the performance of a classifier [190]. In order to identify linear correlations between the different features, we applied a Pearson correlation using a Pearson coefficient $|r| > 0.9$ (p-value < 0.05) to dete CT redundant features [191]. In addition, non-informative features with a low coefficient of variation (CV < 0.1) were removed.

4.1.3 Unsupervised Classification: Hierarchical Clustering

One of the fundamental objectives of our study was the determination of phenotypically representative clusters, each cluster being a representative combination of metabolic, anatomical and vascular features associated with a stage of response to sunitinib. Clusters were determined by the individual response of the subject, independently of the time of treatment by assembling all the longitudinal features extracted. HCA, an unsupervised machine-learning clustering approach [84], was used to stratify the tumor response by finding common metabolic, anatomical and vascular phenotypic patterns of the image descriptors selected. The HCA was applied on each of the training datasets separately, $D^{suni}_{training}$ and $D^{con}_{training}$, in order to determine whether or not the treatment changes the time course of tumor evolution. First, the input data were standardized using the z-score. Then, the interrelationship between individual records was measured by computing the unweighted average Euclidean distance. This was followed by computing the average link as a similarity metric to define the closest pair of clusters. Finally, a heat map with dendrograms was constructed to display the patterns observed and the clusters identified. The length of the dendrogram branches connecting records and features is inversely proportional to the similarity of their profiles. Gap statistics [192] was applied in order to evaluate the optimal number of clusters, and Welch's t-test was applied to identify significantly different clusters [193]. The outcome of this analysis provided the optimal number of clusters corresponding to a particular phenotype identified for each instance in the data-base. HCA and statistical tests were implemented in MATLAB (version 2021-b) using the `clustergram`, `ttest2`, and `evalclusters` functions, respectively.

4.1.4 Supervised Classification: Model Building and Validation

To test the stability of the method, we compared the clustering results applied on an external population ($D^{suni}_{validation}$) to a classification produced as a generalization of the clustering performed on our initial population ($D^{suni}_{training}$). More precisely, we considered the clusters of the initial population ($D^{suni}_{training}$) as classes of a supervised classification algorithm to predict the classes expected in the new population ($D^{suni}_{validation}$).

Because our training dataset has an unbalanced number of instances per class, which can undermine the predictability of the models, we performed oversampling through the synthetic minority over-sampling technique (SMOTE), which balances the minority classes [194]. This technique uses the k-nearest neighbors approach to synthesize new observations based on the existing records. We applied smote using the four nearest neighbors to balance each of the four clusters (A, B1, B2, and C).

The selected features of our $D^{suni}_{training}$ were brought into ten machine learning classifiers, including Decision Tree (DT), GNB, kernel naive Bayes (KNB), Linear SVM, quadratic Quadratic SVM, k-nearest neighbors (KNN), weighted k-nearest neighbors (Weighted KNN), RF, narrow Neural Network (NN), bilayered NN. The best-performing model was selected by comparing the area under the receiver operating characteristic AUC Accuracy (ACC) values. The control parameters of the best model were further optimized by Bayesian optimization and five-fold cross-validation to evaluate the performance of the classifier. All classifiers were trained and validated using the *classification learner* application implemented in MATLAB version 2021-b.

In order to check the relative importance of each of the metabolic, vascular, and anatomical features in the classification problem, we used the predictor importance attribute associated with the RF model. The predictor importance attribute is an implicit technique performed using the RF model and is evaluated using the Gini impurity criterion index. This index is based on the principle of impurity reduction to provide the power of each feature in the classification [195].

4.1.5 Identification of Trajectories of Treatment Responses

We then tested whether the records assembled within each cluster, corresponding to a tumor state with specific biomarkers, could represent a chronological stage of tumor evolution. By referring back to the time point of each record (the week after the beginning of treatment) in both the CON and SUNI groups, the clusters were ordered chronologically, and a time-dependent trajectory was obtained for each mouse. We applied an R^2 test to the states at each of the seven time points of the study (classes obtained from the HCA, considering A = 1, B1 = 2, B2 = 3, and C = 4) to determine if these states indicated temporal stages of treatment response. Finally, the transitional matrix between clusters was analyzed.

4.2 Results

4.2.1 Pearson Correlation

Figure 4.2 shows the cross-heatmap of the Pearson correlation values (r) of CT, vascular, and metabolic features. In order to eliminate redundant features, a Pearson significance of r $>$ 0.9 and p-value $<$ 0.05 were applied to all pairs of features of the four instances. This reduced the number of vascular features from 11 to 8: MeanVesselsLength was correlated with MeanVesselsDiameter, Tort, and VesselsLengthDisp; VesselsLengthDisp correlated with MeanVesselsDiameter and Tort, and Tort correlated with MeanVesselsDiameter. Hence, MeanVesselsLength, MeanVesselsDiameter and Tort were not considered further. Applying the same Pearson r and p values reduced the metabolic features from 5 to 4: MeanSUV correlated with MaxSUV , and MaxSUV was not considered further.

With respect to vascular–metabolic correlations, interestingly, the StdSUV was significantly correlated with MeanVesselsDiam and MeanVesselsLength.

In addition, a low coefficient of variation (CV $<$ 0.1) results in a non-informative dataset from classifiers' training. Thus, features having a high Pearson correlation and a low coefficient of variation were not considered further. Overall, 8 features, including 4 vascular features, i.e., USVolume, NumNodes, DensityNodesinUSV, VesselsLengthDisp, 3 metabolic features, i.e., StdSUV , PETVolume, MeanSUV , and the CT volume, were used for all three curated databases ($D^{suni}_{training}$, $D^{con}_{training}$, $D^{suni}_{validat}$).

4.2.2 Hierarchical Clustering Approach

Sham-treated Training set ($D^{con}_{training}$)

Performing the hierarchical clustering on the $D^{con}_{training}$ dataset identified two major clusters: Clusters A_c and C_c (Figure 4.3a), where subscript c stands for the control group. They showed the following characteristics (Table 4.2):

- Cluster A_c was characterized by significantly low volumes of CT, PET, and UUDI, a high coefficient variance of the standard deviation of SUV , a low number of nodes, and a low density of nodes. This corresponds to a small-sized tumor, with low vascularization and metabolism, and a heterogeneous distribution of FDG uptake.

- Cluster C_c was characterized by high volumes of CT, PET, and UUDI, a significantly lower coefficient of variation of the standard deviation of SUV , and a high number of nodes. This cluster corresponds to a stage where the tumor has grown to a large volume, with high metabolic and vascularization activities but a low heterogeneity in the distribution of FDG uptake.

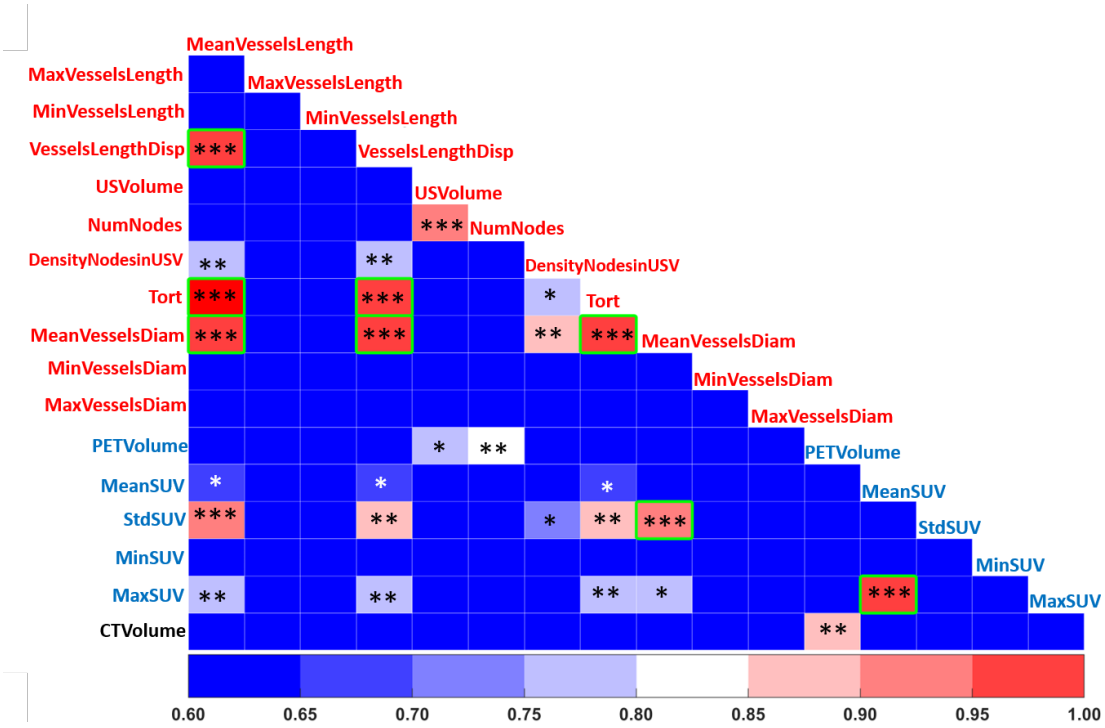

Figure 4.2: Heatmap summarizing significant Pearson coefficient values for each pair of metabolic (blue font), vascular (red font) and anatomical features (black font) used to exclude redundant features (*,**,***, refer to p-value level of significance).

Table 4.2: Metabolic, vascular, and anatomical characteristics of the clusters of the $D^{con}_{training}$ dataset. The average values of each parameter of each cluster are represented. In black, the mean values; in parenthesis, the standard mean errors; and in blue, the z-score means.

Features	**CVstd-SUV**	**Density Nodes inUSV ($1/mm^3$)**	**Num-Nodes**	**US Vol-ume (mm^3)**	**PET Vol-ume (mm^3)**	**CT Vol-ume (mm^3)**	**Mean SUV**	**Vessels Length Disp (mm^2)**
Cluster A_c	45.07 (1.68), 0.42	36.27 (1.85), −0.27	542.85 (32.84), −0.81	15.31 (1.02), 0.82	236.43 (27.75), −0.85	165.06 (23.80), −0.85	1.96 (0.10), −0.63	60.06 (1.89), 0.00
Cluster C_c	35.74 (0.89), 0.42	38.79 (1.57), −0.27	1549.29 (123.44), −0.81	39.44 (2.50), 0.82	815.28 (69.49), −0.85	584.29 (51.77), −0.85	2.66 (0.08), −0.63	59.60 (1.19), 0.00

Sunitinib-Treated Training set ($D^{suni}_{training}$)

The same clustering approach applied to the $D^{suni}_{training}$ dataset identified three major clusters (Figure 4.3b): Clusters A_t, B_t, and C_t, where the subscript t stands for the treatment group. Cluster B_t splitted into two subgroups: $B1_t$ and $B2_t$ (Table 4.3).

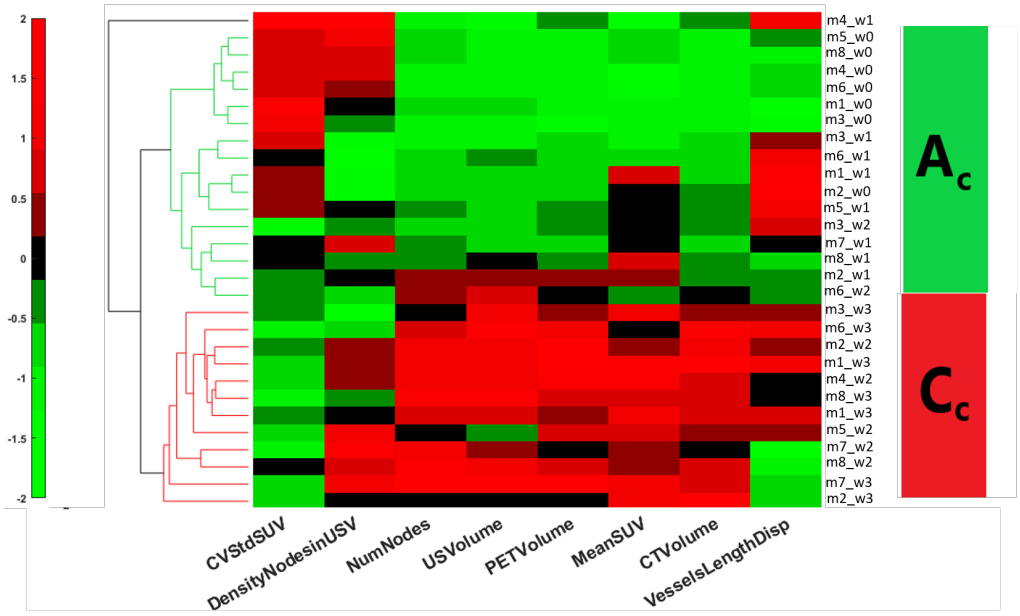

((a)) Control

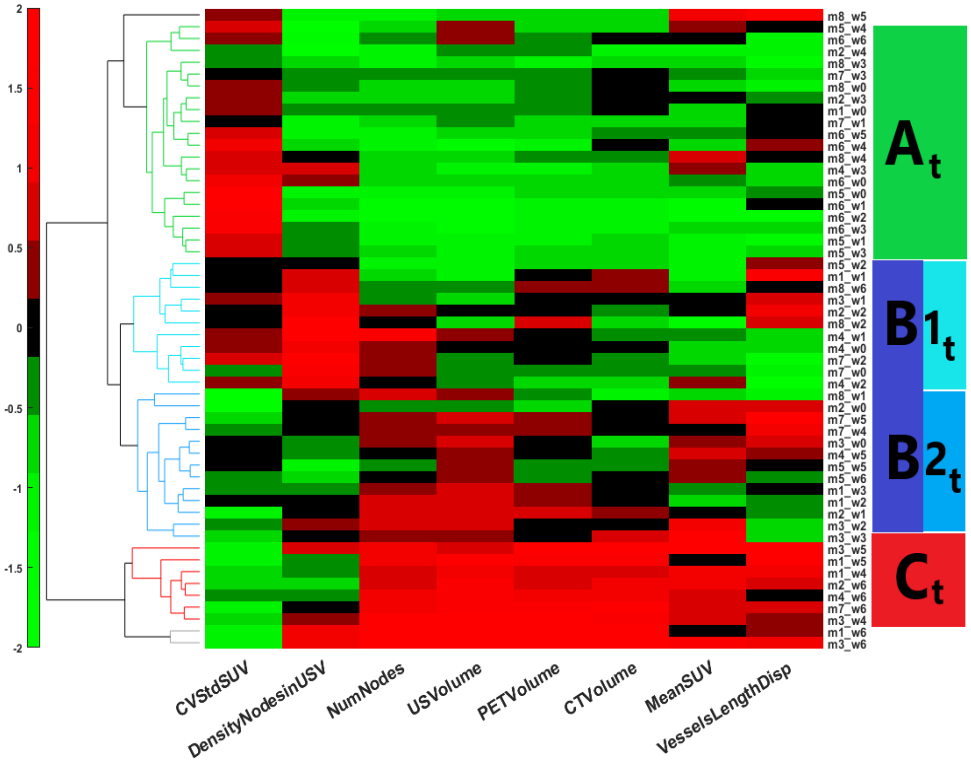

((b)) Sunitinib

Figure 4.3: Heatmap and hierarchical clustering performed (**a**) on the $D^{con}_{training}$ dataset and (**b**) on the $D^{suni}_{training}$ dataset. Two clusters (A_c, C_c) were identified in (**a**) and 4 clusters (A_t, $B1_t$, $B2_t$, and C_t) were identified in (**b**).

- Cluster A_t was characterized by low volumes of CT, PET, and UUDI, a high coefficient of variation of the standard deviation of SUV , and low vessel length dispersion, number of nodes, and density of nodes. This corresponds to a small-sized tumor with low vascularization and heterogeneous distribution of FDG uptake value, features that are similar to those of cluster A_c of the control group.

- Cluster C_t was characterized by high volumes of CT, PET, and UUDI, low coefficient of variation of the standard deviation of SUV , high vessel length dispersion, and very high number of nodes. This cluster corresponds to a tumor with a large volume, high metabolism and vascularization, and low heterogeneity in the distribution of FDG uptake, features that are similar to those of cluster C_c of the control group.

To compare the A and C clusters obtained with the SUNI and CON groups, respectively, a Kruskal–Wallis test [196] was performed between the A_t and A_c clusters, and also between the C_t and C_c clusters. The clusters were statistically similar (p-value < 0.05), indicating that clusters A_t and A_c on the one hand, and clusters C_t and C_c on the other hand, correspond to similar tumor states in the sunitinib-treated and sham-treated groups.

In the sunitinib-treated training set, the HCA algorithm identified two further clusters not present in the CON group:

- Cluster $B1_t$ was characterized by low to moderate volumes of CT, PET, and UUDI, low coefficient of variation of the standard deviation of the SUV, high vessel length dispersion, and a very high density of nodes. This corresponds to a small tumor with a significant but moderate level of vascularization, and medium-to-high heterogeneity in the distribution of FDG uptake.

- Cluster $B2_t$ was characterized by moderate volumes of CT and PET, high UUDI volume, lower coefficients of variation of the standard deviation of SUV, high vessel length dispersion, and low density of nodes. This corresponds to a moderate to high tumor volume and vascularization and low heterogeneity in the distribution of FDG uptake.

Table 4.3: Metabolic, vascular, and anatomical characteristics of the clusters from the $D^{suni}_{training}$ dataset. The mean values of each parameter of each cluster are represented. In black, the means; in parentheses, the standard means error; and in blue, the z-score means.

Features	**CVstd-SUV**	**Density Nodes inUSV (1/mm^3)**	**Num-Nodes**	**US Vol-ume (mm^3)**	**PET Vol-ume (mm^3)**	**Mean SUV**	**CT Vol-ume (mm^3)**	**Vessels Length Disp (mm^2)**
Cluster A_t	52.01 (1.17), 0.81	28.99 (1.05), −0.64	243.15 (18.20), −0.90	5.58 (0.78), −0.81	99.61 (9.73), −0.73	1.73 (0.11), −0.56	66.90 (8.22), −0.60	55.68 (0.77), −0.52
Cluster $B1_t$	47.68 (0.65), 0.12	44.08 (1.84), 1.46	527.4 (50.99), 0.16	11.84 (0.80), −0.34	195.85 (18.44), −0.09	1.79 (0.15), −0.49	100.08 (15.36), −0.29	57.33 (2.22), −0.24
Cluster $B2_t$	43.93 (0.72), −0.64	32.06 (1.02), −0.07	583.64 (29.78), 0.61	18.11 (0.46), 0.78	228,16 (15.76), 0.50	2.56 (0.22), −0.35	123.51 (11.52), 0.06	59.46 (1.40), −0.25
Cluster C_t	41.13 (0.58), −0.92	31.78 (1.29), −0.25	790.67 (39.46), 1.13	24.89 (0.73), 1.52	386.45 (29.66), 1.17	2.67 (0.12), 0.60	261.73 (17.84), 1.23	63.93 (2.01), 0.89

4.2.3 Robustness of Clusterization

An additional validation step was performed in order to ascertain that cluster formation was reproducible and not a casuistic process. HCA clustering was repeated on subsets of random instances of the $D^{suni}_{training}$ group, formed by randomly removing one mouse at a time. The accuracy of each HCA was calculated by considering the clusters obtained for all mice as ground truth and comparing it with the clusters of the new subset using the following formula: $Accuracy = \frac{Number\ of correCTpredictions}{Totalnumberof Predictions}$. As shown in Table 4.4, the total accuracy for each of the performed HCAs was greater than 95 percent for the three major clusters (A_t, B_t, and C_t).

Table 4.4: Performance of each of the HCAs for subsets of the $D^{suni}_{training}$ dataset. Data subsets were obtained by removing all the time points of one mice at a time.

Mice Removed	**1**	**2**	**3**	**4**	**5**	**6**	**7**	**8**
Total Accuracy (%)	100	100	95	98	100	100	95	100

4.2.4 Performance of Supervised Machine Learning Models

All 10 of the ML classifiers explored demonstrated good predictive performance, as demonstrated by the evaluation indexes of performance presented in Figure 4.4a. GNB achieved the best predictive performance (AUC: 100, ACC: 98.7), whereas DT exhibited the weakest (AUC: 96, ACC:94.8). The remaining classifiers achieved the following predicted performance: Quadratic SVM (AUC: 100, ACC: 97.4), KNB (AUC:98, ACC: 94.8), Linear SVM (AUC: 100, ACC: 97.4), KNN (AUC: 97, ACC: 98.7), RF (AUC: 100, ACC: 94.8), Narrow NN (AUC:100, ACC: 96.1), Bilayered NN (AUC:98, ACC: 94.8) and Weighted NN (AUC:100, ACC: 97.4).

Applying the best classifier to the three records that had not been classified using HCA, i.e., mouse1-week6, mouse3-week6, and mouse8-week5, allowed to classify these records into clusters C_t, C_t, and A_t, respectively (Table 4.5). This classification remained consistent with the previous stages of the sunitinib training set $D^{suni}_{training}$. The best-trained model applied to the $D^{suni}_{validat}$ dataset assigned a state for each record and mouse (Table 4.6) that was consistent with the states of the $D^{suni}_{training}$ dataset.

Table 4.5: Evolutionary path of sunitinib-treated mice of the training set. Items marked as * indicate missing classification due to the absence of corresponding PETRUS data. Clusters that were assigned by the RF model are underlined.

Mouse Number	**Baseline**	**Week 1**	**Week 2**	**Week 3**	**Week 4**	**Week 5**	**Week 6**
mouse 1	A_t	$B1_t$	$B2_t$	$B2_t$	C_t	C_t	C_t
mouse 2	$B2_t$	$B2_t$	$B1_t$	A_t	A_t	*	C_t
mouse 3	$B2_t$	$B1_t$	$B2_t$	$B2_t$	C_t	C_t	C_t
mouse 4	$B1_t$	$B1_t$	$B1_t$	A_t	*	$B2_t$	C_t
mouse 5	A_t	A_t	A_t	A_t	A_t	$B2_t$	$B2_t$
mouse 6	A_t	A_t	A_t	A_t	A_t	A_t	A_t
mouse 7	$B1_t$	A_t	$B1_t$	A_t	$B2_t$	$B2_t$	C_t
mouse 8	A_t	$B2_t$	$B1_t$	A_t	A_t	C_t	$B1_t$

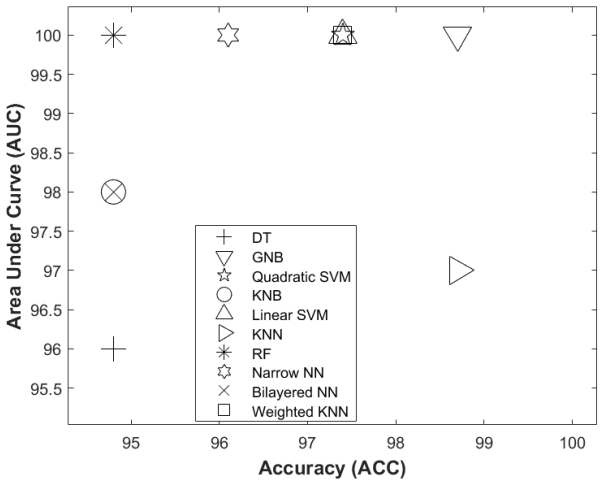

((a)) Classifiers Performance

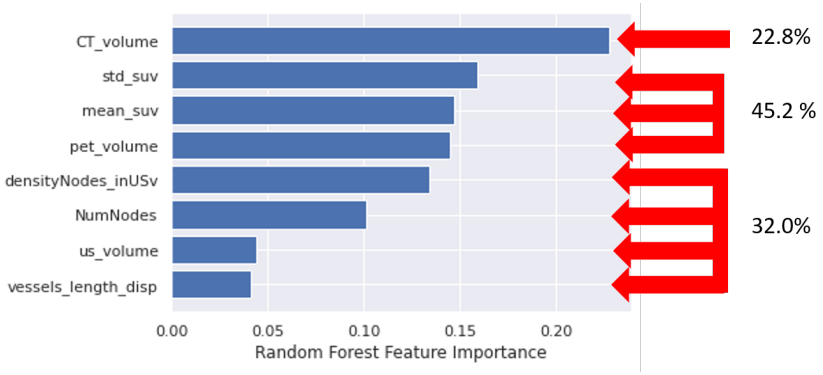

((b)) Feature Importance

Figure 4.4: Performance of the supervised machine learning models (**a**) Scatter diagram of machine learning classifiers prediction performance. The horizontal axis represents accuracy (ACC), the vertical axis represents the area under the curve (AUC); DT, decision tree; GNB; Quadratic SVM, support vector machine (Quadratic); KNB, kernel naive Bayes; Linear SVM, linear support vector machine; KNN, k-nearest neighbors; RF, random forest; NNN, narrow neural network; Bilayered NN, bilayered neural network; Weighted KNN, weighted k-nearest neighbors. (**b**) Contribution of anatomical, metabolic, and vascular features in the discrimination of the 4 clusters of tumor evolution stages identified with RF.

Table 4.6: Clusterization of the 11 sunitinib mice from the validation group. Items marked as - indicate that the RF approach was unable to assign the record to one any of the A_t, $B1_t$, $B2_t$, C_t clusters. Items marked as * indicate no PETRUS data available.

Mouse Number	**Baseline**	**Week 1**	**Week 3**	**Week 6**
mouse 9	A_t	$B1_t$	$B1_t$	*
mouse 10	A_t	A_t	$B1_t$	C_t
mouse 11	A_t	B_1	$B2_t$	*
mouse 12	A_t	$B1_t$	C_t	-
mouse 13	A_t	A_t	*	C_t
mouse 14	A_t	$B2_t$	*	*
mouse 15	$B1_t$	$B1_t$	*	*
mouse 16	$B1_t$	$B1_t$	*	*
mouse 17	A_t	A_t	$B1_t$	*
mouse 18	$B1_t$	A_t	*	*
mouse 19	A_t	*	*	*

Finally, using the RF classifier the relative importance of features used for training showed that all three types of tumor features, i.e., metabolic, vascular, and anatomical features, participated in the prediction of the four clusters (Figure 4.4b). This indicates that the information provided by each of the three imaging modalities contributed in a balanced way to define tumor stages for each imaging record.

Clusterization Reveals Tumor Progression

We then tested whether the different clusters would correspond to different time points during the tumor follow-up, i.e., whether, for any record, there was a correlation between assignment to one particular cluster and the time point at which imaging had been performed for that record. Regarding the CON group, all except two records (mouse 3/week 2 and mouse 6/week 2) of cluster A_c corresponded to the baseline or to the week-1 time point. Conversely, all cluster C_c records corresponded to week-2 or week-3 acquisitions. This confirms that cluster A_c represents an initial stage of the tumor, while cluster C_c represents an advanced tumor stage.

In contrast, the correspondence between the time-point of acquisition and assignment to the A_t or C_t cluster was much looser for the SUNI group than for the CON group. For example, mouse 6 remained in cluster A_t at all time points until week 6. Moreover, at baseline and week 1, a significant number of mice were not assigned to the A_t cluster but either to the $B1_t$ cluster (two mice at baseline and three at week 1) or to the $B2_t$ cluster (two at each time point). Conversely, upon reaching the last observation time point (week 6), five

mice from the SUNI group were in the C_t cluster, while one was classified in the $B1_t$ cluster, one in the $B2_t$ cluster, and one in the A_t cluster. Examples of trajectories for a mouse from the sham-treated group and for two mice from the sunitinib-treated group are shown in Figure 4.5a. We then investigated the influence of the vascular and metabolic features on the clustering results. Removing PET and UUDI features from the SUNI datasets and basing clustering only on the CT volume led to the co-clustering of [A_t;$B1_t$] and [$B1_t$;$B2_t$] (see boxplot in Figure 4.6a). This indicates that RECIST-like criteria using only CT did not identify intermediate clusters. When the same algorithm HCA was applied to the SUNI dataset from which the vascular features obtained by ultrasound imaging had been removed, i.e., using only the PET metabolic features and the CT volume, only two significantly different clusters were obtained using gap statistics: clusters $A_{PET/CT}$ and $B_{PET/CT}$. This indicates that PERCIST-like criteria, using PET-CT only, did not identify intermediate clusters (Figure 4.6b). Therefore, the intermediate B stage (B_t) and its two sub-clusters $B1_t$ and $B2_t$, essentially refle CT changes concerning the vascular features of tumors under sunitinib treatment.

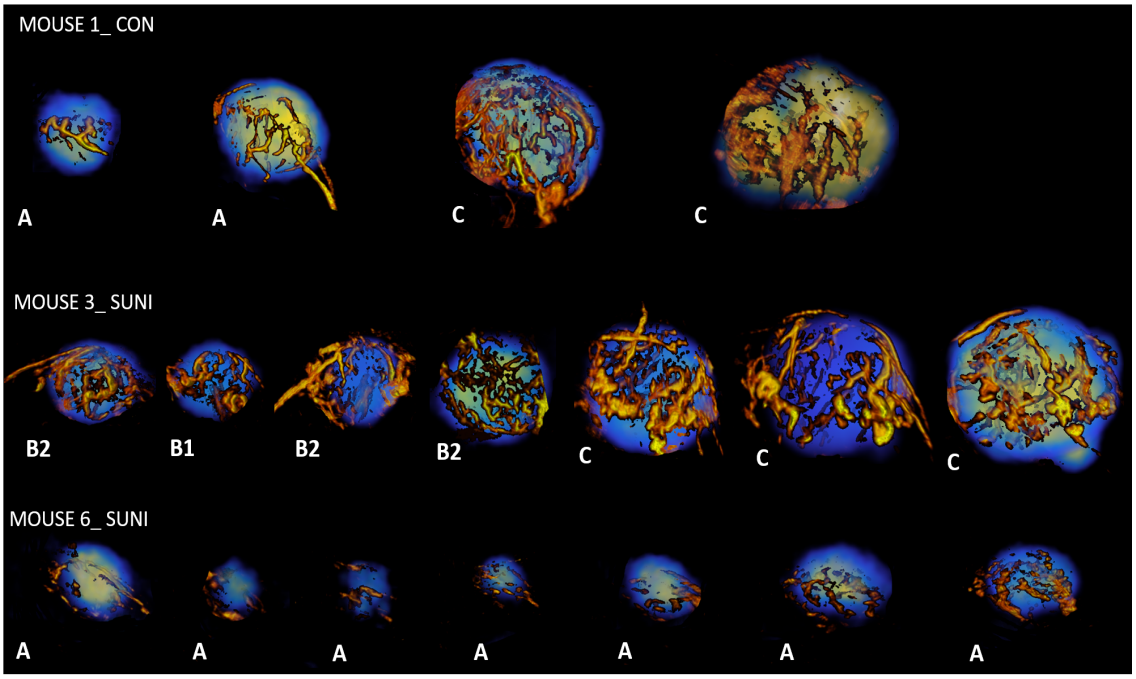

((a)) Visualization of Trajectories

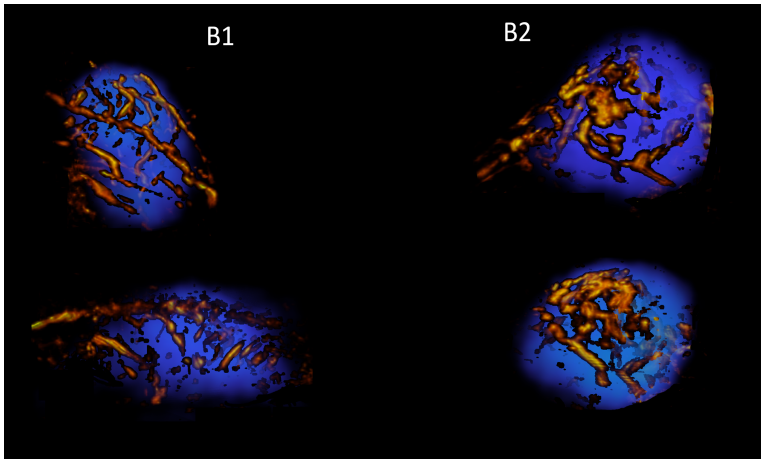

((b)) Visualization of B1 vs B2 vessels

Figure 4.5: Maximum intensity projection renderings of PGL tumors, (**a**) mouse 1 from the CON group, mouse 3 and mouse 6 from the SUNI group. Tumors in the CON group are shown at baseline and from week 1 to week 3, while tumors from the SUNI group are shown at baseline and at week 1 to week 6. (**b**) Comparison of PGL tumors at the $B1_t$ and $B2_t$ stages.

4.2.5 Clusters Depict Responses to Sunitinib Treatment

To further understand how clusters reflect the response to sunitinib treatment, the evolutionary trajectories (passage from one cluster to another over successive time points) were

studied individually for each mouse of the SUNI group (Table 4.5). The progression from cluster A_t to C_t of sunitinib-treated mice was not direct as the A_c to C_c in the sham-treated animals but passed through intermediate B_t clusters. This was confirmed by a correlation analysis performed on clusters A_t, B_t and C_t considered stages 1, 2 and 3, resulting in R^2 = 0.84. Calculation of the cluster transition matrix confirmed the relationship between the clusters and the chronology of tumor evolution. Assuming a progression represented by states A_t, B_t, and finally C_t, we obtained 29/46 (65.9%) stable phenotypes, i.e., remaining in the same state; 10/46 (22.7%) one progression, i.e., advancing further to the next state; and 5 (11.3%) regressions from B_t to A_t (Appendix Table **??**). Pooling the validation population and the training population showed an asymmetry between "progression" (n = 15) and "regression" (n = 6). Finally, Cluster C_t was an irreversible transition deriving essentially from the $B2_t$ state that appeared as a mandatory intermediate stage to reach state C_t, and the transition from B_t to A_t occurred only by the intermediary stage $B1_t$, and not by $B2_t$. States A_t, $B1_t$, $B2_t$, and C_t are thus ordered in time, suggesting that they are in fact tumor stages and that there is a progressive evolution of tumor stages from states A_t to C_t through B_t, and irreversibly between C_t and the other states.

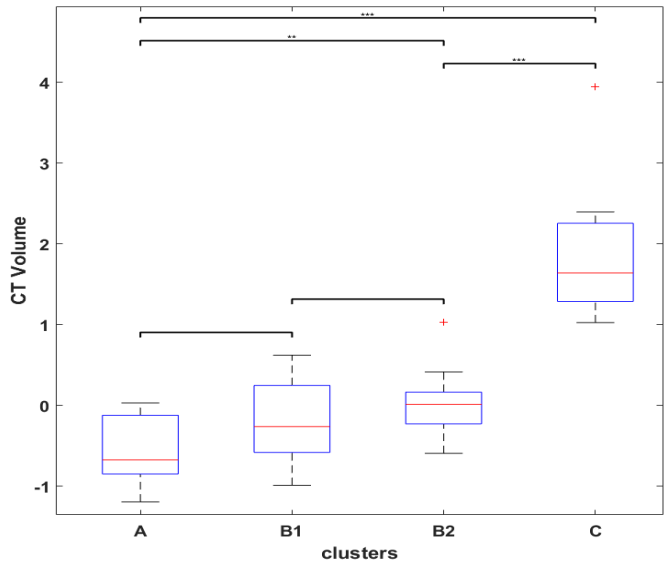

((a)) Visualization of Trajectories

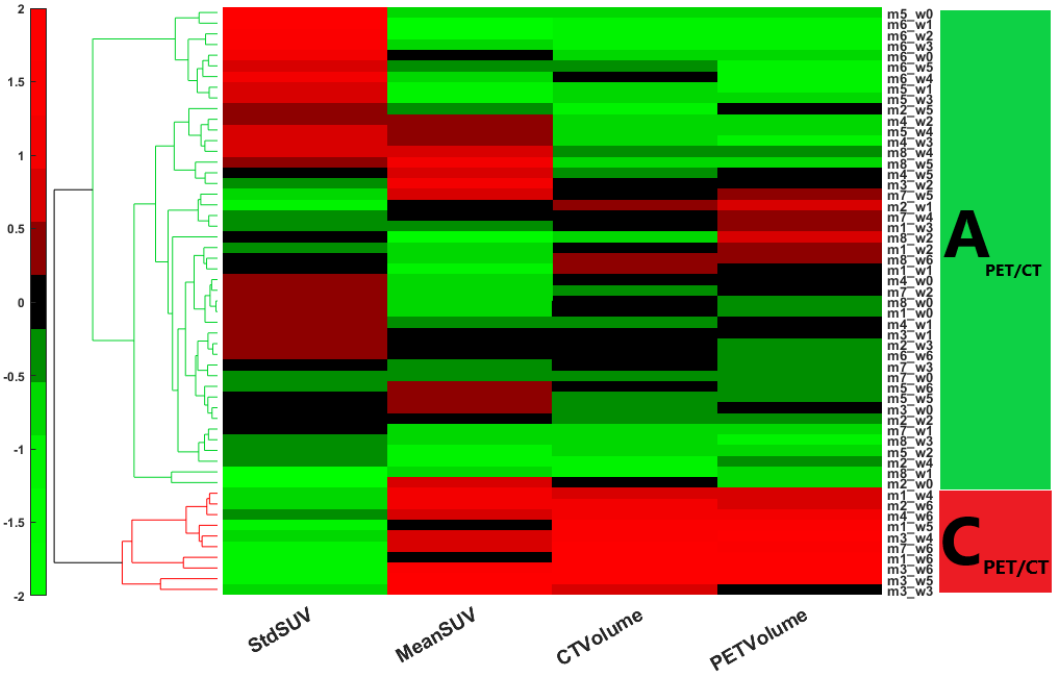

((b)) Visualization of B1 vs B2 vessels

Figure 4.6: Contribution of the vascular features for cluster discrimination in the SUNI group (**a**) CTVolume shows no significant difference between A_t-$B1_t$ and $B1_t$-$B2_t$ (p_value > 0.05), indicating that RECIST criteria alone did not identify the intermediate $B1$ and $B2$ clusters. (**b**) Similarly, hierarchical clustering performed on the $D^{suni}_{training}$ dataset considering only the features derived from PET and CT scans did not identify the intermediate stages $B1_t$ and $B2_t$ either.

In summary, multi-feature ML analysis of the sunitinib-treated animals showed that in-

dividual trajectories, defined by the passage from one cluster to another, followed a discrete number of rules:

- Irrespective of whether mice received sunitinib or vehicle, no mouse reversed from the advanced tumor stage (cluster C) to a less advanced stage.
- In the sunitinib group, mice moved from the early tumor stage (cluster A_t) to either one of the two intermediate stages (clusters $B1_t$ or $B2_t$) but not directly to the advanced stage (cluster C_t).
- In the sunitinib group, mice moved from cluster $B1_t$ to $B2_t$ and back, and from cluster $B1_t$ back to cluster A_t, but no passage from cluster $B2_t$ to cluster A_t was observed.
- In the sunitinib group, all mice reaching the advanced (cluster C_t) stage originated from cluster $B2_t$.

The robust correlations between clusters and treatment duration, and the transition matrix between clusters confirm that the A, B, and C clusters correspond to tumor stages. Interestingly, transitions between sub-clusters $B1_t$ and $B2_t$ were less correlated with time than transitions between A_t and $B1_t$ or $B2_t$, and between $B2_t$ and C_t. This suggests that the "reverse" transitions, i.e., $B2_t$ to $B1_t$ and $B1_t$ to A_t, could reflect the phenotype changes associated with a positive response to sunitinib. Figure 4.7 summarizes the trajectories between tumor stages in sunitinib-treated mice. There was first an increase in the level of tumor vascularization (A_t to $B1_t$ transformation), followed by a decrease in the heterogeneity of FDG distribution in the tumor ($B1_t$ to $B2_t$).

4.3 Discussion

Previous studies used ML to study the correspondence between gene expression and tumor progression [197, 198], including PGL [199]. To the best of our knowledge, this is the first application of ML based on HCA and supervised ML algorithms to noninvasive multimodal imaging of PGL. PGL lesions may concern the whole sympathetic and parasympathetic chains from the base of the skull to the pelvis. Germline mutations in one of the SDHx genes are responsible for approximately 20% of cases of PGL and also in some other tumors [24, 200]. PGL patients carrying SDHx mutations show a higher rate of metastatic disease and a lower rate of survival than non-SDHx PGL patients. Surgery is not without risk and may be impractical for numerous or misplaced lesions. Clinical trials with sunitinib have reported modest results in SDHB mutation carriers [69, 25]. There is an international consensus on the use of repeated non-invasive imaging for the screening, management and follow-up of PGL patients [201], as well as for asymptomatic SDHx mutation carriers [202]. Our results show that unsupervised ML of serial noninvasive and multimodal imaging data can define the phenotypic stages of mouse Sdhb-/- PGL tumors under anti-angiogenic treatment. The main finding is that, although the records fed to the ML algorithm had not been time stamped for the duration of treatment, unsupervised ML applied to multimodal multiparametric imaging features yielded clusters relevant to disease progression and to the

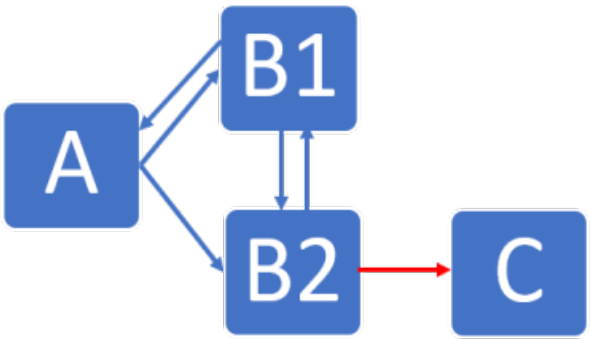

cluster	volume	vascularization	FDG heterogeneity
A	Lo	Lo	Hi
B1	Lo	Med	Hi
B2	Med	Med-Hi	Lo
C	Hi	Hi	Lo

Figure 4.7: Graphical and tabular representations of the trajectories highlighting the major characteristic features of mice under sunitinib treatment.

response to sunitinib. In the sham-treated group, all mice switched, generally in less than three weeks, from cluster A_c, an early stage with small and poorly developed tumors, low vascularization, and heterogeneous FDG uptake, to cluster C_c, an advanced stage with large tumors, large vessels, high and relatively homogeneous FDG uptake, corresponding to an end-stage cancer disease. In the sunitinib-treated group, a given tumor from a given mouse could, over time, move from one cluster to another, suggesting that the changes from one cluster to another depicted trajectories of tumor evolution related to the response or the escape from treatment. Some sunitinib-treated tumors showed a progression similar to sham-treated tumors, which infers that sunitinib-treated mice entering the advanced-stage C_t cluster have escaped sunitinib treatment.

Two other clusters, $B1_t$, and $B2_t$, representing intermediate tumor stages, were observed only in the sunitinib-treated group, supporting the view that their phenotypes represent the effects of sunitinib on PGL tumors. The first one, $B1_t$, encompassed small-sized tumors with a significant but moderate level of vascularization and heterogeneity in the distribution of glucose uptake. The second cluster, $B2_t$, encompassed tumors of moderate volume and vascularization, and low heterogeneity in the distribution of glucose uptake. ML did not identify these two intermediate stages when the vascular features derived from ultrafast ultrasound were removed from the analysis. Therefore, the $B1_t$ and $B2_t$ intermediate stages identified the effect of sunitinib on tumor vascularization, likely by inhibition of vascular endothelial growth factors receptors (VEGFRs), the major pharmacological target of the drug [203]. Previous studies have documented the relationship between tumor vascular types and the malignancy of PGL or pheochromocytoma, which is the adrenal form of paraganglioma. In a pioneering study, al.[19] divided pheochromocytomas into two groups according to their vascular architecture. Tumors with short, straight vascular segments distributed regularly over large areas of tumoral tissue had a vascular density equivalent to that observed in the normal adrenal medulla, while tumors with longer vascular segments of irregular length and a lower density of vessels corresponded to the malignant form. These regular and irregular patterns observed using in vitro stained sections of tumor tissue samples are remarkably similar to the states that we observed here in vivo, A and C [19]. A few years later, a study attempted to use "Favier's criteria" of the vascular patterns on histological sections of pheochromocytomas and PGL for the prediction of clinical behavior [204]. Again, malignancy was associated with an irregular vascular pattern; however, in spite of the correct agreement between observers, sensitivity and specificity were relatively modest and the authors concluded that vascular patterns, although useful, were not sufficient as "stand-alone [...] prognostic tool for the distinction between benign and malignant PCC...". Interestingly, we observed a difference in vascular morphology reminiscent of regular/irregular patterns under sunitinib treatment, tumor vessels being larger in diameter at stage $B2_t$ than at stage $B1_t$ (see Figure 4.5b). Therefore, while the analysis of vascularization may by itself not be sufficient, and notwithstanding the fact that the morphology of vessels in fixed tissue may not reflect their in vivo morphology, there is good agreement with changes in vessel morphology and the response to sunitinib, suggesting that the in vivo exploration of vascular morphology may be useful for the management of PGL. In addition, the link between FDG heterogeneity and microvascular density was theorized using a spatiotemporal computational model [205]. Our present results are in agreement with the authors' conclusion that "as microvascular densities increase [...], the spatiotemporal distribution of total FDG uptake by tumor tissue changes towards a more homogenous dis-

tribution [205]". Therefore, combined imaging of vascularization and metabolism could be an advantage for the follow-up of PGL patients under treatment.

Interestingly, all of the three mice that pertained to a B cluster ($B1_t$ or $B2_t$) at baseline ended up in the C_t cluster at the end of the 6-week sunitinib treatment, while only one of the four mice pertaining to the A_t cluster at baseline ended up in the C_t cluster. Although further studies are necessary to determine whether the tumor's biology prior to the administration of sunitinib could predict future escape from treatment, this may indicate that tumors that have already developed a significant vessel network are less prone to respond to sunitinib therapy. Thus, even though the switch from $B1_t$ to $B2_t$ was reversible under sunitinib treatment ($B1_t$ to $B2_t$), increased vascularization and decreased metabolic heterogeneity defining the $B2_t$ stage were necessary features for passage to the C_t stage, in other words, for escape from sunitinib treatment. From a cancer biology point of view, this suggests that escape from sunitinib treatment involves both a metabolic and a vascular switch.

From a statistical point of view, the analysis of each record independently without time stamping allows to extraction of information regarding the rates of tumor evolution in a small group of eight mice. This would not have been possible with conventional methods based on time-stamped groups of individuals unless the number of individuals would have been drastically increased. Considering the necessity to reduce the use of animals in research, the unsupervised method for the analysis of multimodal imaging presented here is an attractive alternative for the preclinical exploration of treatments in cancer models.

Moreover, cluster extraction using multiple features could allow gaining a better understanding of the sequence of events underlying drug response. The fact that cancer is a multiform disease with multiple intermingled hallmarks has been extensively documented and reviewed in the classical paper by Hanahan and Weinberg [7]. Therefore, it is unlikely that assessing only one biomarker, even one that informs on the activity toward the pharmacological target, may be sufficient to assess treatment response, and, even less so, to identify complex escape mechanisms. All in all, our results support the recourse to multimodal imaging with the careful selection of relevant imaging biomarkers, ideally including one or several biomarker(s) of the hallmark targeted by the treatment. In this respect, other tumor variants could also benefit from similar approaches extracting biomarkers specific to the tumor type and/or treatment. Finally, it may also be interesting to apply a radiomics analysis in order to compile mathematically defined image features and determine whether they represent phenotypic states predictive of tumor stage predictive of treatment response.

The main limitation of our study is that it is based on preclinical data. Serial imaging sessions, even non-invasive, are difficult to envision in clinical settings. However, we show that comprehensive longitudinal explorations in a patient-relevant animal model can identify key imaging features leading to sunitinib resistance, and may inspire translational methods for tumor follow-up in patients. ML analysis of multimodal hybrid imaging could offer individual monitoring of the vascular and metabolic states of a tumor, thus providing valuable information for personalized treatment decisions. Our results need to be further validated on prospective cohorts and extended to the clinical situation.

4.4 Conclusions

The combination of hierarchical clustering and supervised machine learning algorithms provides remarkable insight into the progression of tumor development in a mouse model of paraganglioma. Through the incorporation of multi-modal information, including the vascular features of the tumor-targeted by sunitinib, our approach is successful in depicting trajectories of response to treatment. This approach could set a basis for personalized follow-up of tumors treated by targeted therapies.

Chapter 5

Intratumoral Heterogeneity by Molecular-Vascular Profiling for Predicting Drug Resistance

Continuing our exploration into the intricate dynamics of treatment response in paraganglioma, this chapter represents a significant evolution from our preceding work. In our prior investigations, we identified distinct stages of treatment response in a paraganglioma mice model treated with sunitinib. This initial groundwork provided a foundational understanding of the tumor's behavior when subjected to therapeutic interventions.

In this current phase, our focus shifts toward an innovative hypothesis: the potential existence of tumor subregion(s) that hold the key to predicting treatment response within the same model. The identified subregion(s) could offer crucial insights into the varying responses of the tumor to sunitinib treatment. This hypothesis has emerged from the comprehensive analysis of the stages we previously identified, prompting a deeper exploration into the microenvironment of the tumor. By hypothesizing the existence of tumor subregion(s), we aim to bridge the gap between the macro-level treatment response stages and the nuanced micro-level characteristics within the tumor.

In the current study, we employed a machine learning framework that serves as a powerful tool in unraveling the complexities of tumor heterogeneity. By harnessing machine learning algorithms, our objective is to pinpoint and map the unique characteristics inherent within the tumor subregions, potentially revealing their significance in predicting treatment response. The integration of machine learning not only broadens our analytical scope but also signifies a promising convergence of medical research with advanced computational methodologies.

Furthermore, this chapter represents an integration of collaborative efforts that have significantly influenced the trajectory of our study. The collaboration with Grupo de Física Nuclear at the Facultad de Ciencias Físicas in Spain has been instrumental. It's noteworthy to mention that the work in this chapter is under consideration for publication. We have submitted our findings to Medical Image Analysis, reflecting our commitment to sharing

our discoveries with the scientific community. This chapter, with its combination of previous findings marks as a pivotal stage in our exploration of paraganglioma treatment response.

5.0.1 Database Formation

Animal housing, tumor implantation, follow-up, imaging, and sunitinib administration were as described in [**Facchin**]. Animal experiments were approved by the French Ethical committee under reference No. 16-098. Briefly, 6-week-old adult female nude mice weighing 30g (Janvier Labs, France) underwent implantation in the dorsal fat pad of tumors derived from immortalized mouse chromaffin cells (imCC) carrying a homozygous knockout of the *Sdhb* gene ($Sdhb^{-/-}$). When tumors had grown to a volume of 300 mm^3, they received through oral gavage a daily dose of 50 mg/kg of sunitinib malate (Clinisciences, A10880-500) for six consecutive weeks. Imaging sessions were conducted before drug administration and then weekly until the sixth week for mice treated with sunitinib (8 mice). Two imaging sessions were discarded because of animal motion, and all in all 8 * 7 = 54 images constituted the input dataset, Fig. 5.1-A.

5.0.2 *In vivo* Imaging protocol

The hybrid *in vivo* imaging technology PETRUS (Positron Emission Tomography Registered Ultrafast Sonography) [**PETRUS**] allows for simultaneous acquisition of tissue metabolism using [^{18}F]Fluorodeoxyglucose (FDG) dynamic PET, Computed Tomography (CT) and Ultrafast Ultrasound Doppler Imaging (UUDI) [**PETRUS**]. PETRUS simultaneously reads the cellular metabolism activity alongside micro-vascular architecture within the tumor, ensuring unimpaired physiological conditions for both sets of spatially co-registered features [**Facchin**].

PET acquisition started 30 seconds before injection of 10 MBq of 18F-FDG in 0.2 mL saline into the mouse tail vein. List-mode PET data were collected during 60.5 min, binned using a 5-ns time window, a 400- to 600-keV energy window, and a 1:5 coincidence mode, i.e. each detector associated with the five opposite detectors. Data were reconstructed by the TeraTomo reconstruction engine (3D-OSEM based manufactured customized algorithm, Mediso medical imaging systems, Hungary). A 31-frame dynamic sequence was obtained with the following time sequence: exclusion of 20 s; 10 frames of 5 s, 5 frames of 10 s, 2 frames of 15 s, 3 frames of 60 s, 5 frames of 120 s, 3 frames of 5 min, 3 frames of 10 min.

The UUDI system (Aixplorer, Supersonic Imaging, France) employed in-house MATLAB (MathWorks in Natick, MA, USA) scripts for plane-wave beamforming and for the implementation of Ultrasensitive Doppler Imaging (UUDI) [**Demene**]. UUDI images were captured as 2D planes measuring 12.8 x 20 mm^2, with each plane spaced 0.1 mm apart. Each plane resulted from averaging 300 temporal frames acquired at a frame rate of 500 frames per second. These frames were composed of images from 11 tilted plane waves, evenly distributed between -10 and 10 degrees. The entire tumor volume image was reconstructed by stacking individual planes that were spatially and temporally filtered [**Demene**] to extract

the vascular information. The number of planes per volume ranged from 70 to 200.

5.0.3 Tumor segmentation using a two-level clustering method

Intra-tumor segmentation was performed in two successive steps illustrated in Fig. 5.1. First, we performed individual tumor segmentation, where voxels exhibiting similar metabolic activity profiles were grouped into super-voxels. This step provided insights into distinct metabolic sub-regions within each tumor. A second-level clustering was conducted to group the related super-voxels by using information about the vascular patterns and architecture based on UUDI.

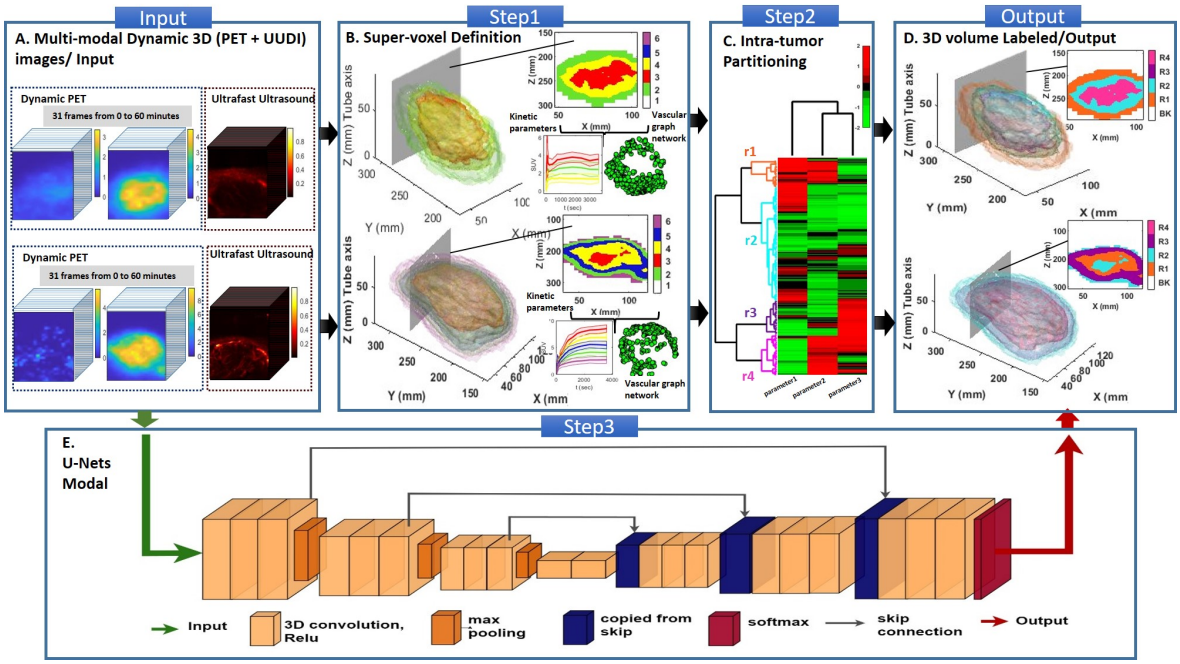

Figure 5.1: Schematic pipeline of the study. A: Dynamic (31-time consecutive time frames, see Materials and Methods section B) PET images from 8 mice acquired at seven separate time points, before treatment and weekly during treatment in addition to the 3D UUDI images, formed the input data for the study. B: K-means with calculated optimal k was applied to obtain distinct metabolic regions for each tumor independently. Each sub-region was outlined in supervoxels by averaging the PET values inside the sub-region and by extracting distinct metabolic and vascular features from the voxels corresponding to the sub-region. C: The resultant supervoxels were combined and used to perform intra-tumor partitioning. HCA was applied on the supervoxels to locate common sub-regions in the population. D. for each tumor a 3D volume with labeled sub-region(s) was produced to form the output of the study. E: The PET and the UUDI images were thereafter fed to the 3D-UNet model along with the labeled volume of step D to train a supervised model.

Individual-level tumor segmentation and definition of supervoxels

Voxels with common metabolic activities were clustered together applying K-means to the dynamic PET of each tumor [**kmeans**]. In this step, the gap evaluation criterion was used to calculate the optimal 'K' level for the K-means algorithm in each tumor [**gap_eval**]. Subsequently, for each 'K', a supervoxel on each PET frame was calculated by averaging the PET value per sub-region. The PET values were expressed using the standard uptake value (SUV) of FDG for each voxel, calculated as the ratio of the concentration of FDG in the supervoxel ($\frac{KBq}{cc}$) by the ratio of the injected dose (KBq) and the mouse body mass (g).

Vascular and metabolic parameters of the supervoxels were extracted from co-registered UUDI and dynamic PET data, respectively. Within each supervoxel, vascular structures were delineated and skeletonized employing an interactive ordered thinning-based skeletonization methodology, as in [**Babin**]. For each supervoxel, the following vascular parameters were computed as previously described [**Mansouri**]: density and number of nodes, mean, maximum and minimum vessel diameter, vessel length, vessel dispersion, and vessel tortuosity. In the same supervoxels, the following metabolic parameters were computed: carrier-mediated transport of FDG from the plasma to the tissue (K1) and tissue to plasma (k2), rate constant of phosphorylation of FDG by hexokinase (k3), using COMKAT software [**Muzic**]. The Pharmacokinetic Rate Constant Ki that measures the rate of FGD uptake in tissue was also calculated using Patlak analysis [**Patlak**]. A comprehensive database of metabolic and vascular parameters were subjected to the feature selection methodology outlined in [**Mansouri**]. This allowed us to identify and retain the informative (coefficient of variation $> 10\%$) and non-redundant (pearson correletion coefficient threshold ≥ 70 %) from the database, which were forwarded to the population level analysis.

Population-level tumor segmentation: Intra-tumor Partitioning

The selected features encompassing all supervoxels for each subject were subjected to Hierarchical Cluster Analysis (HCA) (Fig. 5.1-C), a clustering method that explores the organisation of samples into groups and between groups, representing a hierarchy [**HCA**]. The HCA results were presented as dendrograms to show the organization of the samples and their relationships in the form of a tree. Each row within the HCA matrix corresponded to an individual supervoxel, and each column corresponded to a metabolic or vascular feature. HCA merging of supervoxels with common metabolic and vascular characteristics then identified spatially congruent sub-regions across the entire tumor population. The Euclidean distance was used as the distance metric (MATLAB version 2022-b) and inner squared distance (minimum variance algorithm) was used as a metric for computing the distance between clusters. Then, Kruskal-Wallis [**Kruskal**] analysis was performed on the resulting tumor sub-regions to assess their statistical significance, with a threshold p-value ≤ 0.05. These regions defined the final tumor partitions.

5.0.4 U-Net Construction for automatic partitioning

Previous results using the same dataset of the sunitinib treated mice group[**Mansouri**] identified four distinct tumor development stages denoted as A, B (comprising sub-stages B1 and B2), and C, corresponding to the initial, intermediate, and advanced tumoral states, respectively. In order to automatically segment the region predicting treatment escape, we employed a "U-Net" machine learning approach [**U-Nets**] to perform segmentation on three-dimensional PET and UUDI input images. The U-Net model was trained to assign sub-region classifications to each voxel within the PET image in conjunction with HCA label.

The U-Net architecture contains 2 major parts: the encoder network (contracting path) and the decoder network (expansive path) connected together through a bridge. Both parts are composed by a sequence of blocks. The encoder network has a typical Convolutional Neural Network (CNN) architecture. Each encoder block consists of two 3x3 convolutions followed by a ReLU activation unit and a max-pooling layer. The ReLu activation function introduces non-linearity in the network and its output acts as a skip connection for the corresponding decoder block. The max-pooling linear is important to reduce the training cost by reducing the feature maps to half. The major role of the encoder part is to extract features and learn an abstract representation of the input image.

The encoder and decoder networks are connected through a bridge explaining the arc in the U letter. The bridge is made of two 3x3 convolutions, where each convolution is followed by a ReLU activation function.

The novelty of the U-Net approach lies in its expansive path where each block up-samples the feature map using 2×2 up-convolution. Each block is connected via skip connection with the corresponding block in the contracting part. These skip connections provide features from earlier layers that are sometimes lost due to the depth of the network. At the final stage, an additional 1×1 convolution is applied to reduce the feature map to the required number of channels and produce the segmented image.

We trained a 3D U-Net using 3D convolutions, 3D max pooling, and 3D up-convolutions. We incorporated the pixel classification layer with the Dice pixel classification layer, in order to optimize the segmentation of smaller tumor regions while mitigating the influence of larger background regions. Our training process employed input patches sized at $64 \times 64 \times 48$, with a total of 10 training epochs, a MiniBatchSize of 12, and an initial learning rate of 10e-3.

5.1 Results

5.1.1 Tumor Partitioning

The three following features: Ki, number of nodes, and density of nodes in cluster volume were , in terms of non-redundancy the most robust features of the metabolic and vascular

aspects of the tumor. The non-redundant parameters were selected using Pearson correlation test and the informative parameters were selected by calculating the coefficient of variation as described in [**Mansouri**]. Applied to the same three parameters across all supervoxels, HCA identified four distinct tumor sub-regions denoted r1, r2, r3, and r4 (Fig. 5.2). Statistical analysis using the Kruskal-Wallis test validated the presence of significant differences among the imaging features depicting the phenotype of the four sub-regions, with a p-value ≤ 0.05. Each region exhibits distinctive metabolic and vascular characteristics:

- region r1 has a high number and a low density of vessel nodes, and high Ki values. This reflects a region characterized by a large vascular network with multiple branches and a high metabolic activity.

- region r2 displays a low number and low density of vessel nodes, and Ki values fluctuate between high, moderate, and low. These characteristics are indicative of low vascularization in a variable metabolic environment.

- region r3 has a low number and a high density of vessel nodes, and a low metabolism. These features are the opposite of those of region r1 and indicate small tumor regions with reduced metabolism and vascularization.

- region r4 is characterized by a moderate to high density and a high number of vessel nodes, and a low metabolism. It combines a low glucose metabolism with a proliferative vascular network.

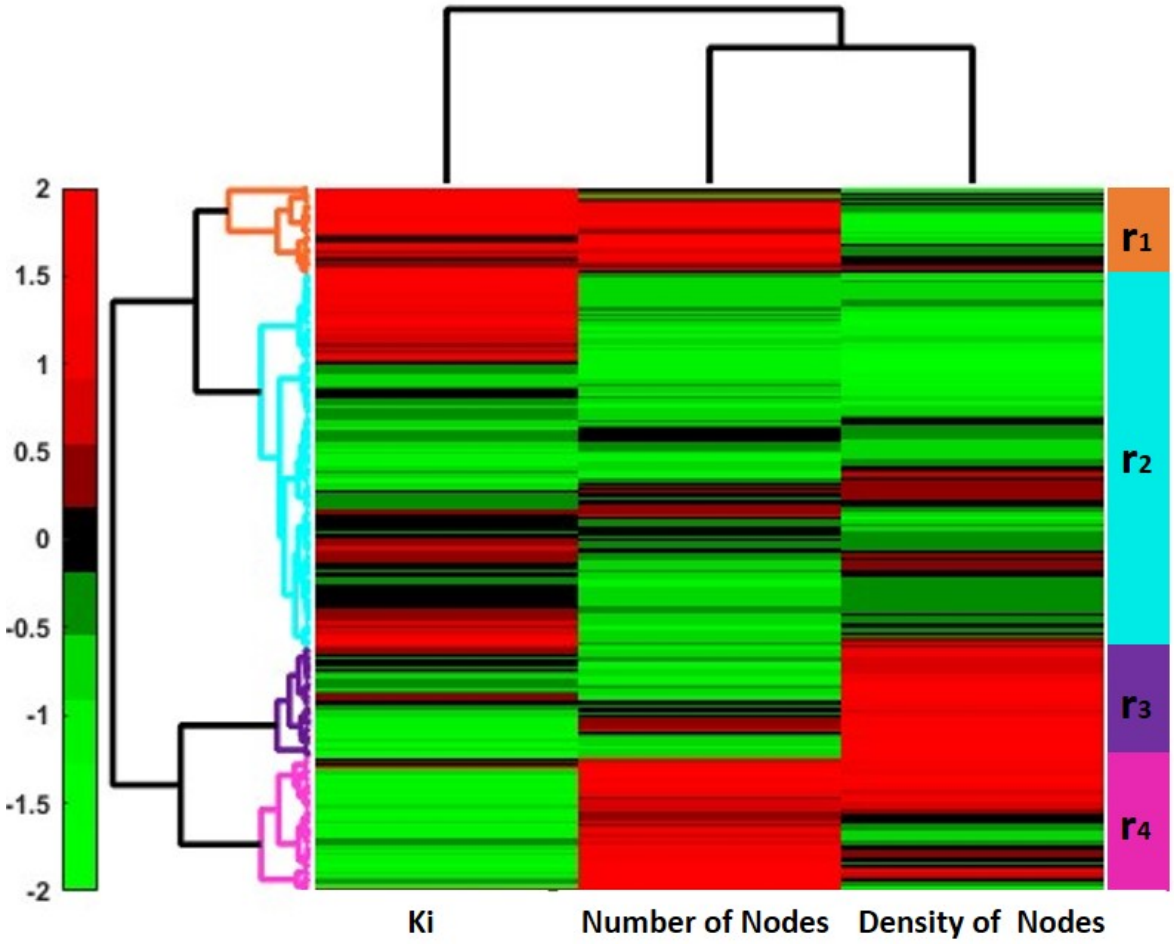

Figure 5.2: Hierarchical Clustering Analysis (HCA) output using the three most robust metabolic and vascular parameters (Ki, Number of Nodes, and Density of Nodes). The vertical dendrogram illustrates the distance between the parameters, while the horizontal dendrogram represents the distance between supervoxels. Resulting in the clustering of supervoxels into four sub-regions: r1, r2, r3, and r4.

Figure 5.3 presents a comparative analysis of two tumor volumes corresponding to mouse 3 (first column) and mouse 6 (second column) at week 5. The PET volume in the first case reveals elevated metabolic activity, contrasting with the second case displaying lower activity (first row) in both the full volume and the zoomed-in figure. Examination of the skeletonized vascular networks in the middle row indicates a greater number of nodes in mouse 3 compared to mouse 6. Upon zooming in, mouse 6 exhibits a more densely packed network than mouse 3. The combined analysis of metabolic and vascular characteristics, including metabolic activity (first row) and the number and density of nodes(second row), results in the classification of 94% of mouse 3 as region 1, while 79% of mouse 6 is classified as region 3. The zoomed-in figure in the third row reveals that the selected sub-volume predominantly represents r1 in mouse 3, whereas that of mouse 6 predominantly represents r3. The dimensions of the zoom-in region in each axis are accurately indicated in the top

right. This detailed visualization provides a clearer explanation of the selected parameters (K1, number, and density of vessel nodes) in two cases: mouse 3, considered responsive, and mouse 6, considered non-responsive, as discussed previously in [**Mansouri**].

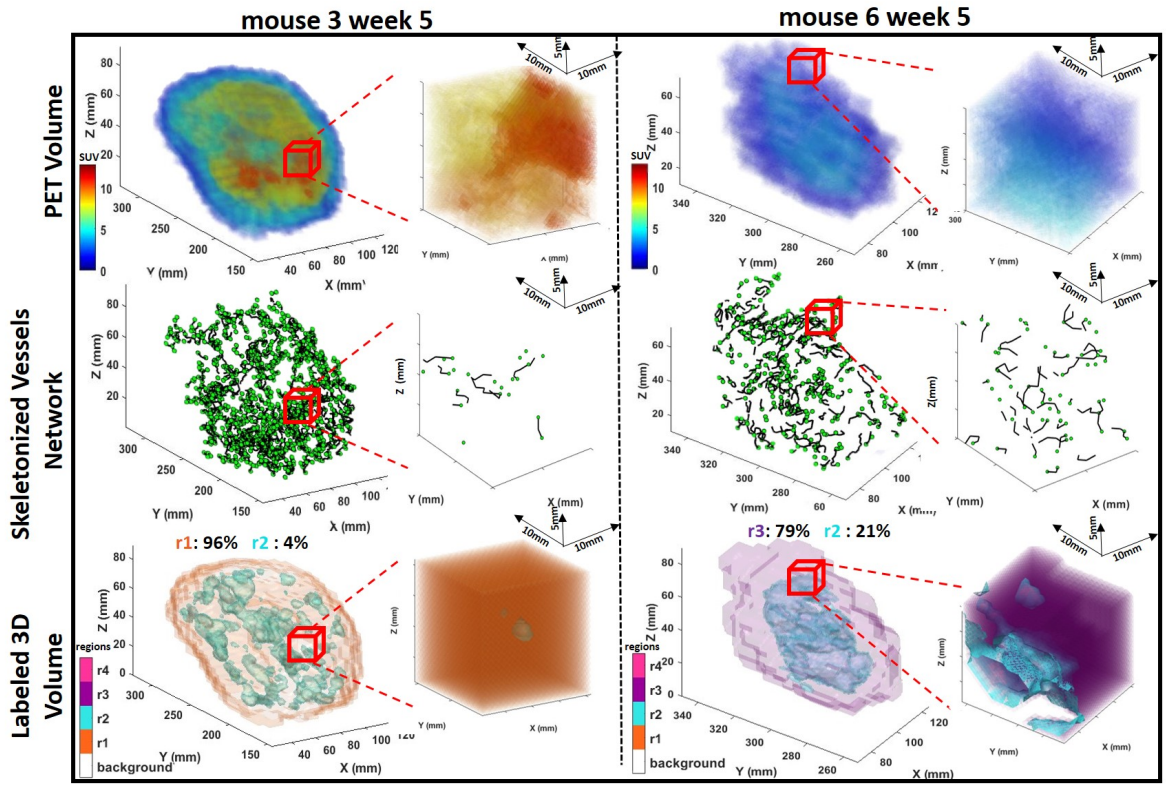

Figure 5.3: Examples of two tumor volumes correspond to mouse 3 (first column) and mouse 6 (second column) at week 5. The PET volume indicates high metabolic activity in the first case and low metabolic activity in the second (first row). In the middle row, the skeletonized vascular networks reveal a higher number of nodes in mouse 3 compared to mouse 6. Upon zooming in, mouse 6 displays a more densely packed network than mouse 3. The combined metabolic and vascular characteristics, including the metabolic activity and number and density of nodes, result in 94% of mouse 3 being classified as region 1, while 79% of mouse 6 is classified as region 3. The dimensions of the zoom-in region in each axis are indicated in the top right.

5.1.2 Identification of sub-region predictive to treatment response

Fig. 5.4 shows, for each mouse imaged weekly at baseline (pre-treatment) until week 6 of treatment, the ratio of each of the four sub-regions to the total tumor volume. Interestingly, region r1 was not present at any time point inside the tumor of Mouse 6 that responded very well to sunitinib [**Mansouri**]. Conversely, non-sunitinib-responding mice for which tumors had progressed at week 6 of treatment to the B2 or C stages showed a high level of r1 over the total tumor volume.

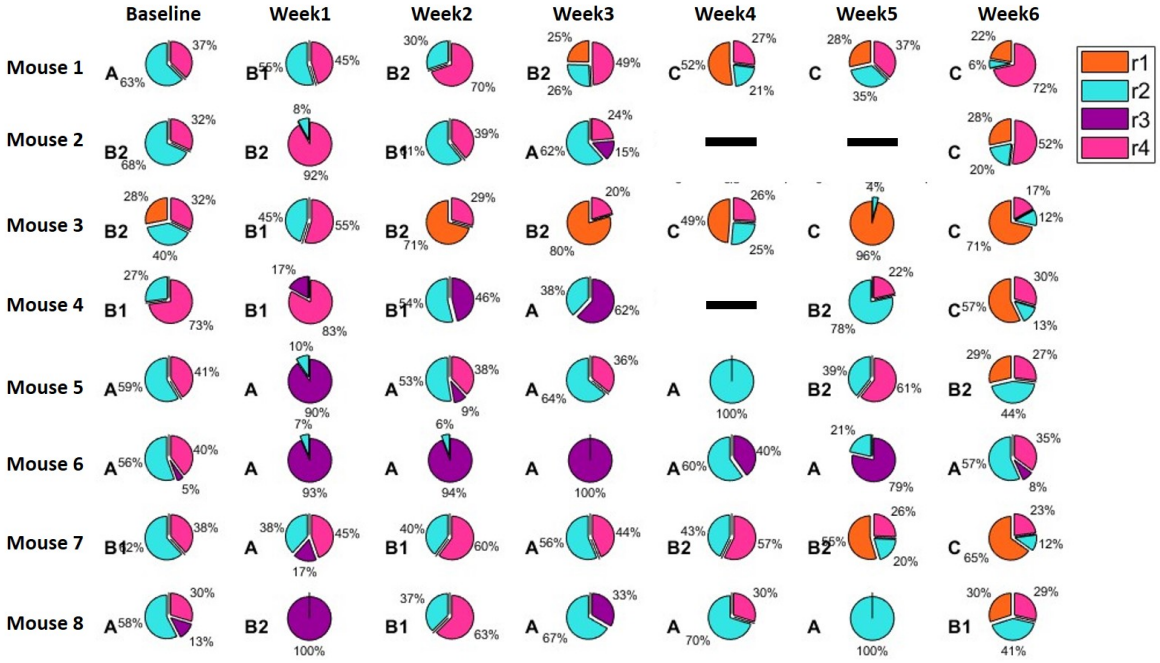

Figure 5.4: The respective proportions of regions r1, r2, r3, and r4 inside the tumor over the seven time points (spanning from pre-treatment to week 6 of treatment) acknowledge individual treatment response trajectories for each mouse. Response stages A, B1, B2 and C are those identified previously in [**Mansouri**]. Black dashes correspond to missing information due to mouse movement during the imaging session.

An overview of the different sub-regions' proportions for the different tumor stages is shown in Fig. 5.5. During the initial stage A, no r1 region was found in any of the mice, whereas the highest occurrence of r1 was observed in the advanced stage C (100%). The prevalence of r1 was low in stage B1 (10%) and moderate in stage B2 (46%). This observation suggests that the r1 region is a predictor of the response to sunitinib treatment. Conversely, region 3 showed its highest occurrence in stage A (67%) but declined in stages B1 and B2 (20% and 8%, respectively), and was absent in stage C. Regions r2 and r4 were consistently present across all stages. In summary, the absence of r1 corresponded to a less favorable response to treatment, while a high level of r3 indicated a positive response to sunitinib treatment.

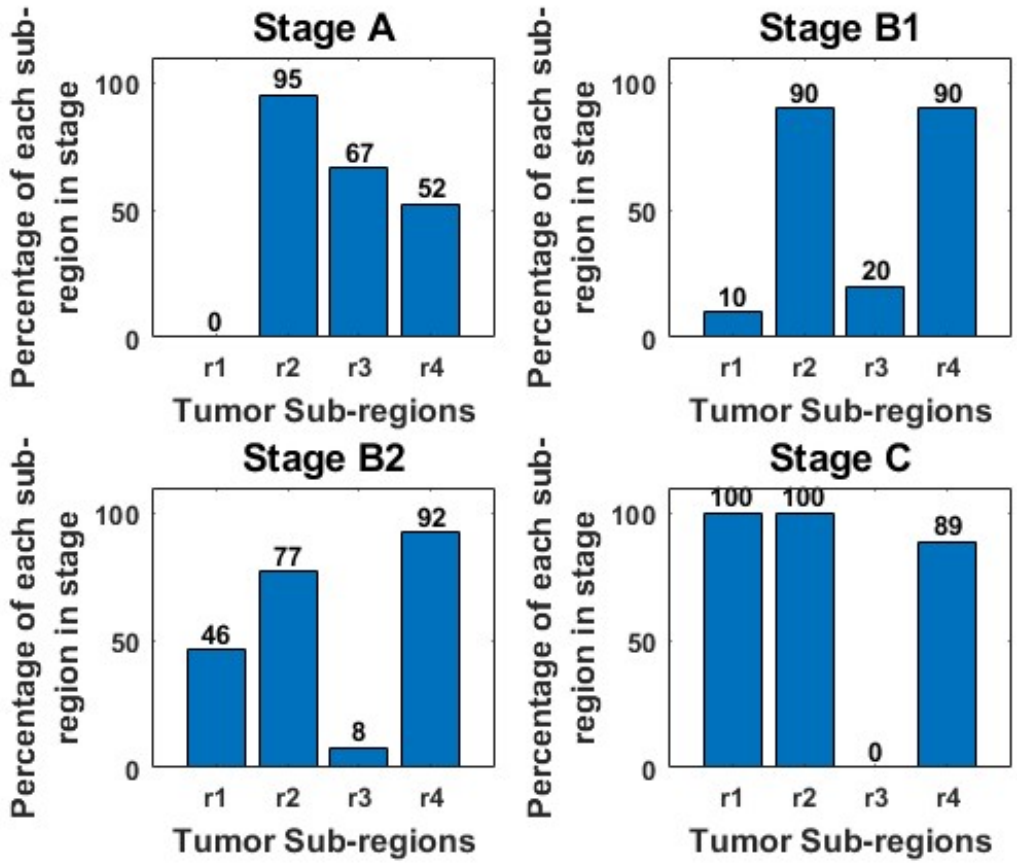

Figure 5.5: Frequency of appearance of each sub-region r1, r2, r3, r4, among the 4 tumor development stages A, B1, B2 and C [**Mansouri**]. Percentages represent the occurrence of a given sub-region in a given stage over the total number of cases containing the corresponding region

5.1.3 U-Nets

Following the assignment of K-means labels and the identification of r1 as the sub-region predicting treatment response, we proceeded to train a U-Net model specifically tailored to distinguish r1 from the other regions. Subsequently, the model underwent testing on random examples sourced from the entire database. The validation accuracy of the trained model reached 88.8%.

Fig. 5.6-A shows the Dice coefficient of the discrimination between r1 and the other regions. The testing accuracy for r1 achieved 86.7%, while the accuracy for the other sub-regions reached 80.4%. Fig. 5.6-B shows an example of a tumor section predicted by the U-Net model, compared to its corresponding ground truth segmented by K-means.

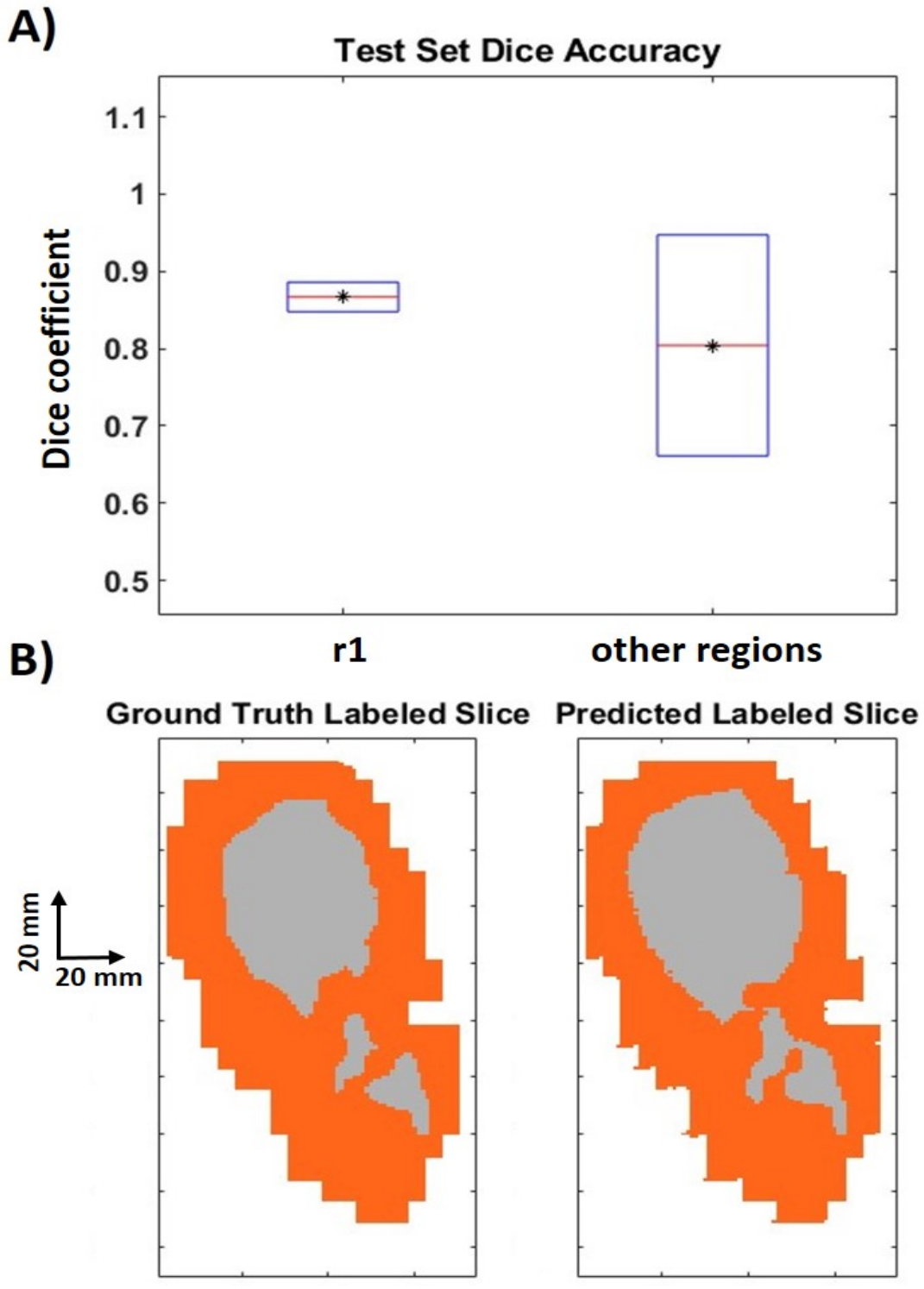

Figure 5.6: A) Dice accuracy coefficient in the testing data set for sub-region r1 was 86.7 % while for the other regions it was 80.4 %. B) Example of a predicted case and of the corresponding ground truth segmented by K-means. Sub-region r1 is shown in orange and the other sub-regions r2, r3 and r4 are shown in grey for.

5.2 Discussion

The present study aimed to explore a vascular-metabolic intricate landscape of intra-tumor heterogeneity in PPGL-SDHB$^{-/-}$ mouse tumors, with a specific focus on identifying regions associated with resistance to sunitinib treatment. Our work builds on previous research, which highlighted the critical role of metabolic, vascular, and morphological features in delineating the stages of the response of PPGL-SDHB$^{-/-}$ to sunitinib treatment. In particular, metabolic heterogeneity defined as the coefficient of variation of SUV, a feature linked to tumor heterogeneity, appeared as a robust biomarker for stage identification, in line with findings from our previous research [**Mansouri**]. The present study sought to investigate further the relevance of intra-tumor partitioning as an indicator of treatment resistance.

We developed a two-level unsupervised machine learning framework to segment tumors into distinct metabolic and vascular active sub-regions based on quantitative data measured using dynamic PET images of glucose metabolism and UUDI-derived vascular maps. It is worth noting that the segmentation process, based on the similarity between voxel-wise metabolic profiles, could have been performed by aggregating all dynamic PET data from all the tumors under investigation into a single-step K-means analysis. However, this approach would require considerable computational power to accommodate the spatial and temporal data from all voxels of all tumors, representing an unmanageable amount of data. The two-level strategy used here, in which the first step condensed individual voxels into super-voxels, greatly reduced the computational burden. Thus, it allowed the second level of clustering analysis to be run on a manageable amount of data, making the procedure computationally efficient. During the second level of clustering, we trained a supervised model to automatically identify the tumor partitions. By combining two different modalities - FDG-PET and UUDI - we integrated complementary information that revealed phenotypic changes induced by sunitinib treatment. Importantly, our approach included both metabolic and vascular features, the latter being the main target of the anti-tumor drug sunitinib. The utilization of U-Net, which is based on patch image extraction, allowed us to expand our database and train our model to autonomously identify tumor sub-regions. Our analysis yielded four distinct tumor sub-regions (r1, r2, r3, and r4), each characterized by different metabolic and vascular characteristics. Interestingly, region r1 was predominant in advanced stage C, intermediate in stage B2, low in stage B1, and absent in stage A. Thus, the proportion of region r1, characterized by high metabolic and vascular conditions, appears as a predictor of treatment escape. Conversely, r3, characterized by low metabolic and vascular activity, was prominent in stage A, less prevalent in stages B1 and B2, and absent in stage C, thus this sub-region was associated with a good response to treatment.

These results suggest that the r1 and/or r3 could thus serve as biomarkers of the response of PPGL to sunitinib treatment. Naturally, it remains to be demonstrated whether the method described here can be useful for the management of human PPGL patients. One advantage is that the two-step approach could be used to blindly investigate patient cohorts retrospectively, as shown by Katiyar et al [206].

Conclusion

In this study we showed that the spatial characterization of intra-tumoral heterogeneity in a mouse model of PPGL, using machine learning applied to non-invasive imaging, allows the identification of tumor sub-regions that predict the response to anti-angiogenic treatment.

Chapter 6

Radiomics Analysis of the Effect of Sunitinib Treatement on Sdhb$^{-/-}$ Experimental Paraganglioma

In this chapter, we embark on a journey into the intricacies of radiomics as it relates to Pheochromocytoma and Paraganglioma (PGL) tumors. Our objective unfolds in two distinct parts. Firstly, we aim to extract radiomic markers from the co-registered PET, CT, and UUDI images, of the entire tumor. The methodology outlined in Chapter 4 will serve as our guiding framework, and its application aims to ascertain the reproducibility of the distinct stages identified using the extracted radiomics features.

Expanding our focus beyond the overall tumor landscape, our second objective narrows in on specific regions labeled as r1 and r3. As revealed in Chapter 5, these regions exhibit a significant correlation with treatment response stages. By extracting radiomics features from the two delineated sub-regions separately, we aspire to unravel nuanced insights into the intricate relationship between radiomic signatures and the effectiveness of treatments for PGL tumors.

This dedicated chapter underscores our commitment to unraveling the radiomics complexities inherent in PGL tumor images. Through meticulous analysis and the application of our chosen methodology, we anticipate contributing valuable knowledge to the evolving landscape of radiomics characterization for PGL tumors. Such insights hold the potential to inform prognosis, guide treatment planning, and enhance personalized care for individuals affected by PGL tumors.

6.1 Materials & Methods

Based on the 2 objective of this chapter this section will be divided into 2 parts:

Part 1: Radiomics for Whole Tumor

The radiomics process explained in 1.5.2 is followed:

6.1.1 Quantittative Imaging

Co-registered PET/CT/UUDI images where acquired using PETRUS a prvious study by a former PhD student presented in chapter 3.

6.1.2 Region of Interest (ROI) Selection

As previously explained in 3 PET and UUDI volumes were cropped based on standardized criteria obtained from PET image segmentation, which was semi-automatically defined using iso-contours at a 30% threshold of the SUV peak in the last-time frame (50-60 minutes post-injection). The cropping of UUDI volumes utilized the mask generated from the PET segmentation. The CT volume was defined as the starting point, from which the tumors were delineated on the CT images and their boundaries were established with reference to the adjacent fat pad.

6.1.3 Feature Extraction

Radiomic features were derived using the SERA program, developed in MATLAB by Johns Hopkins University [207], which calculates radiomic characteristics in accordance with the Imaging Biomarker Standardization Initiative (IBSI) guidelines, ensuring their reproducibility. SERA is capable of extracting radiomics from CT, PET, MRI, and SPECT medical images. While UUDI images are not explicitly covered, they have been included as part of the CT images due to their similar characteristics. SERA provides access to a comprehensive set of 487 radiomic features, categorized into 29 morphology, 50 first-order, 150 second-order, and 258 higher-order features. Additionally, it offers 10 moment invariant characteristics, although these are not part of the IBSI guidelines and have not been utilized in this study.

SERA offers versatile options for configuring and modifying parameters prior to radiomic extraction. To assess the robustness of radiomic parameters in the face of variations in image settings, radiomic calculations were systematically repeated by altering the discretization of dynamic intensity range, voxel size, and interpolation method.

In terms of discretization, there is a choice between Fixed Bin Number (FBN), where a specific number of bins is chosen for calculation regardless of the range of intensity values in the image, and Fixed Bin Size (FBS), which employs a fixed bin size to group intensity values. With FBS, the bin width remains constant, and the number of bins may vary depending on the intensity range of the image.

For CT, PET, and UUDI images, FBN utilized 16, 32, and 64 bins, while FBS employed bin

sizes of 200, 400, and 600 for CT and UUDI, and 1, 2, and 3 for PET. The latter variation was due to PET being converted to SUV (Standardized Uptake Value), a crucial uptake index in 18F-FDG PET studies, defined as the ratio between the activity concentration in the ROI and the injected activity.

Voxel size was selected to match or be smaller than the spatial resolution of the imaging techniques. For CT and PET, 0.5 and 1 mm were chosen since their spatial resolution is 1.5 mm. Regarding UUDI, the choice considered the UUDI probe's 12 MHz frequency, which allows the observation of blood vessels with a minimum diameter of 0.1 mm. Additionally, the range of diameters observed in these tumors falls between 0.1-0.4 mm, thus warranting voxel sizes of 0.2 and 0.1 mm.

The three available interpolation methods, namely linear, cubic, and nearest neighbors, were employed for ROI resampling.

Through the radiomic calculations carried out with these diverse configurations, each image modality was subjected to 16 distinct combinations for each vowel size. These combinations encompassed both voxel sizes of 0.5 mm and 1 mm, spanning the PET and CT images. For UUDI, using voxel size 0.2 mm 16 combinations was also obtained. However, for voxel size 0.1 mm only 3 combinations where obtained since since the calculation time of each configuration was greater than two days, requiring the implementation of the calculation in mode, which is left for further work. Therefore, making in total 32 configuration for each of PET and CT images and 19 configuration for the UUDI images.

6.1.4 Feature Selection and Dimensionality Reduction

A total of 487 radiomic features were extracted using SERA for each imaging modality, resulting in a combined count of 1461 radiomics. However, due to the relatively low number of mice in the study, a notable imbalance exists between the number of parameters and the quantity of independent data. This discrepancy can potentially lead to the generation of erroneous predictions and findings.

In this context, it becomes imperative to mitigate the risk of overfitting by narrowing down the selection of radiomic features to those that exhibit robustness. Overfitting, if it occurs, can distort the analysis results as it endeavors to describe differences in images resulting from the inherent noise rather than accurately capturing variations due to tumor behavior or the specific data under examination.

Out of the 487 radiomics calculated for CT, PET, and UUDI, the focus is on identifying those that demonstrate both reproducibility, meaning they can be consistently replicated under different circumstances, and non-redundancy, as some image markers may exhibit correlations that necessitate choosing one among them to avoid redundant outcomes.

This selection process is further refined by determining the most robust configuration for each modality, a step that follows the evaluation of reproducibility. Additionally, radiomics characterized by an exceptionally low coefficient of variance, signifying their uniformity across all mice and tumor stages, are excluded, as they lack sensitivity to the specific information we aim to discern.

1. **Selecting most relevant configuration**
   A large number of combinations have been obtained by varying different parameters with *sera* and the most robust configuration has to be selected, using the function zscore from MATLAB.

2. **Testing features reproduciblity:**
   To identify reproducible radiomics features, we employ a method that filters out those which exhibit inconsistent behavior when varying image configuration options. In line with previous research [208], we utilize two correlation coefficients: the Intraclass Correlation coefficient (ICC) and the Concordance Correlation coefficient (CCC). The ICC is a statistical metric used to assess the reproducibility of radiomic features across different segmentations. It provides a value between 0 and 1, where 0 signifies no reproducibility, and 1 denotes perfect reproducibility. Radiomic features are categorized based on ICC values into three groups: highly reproducible (ICC $\geq$ 0.8), moderately reproducible (0.5 $\leq$ ICC $<$ 0.8), and poorly reproducible (ICC $<$ 0.5). On the other hand, CCC measures the agreement between two variables. Similar to ICC, CCC also ranges from 0 to 1, with values of CCC $\geq$ 0.9 indicating high reproducibility, and values below 0.9 indicating lower reproducibility. A radiomic feature will be considered reproducible if it demonstrates high reproducibility with respect to CCC and high or moderate reproducibility with respect to ICC simultaneously.

3. **Testing features redundancy**
   The elimination of redundant radiomic features offers several advantages, including enhanced precision in model results, reduced storage requirements, improved result visualization and comprehension, and shorter training times for automated models. To achieve this, a correlation matrix based on Spearman's correlation coefficient is employed, assessing the relationships between all variable pairs within the database. The Spearman correlation coefficient (often represented as ρ) is a statistical metric used to asses the strength of association between two sets of data. Its value falls within the range of -1 to +1, signifying the degree of correlation between variables: a value of r = +1 or -1 indicates a perfect positive or negative correlation, respectively, while r = 0 signifies no correlation between the variables. In this study, we employ a user-defined threshold of 0.9, categorizing radiomic features with $|r| \geq 0.9$ as highly correlated, thus offering redundant information.

   Furthermore, the p-value is evaluated as a measure of correlation between random variables. The p-value varies between 0 (0%) and 1 (100% probability). When ρ is close to 1, the correlation likely occurred by chance, whereas when p is close to 0, the correlation between radiomics is unlikely to be coincidental, indicating a genuine correlation. A p-value of $\leq$ 0.05 suggests a true correlation between the variables. Initially, redundancy between radiomics within each imaging modality is assessed individually, followed by an exploration of correlations between radiomics from different imaging techniques.

4. **Testing features informativity:**
   In a further effort to decrease the quantity of radiomic features, we excluded those exhibiting minimal variance. Specifically, we remove radiomic features that possess a coefficient of variation below 0.3.

5. **Elimination of atypical cases (Outliers)**
   The outliers, which refer to the exceptional cases significantly deviating from the norm were removed, particularly in relation to the frequency of imaging sessions conducted with PETRUS per week. In this context, we exclude weeks rather than radiomic features. To achieve this, we employ the `rmoutliers` function in MATLAB, utilizing the `mean` method, which effectively eliminates outlier cases from the database that deviate more than three standard deviations from the mean.

6.1.5 Statistical Analysis and Modeling

The same protocol followed in 4 was followed. In summary, Hierarchical clustering (HCA), was used to discover hidden patterns and relationships within the multi-modal radiomics data. Without the need for predefined labels or time point information, HCA groups radiomic features into clusters having commmon characteristics. This method effectively identifies distinct tumor stages during precision treatment based on the patterns present in the data. By grouping the obtained clusters per mouse and per week trajectories of tumor responses to sunitinb treatment were revealed.

6.1.6 Model Development

As described in 4 Random forest model was employed to build predictive models that assisted in understanding and predicting responses to precision treatment. In this approach, the models were trained using labeled data, which includes information about known tumor responses to specific treatments. The supervised models use this labeled data to learn patterns and relationships between radiomic parameters and treatment stages. Once trained, these models can predict how new cases will respond to precision treatment based on the radiomic features. This approach is valuable for tailoring treatment strategies to individual patients, as it can provide insights into the most effective treatment options based on the specific characteristics of the tumor.

6.1.7 Clinical Applications

In our study, this innovative approach was rigorously tested on a mouse model of SDHB paraganglioma, demonstrating its effectiveness in deciphering tumor response trajectories through multi-modal imaging and machine learning techniques. While the results are promising and hold significant potential for precision treatment in a research context, it is

crucial to note that the application of this approach in clinical settings has been limited. The primary reason for this limitation is the absence of comprehensive data from paraganglioma (PGL) patients, which is essential for validating and translating the findings to human cases. Due to this data gap, the clinical application of our approach remains a future objective, emphasizing the need for further research and data collection in the context of PGL patients to realize the full clinical potential of this innovative methodology.

Part 2: Radiomics for Tumor sub-regions: r1 & r3

The radiomics feature extraction and selection steps outlined in part 1 were applied to each tumor sub-region, namely r1 and r3. Subsequently, we examined shared features within these two sub-regions to evaluate if they displayed significant differences.

6.2 Results

Part 1: Radiomics for Whole Tumor

6.2.1 Reduction of radiomics and elimination of outliers

Testing features reproducibility

As mentioned in the preceding materials and methods section, a critical feature selection step is necessary to mitigate the risk of overfitting. This specific procedure is exclusively applied to the Sunitinib group. The primary objective is to explore potential correlated patterns between the Sunitinib group and the Control group. Subsequently, after the reduction of radiomic features, the chosen features are extended to the Control group for a comprehensive examination of shared states between the two groups.

In the context of reproducibility analysis for each of the three modalities, namely PET, CT, and UUDI, it's important to note that among them, CT Volume exhibited a notably low level of reproducibility for the CT modality. This outcome can be attributed to the challenges encountered in PET/CT/UUDI images, where the positioning of the UUDI probe over the tumor introduced significant noise and created shadows that adversely affected the diagnostic quality of the CT scans. Consequently, the analysis was proceeded with PET, UUDI radiomics, and CT Volume (mesh-based), with the exclusion of other CT radiomics features. It's worth mentioning that the CTVolume parameter provides valuable information about the tumor size. For detailed results, please refer to Tables 1 and 2, which present the findings using the ICC and CCC correlation coefficients for PET and UUDI.

For each of the PET and UDDI modalities the number of the radiomic features was reduced as following Figure 6.1:

	PET			UUDI		
	ICC<0.5	0.5≤ICC<0.8	ICC≥0.8	ICC<0.5	0.5≤ICC<0.8	ICC≥0.8
morphological	0 (0.00%)	9 (1.85%)	20 (4.11%)	0 (0.00%)	8 (1.64%)	21 (4.31%)
first order	26 (5.34%)	3 (0.62%)	21 (4.31%)	31 (6.37%)	2 (0.41 %)	17 (3.49%)
second order	145 (29.77%)	5 (1.03%)	0 (0.00%)	150 (30.80%)	0 (0.00%)	0 (0.00%)
Higher order	252 (51.75%)	6 (1.23%)	0 (0.00%)	256 (52.57%)	0 (0.00 %)	2 (0.41%)
TOTAL	423 (86.86%)	23 (4.72%)	41 (8.42%)	437 (89.73%)	10 (2.05%)	40 (8.21%)

Table 6.1: The outcomes of the reproducibility investigation concerning PET and UUDI radiomics, as assessed through the ICC, are presented. Within each imaging modality, we categorized radiomics into three groups: those with low reproducibility (ICC $<$ 0.5), medium reproducibility (0.5$\leq$ ICC $<$ 0.8), and high reproducibility (ICC $\leq$ 0.8). The distribution of radiomics across these categories, including the total number of radiomics and the percentage extracted in each technique, is displayed. In total, 487 radiomics were examined per modality.

- Number of radiomics with high ICC : PET 487→41, UUDI 487→40.
- Number of radiomics with average ICC : PET 487→23, UUDI 487→10.
- Number of radiomics with high CCC : PET 487→484, UUDI 487→472.

By applying the criterion that a radiomic is deemed reproducible when it exhibits both a high CCC and medium or high ICC simultaneously, the following results are achieved:

- Total count of reproducible radiomics: PET→64, UUDI→49.

Selecting Best Configuration

Subsequently, an evaluation was conducted to determine the most stable configuration. For PET, the most stable configuration was identified as one utilizing FBS discretization with a bin size of 1, a voxel size of 1 mm, and cubic interpolation. Conversely, for UUDI, the configuration demonstrating the highest stability employed FBN discretization with 16 bins, a voxel size of 0.2 mm, and near-neighbor interpolation (nearest).

Testing features redundancy

In the following stage, redundancy analysis is conducted individually for each modality and in a combined manner. This analysis is visualized using the "plot corrmat" function in MATLAB, with adjusted representation limits to exclusively display correlated instances.

	PET		UUDI	
	CCC<0.9	CCC≥0.9	CCC<0.9	CCC≥0.9
morphological	0 (0.00%)	29 (5.95%)	0 (0.00%)	29 (5.95%)
first order	3 (0.62%)	47 (9.65%)	12 (2.46%)	38 (7.80%)
second order	0 (0.00%)	150 (30.80%)	0 (0.00%)	150 (30.80%)
Higher order	0 (0.00%)	258 (52.98%)	3 (0.62%)	255 (52.36%)
TOTAL	3 (0.62%)	484 (99.38%)	15 (3.08%)	472 (96.92%)

Table 6.2: The findings from the analysis of PET and UUDI radiomics reproducibility using the CCC are presented. Within each imaging modality, radiomics were categorized into two groups: those exhibiting low reproducibility (CCC < 0.9) and those with high reproducibility (CCC ≥ 0.9). The distribution of radiomics among these categories, including the count for each type and the total number categorized according to their CCC values, is illustrated. The analysis encompasses a total of 487 radiomic features per modality.

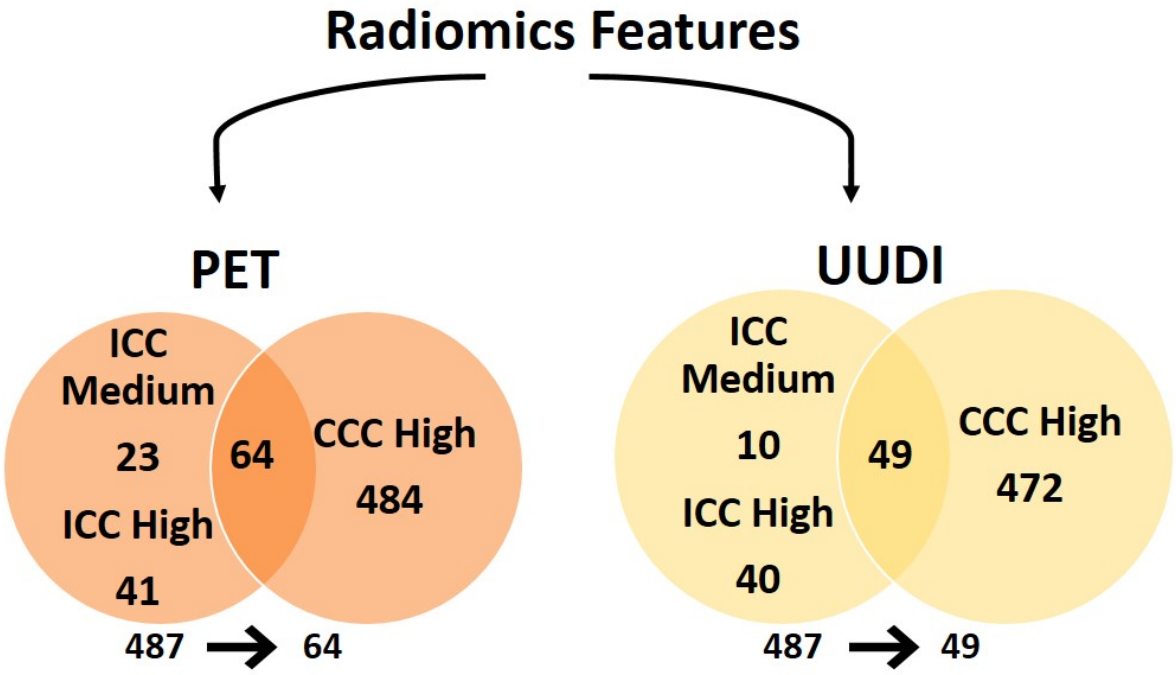

Figure 6.1: Scheme representing the reduction in the number of features after performing the reproducibility study for each of the PET and UUDI modalities.

- Intra-modality correlation: PET 64→36, UUDI 49→24. Along with CT radiomics, there are 61 radiomics.
- Inter-modality cross-correlation: 61→57.

Inter-modality cross-correlation: This results in 61 correlations, which are further reduced to 57 after analysis.

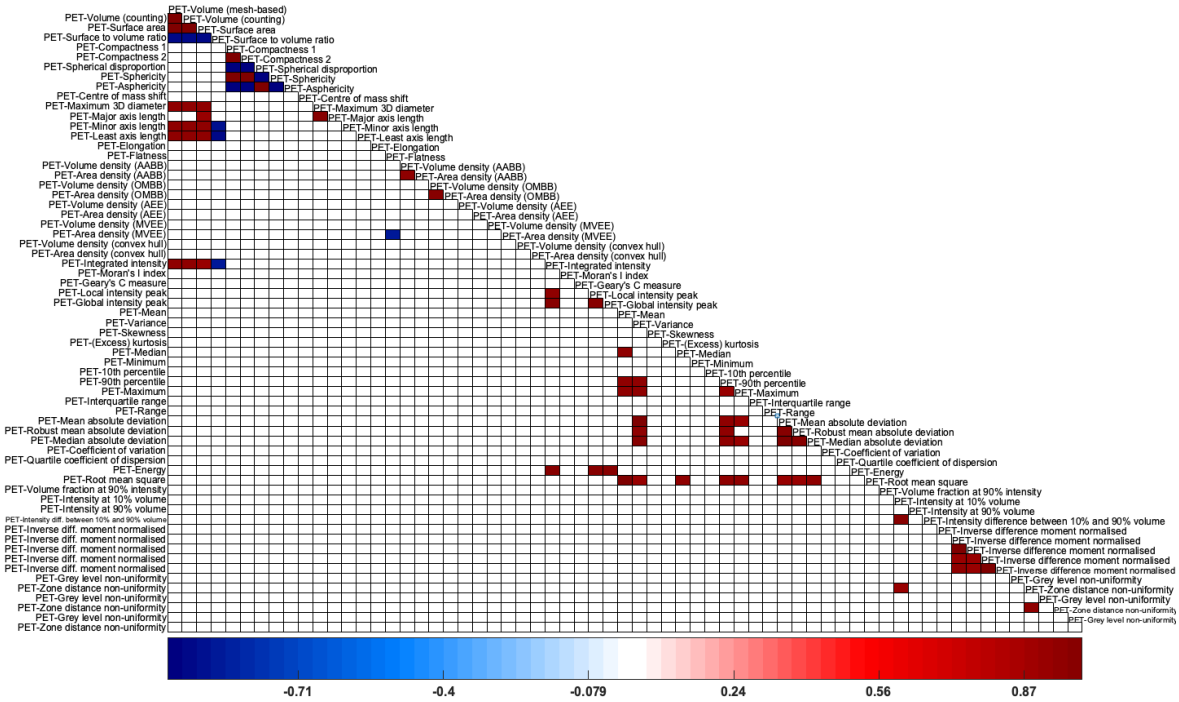

Figure 6.2: PET correlation matrices of the Sunitinib group.

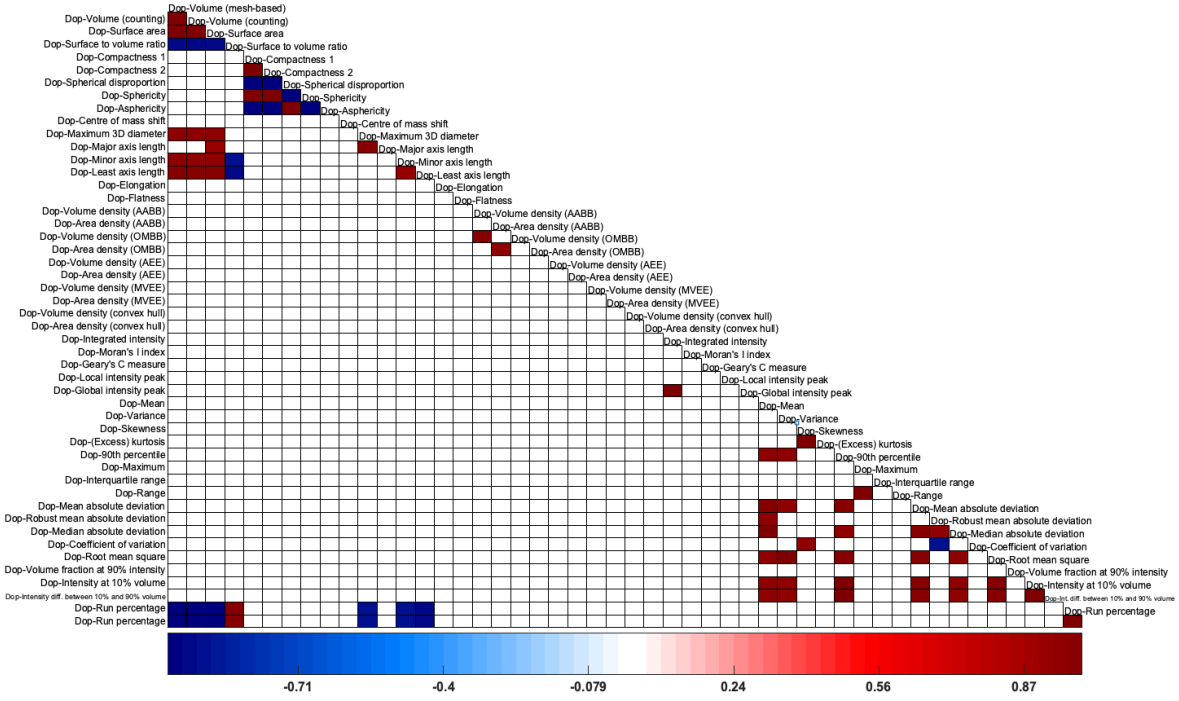

Figure 6.3: Doppler correlation matrices of the Sunitinib group.

From the correlation matrices, we obtain the following results: - Correlation between radiomics of the same imaging modality: PET 64→36, UUDI 49→24. Along with CT ra-

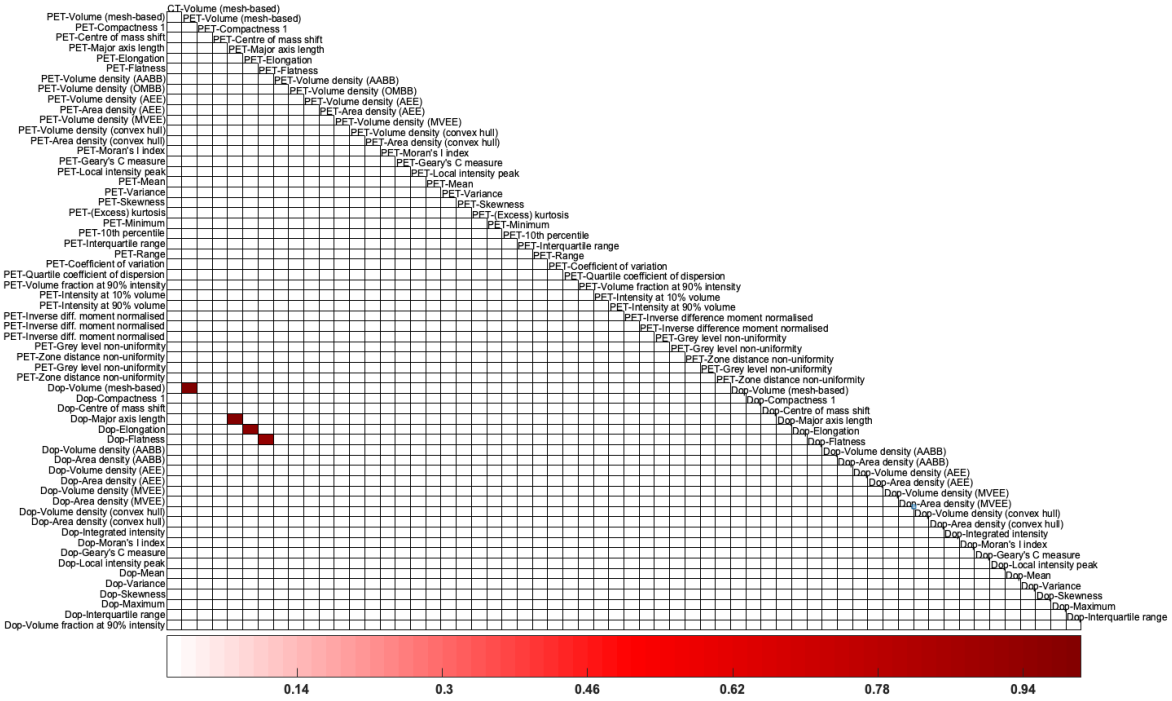

Figure 6.4: Inter-correlation matrices between PET and Doppler features of the Sunitinib group.

diomics, there are 61 radiomics. - Cross correlation:61→57

Outlier Removal

Regarding the removal of outliers, it's important to note that this process entails the exclusion of specific cases rather than radiomic features:

- **Control Group:** Out of the 29 available cases (originally 32, but 3 were not in the database), 8 cases were omitted, leaving 21 cases for cluster formation.
- **Sunitinib Group:** Out of the 55 available cases (originally 56, but 1 was not in the database), 12 cases were excluded, resulting in 43 cases for cluster formation.

Removal of Low Variance Features (Informativity test)

Furthermore, radiomics exhibiting low variance, which were deemed non-informative, were also excluded from the analysis. Those with a coefficient of variation (cv) < 0.3 were reduced, resulting in a total reduction of radiomics from 57 to 19.

A comprehensive overview of all the steps involved in reducing features is depicted in Figure 6.5. As a result of these feature reduction procedures, the count of radiomics within

the Sunitinib group has been significantly decreased from 1461 to 19, a number deemed suitable for performing hierarchical clustering.

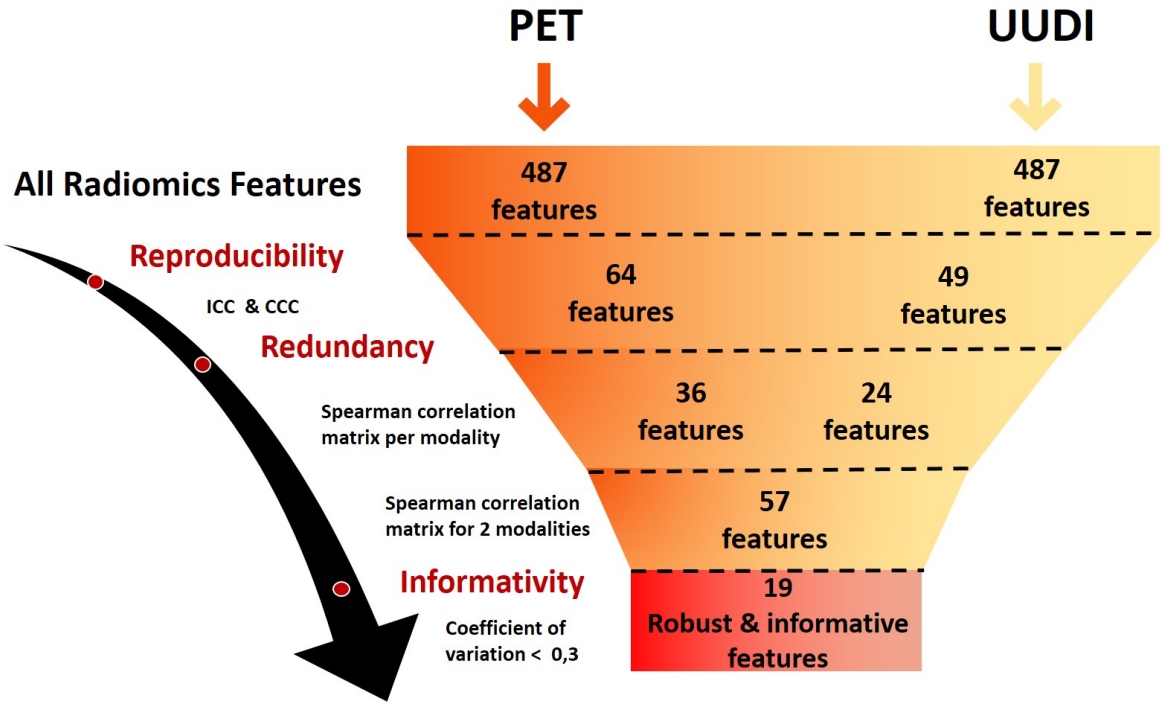

Figure 6.5: Scheme representing the reduction in the number of features after performing all the feature reduction steps for each of the PET and UUDI modalities.

6.2.2 Hierarchical clustering of the Sunitinib group

Upon the application of hierarchical clustering to the selected radiomics features of the sunitinib group, the analysis revealed the formation of three primary clusters: Ar_s,Br_t, and Cr_s, along with two sub-clusters within group Br_t: $B1r_t$ and $B2r_t$. The visual representation of this outcome is presented in Figure 6.6.

Based on the extracted radiomics and the biological insights they offer, these groups exhibit distinct characteristics. For a more comprehensive description of each individual radiomic feature, please refer to Annex A:

- Cluster Ar_t is distinguished by the presence of small tumors, evidenced by their limited volumes in both CT and PET scans, along with minimal metabolic activity, denoted by low values of the Local Intensity Peak radiomic feature. Within this group, these tumors exhibit notable metabolic heterogeneity, as indicated by a substantial region with low values in metrics such as radiomics variance, non-uniformity of various orders, and high values of Skewness. In terms of vascularization, it displays an early stage, characterized by heterogeneity and variable perfusion, a description supported by metrics such as Doppler variance, volume, and fluctuating mean values.

- Subcluster $B1r_t$ represents the initial sub-stage within cluster Br_t, and it is in close proximity to cluster Ar_t, which denotes the most favorable stage of tumor development. In this sub-stage, we observe a slight increase in both CT and PET volumes, indicating the commencement of tumor growth. The metabolic activity is notably high, evident through the elevated value of the Local Intensity Peak radiomic feature, and it demonstrates heterogeneity, as there are concentrated areas with high values within the radiomics that report heterogeneity in PET. Vascularization, on the other hand, is characterized by low values, including low Volume Fraction at 90% Intensity, mean, Integrated Intensity, and Local Intensity Peak for UUDI, while Variance reflects homogeneity with low values. This substage signifies a tumor in its early stages of size and metabolic development. Glycolysis is beginning to exhibit heterogeneity, and vascularization is slowing down, transitioning towards a more homogeneous state.

- Subcluster $B2r_t$ represents the final substage within cluster B, and it is situated in close proximity to Cr_t, which denotes the least favorable stage of tumor development. Within this substage, both CT and PET volumes are notably elevated, particularly as the tumors approach Cr_t. Metabolic activity is exceptionally high and exhibits marked heterogeneity, mirroring the state of vascularization. These characteristics collectively point to a more aggressive and advanced stage of tumor development, bearing greater similarity to stage Cr_t.

- The Cr_t cluster is defined by its larger tumors, indicated by high CT and PET volumes, and significant metabolic activity, as reflected in the elevated Local Intensity Peak radiomic feature, which implies heightened glycolysis. These tumors are metabolically homogeneous, as evidenced by the presence of very high values in radiomics related to tumor heterogeneity, further confirmed by the low value of Skewness. Moreover, vascularization within this cluster is notably high, demonstrated by the elevated values of Local Intensity Peak and Integrated Intensity. Additionally, radiomics related to vascularization heterogeneity exhibit low values in this cluster.

As previously conducted in Chapter 4, to enhance our comprehension of the clusters and to identify responses to Sunitinib treatment, we analyze the mice's evolutionary trajectories—observing the clusters in which they are categorized each week. The findings are presented in Table 6.3

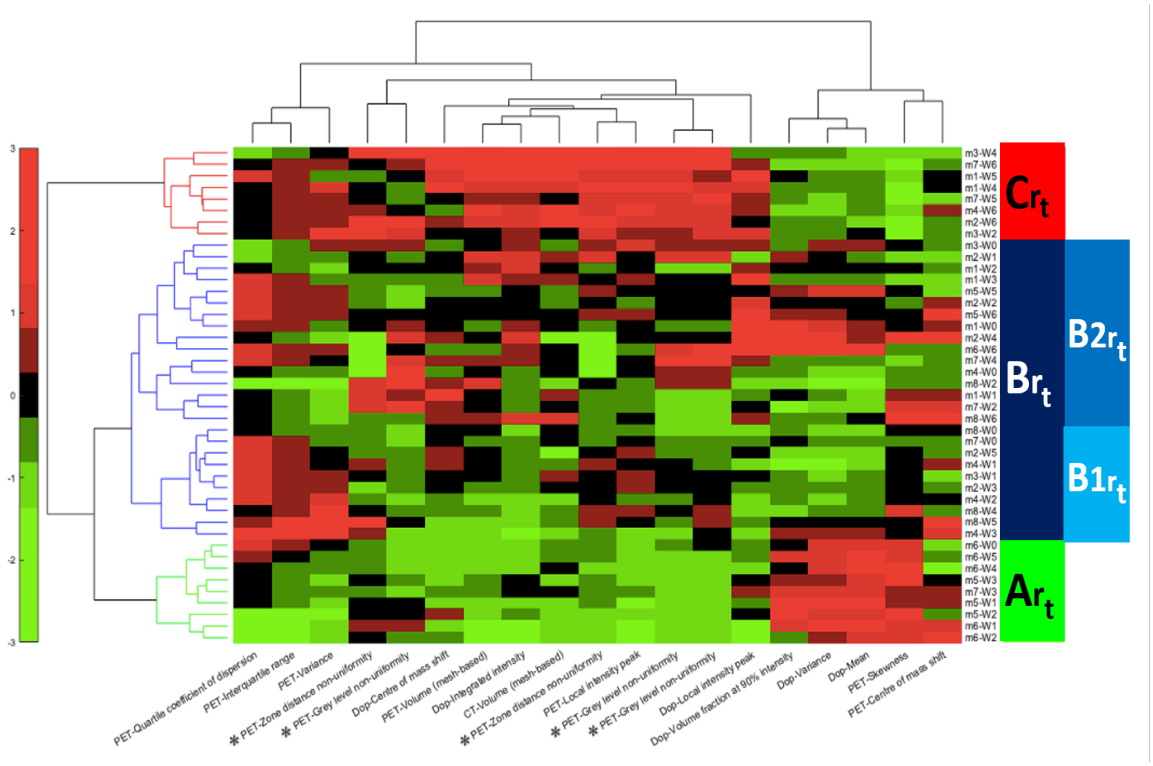

Figure 6.6: Heatmap and hierarchical clustering performed on the $D^{suni}_{training}$ dataset. Four clusters (Ar_t, $B1r_t$, $B2r_t$, and Cr_t) were identified.

Table 6.3: Evolutionary path of sunitinib-treated mice of the training set. Items marked as * indicate missing classification due to the absence of corresponding PETRUS data. Clusters that were assigned by the RF model are underlined.

Mouse Number	**Baseline**	**Week 1**	**Week 2**	**Week 3**	**Week 4**	**Week 5**	**Week 6**
mouse 1	Br_t	Br_t	Br_t	Br_t	Cr_t	Cr_t	**outlier**
mouse 2	**outlier**	Br_t	Br_t	Br_t	Br_t	*	Cr_t
mouse 3	Br_t	Br_t	Cr_t	**outlier**	Cr_t	Cr_t	**outlier**
mouse 4	Br_t	Br_t	Br_t	Br_t	*	**outlier**	Cr_t
mouse 5	**outlier**	Ar_t	Ar_t	Ar_t	**outlier**	Br_t	Br_t
mouse 6	Ar_t	Ar_t	Ar_t	**outlier**	Ar_t	Ar_t	Br_t
mouse 7	Br_t	**outlier**	Br_t	Ar_t	Br_t	Cr_t	Cr_t
mouse 8	Br_t	**outlier**	Br_t	**outlier**	Br_t	Br_t	$B1r_t$

Some of the rules explaining the passage from cluster to another were re-obtained by the follwing the same protocol on the radiomics features:

- Mice found in cluster Ar_tthey stayed in Ar_t or moved to cluster Br_t.

- Mice within cluster Br_t persist within the same cluster (Br_t), transition to cluster Ar_t, or transition to Cr_t. Notably, the subclusters of Br_t depicted in the dendrogram offer valuable insights into the direction of these trajectories: indicating a direction towards Ar_t for cases classified as $B1r_t$, or towards Cr_t for those identified as $B2r_t$.
- All mice reaching the advanced (cluster Cr_t) stage originated from cluster $B2r_t$.
- no mouse reversed from the advanced tumor stage (cluster C) to a less advanced stage.

As observed, the mice in cluster Ar_t are linked to either the baseline week or week 1, signifying that this cluster represents the initial and most favorable tumor stage. However, some mice do not originate in cluster Ar_t and are placed directly in the intermediate stage Br_t, indicating a more advanced tumor at the start of treatment. Within cluster Cr_t, cases from later weeks are primarily located, except for mouse 2, which, by week 2 of treatment, is already positioned in this cluster, denoting a more advanced and unfavorable tumor stage.Conversely, mice 5, 6, and 8 display a positive response to Sunitinib treatment, as they do not progress to the most advanced stage by the study's end. Notably, their volumes in PET and CT during the final treatment week are moderately to high, while their metabolic and vascular evolution is moderate. This suggests a favorable response to antiangiogenic treatment, as indicated by the clustergram.

Figure 6.7 illustrates the hierarchical clustering of the Control group, revealing the presence of two primary clusters: Ar_c and Cr_c.

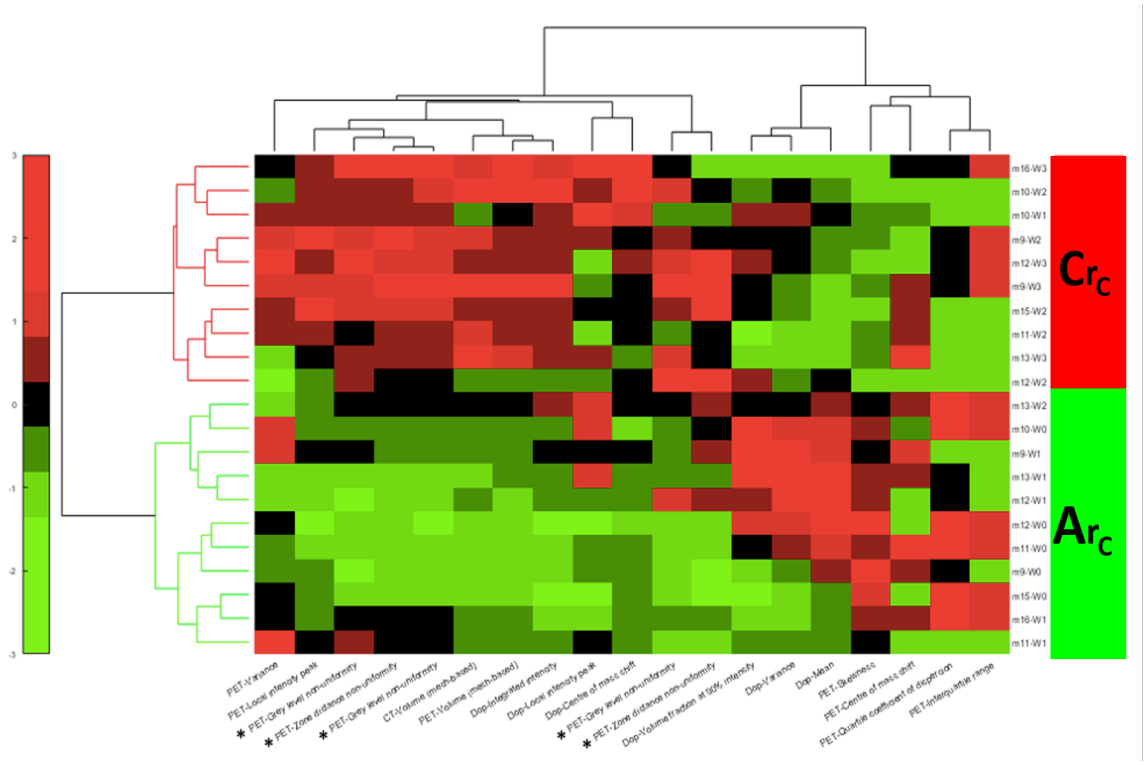

Figure 6.7: Heatmap and hierarchical clustering performed on the $D^{con}_{training}$ dataset. Two clusters (Ar_c, Cr_c) were identified.

Part 2: Radiomics for Tumor sub-regions: r1 & r3

Testing feature reproducibility

For each of the PET and UDDI modalities the number of the radiomic features was reduced as following 6.8-A for r1 :

- Number of radiomics with high ICC : PET 487→42, UUDI 487→41
- Number of radiomics with average ICC : PET 487→26, UUDI 487→3.
- Number of radiomics with high CCC : PET 487→481, UUDI 487→312.

By applying the criterion that a radiomic is deemed reproducible when it exhibits both a high CCC and medium or high ICC simultaneously, the following results are achieved: — Total count of reproducible radiomics: PET→68, UUDI→37

For each of the PET and UDDI modalities the number of the radiomic features was reduced as following 6.8-B for r3 :

- Number of radiomics with high ICC : PET 487→42, UUDI 487→50
- Number of radiomics with average ICC : PET 487→26, UUDI 487→6.
- Number of radiomics with high CCC : PET 487→484, UUDI 487→417.

By applying the criterion that a radiomic is deemed reproducible when it exhibits both a high CCC and medium or high ICC simultaneously, the following results are achieved: — Total count of reproducible radiomics: PET→68, UUDI→47

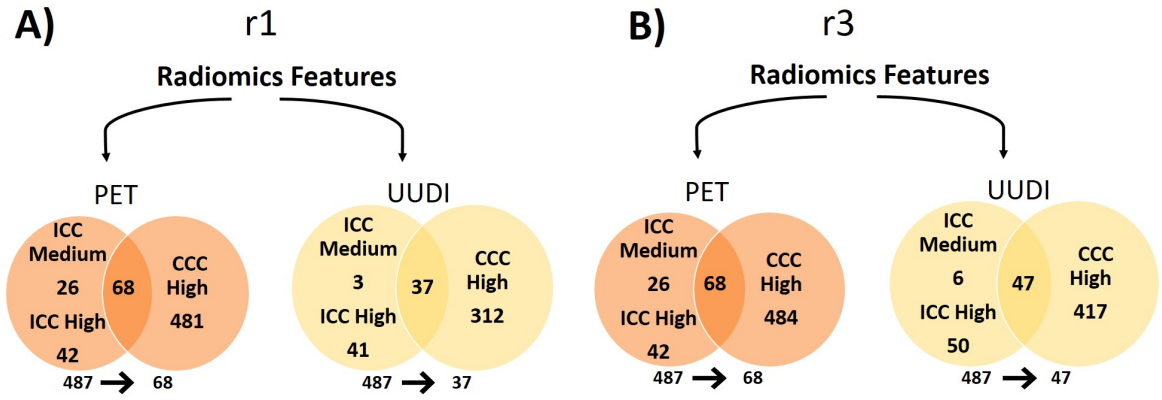

Figure 6.8: Scheme representing the reduction in the number of features after performing the reproducibility study for each of the PET and UUDI modalities: A) for tumor sub-region r1 and B) for tumor sub-region r3.

Testing feature redundancy

In the following stage, redundancy analysis is conducted individually for each modality (PET and UUDI) and in a combined manner 6.9.

1. For r1:
    - Intra-modality correlation: PET 68→37, UUDI 37→19. Along with CT radiomics,there are 56 radiomics.
    - Inter-modality cross-correlation: 56→49.
2. For r3:
    - Intra-modality correlation: PET 68→33, UUDI 47→26. Along with CT radiomics,there are 59 radiomics.
    - Inter-modality cross-correlation: 59→50.

Removal of Low Variance Features (Informativity test)

As discussed earlier, features with low variance, considered non-informative, were excluded from the analysis. Those with a coefficient of variation (cv) less than 0.3 were pruned, leading to a substantial reduction in radiomics—from 49 to 11 in r1 and 50 to 18 in r3.

Figure 6.9 provides a comprehensive overview of the steps taken to reduce features. These reduction procedures notably decreased the count of radiomics within the Sunitinib group, reducing it from 1461 to 11 in r1 and from 1461 to 18.

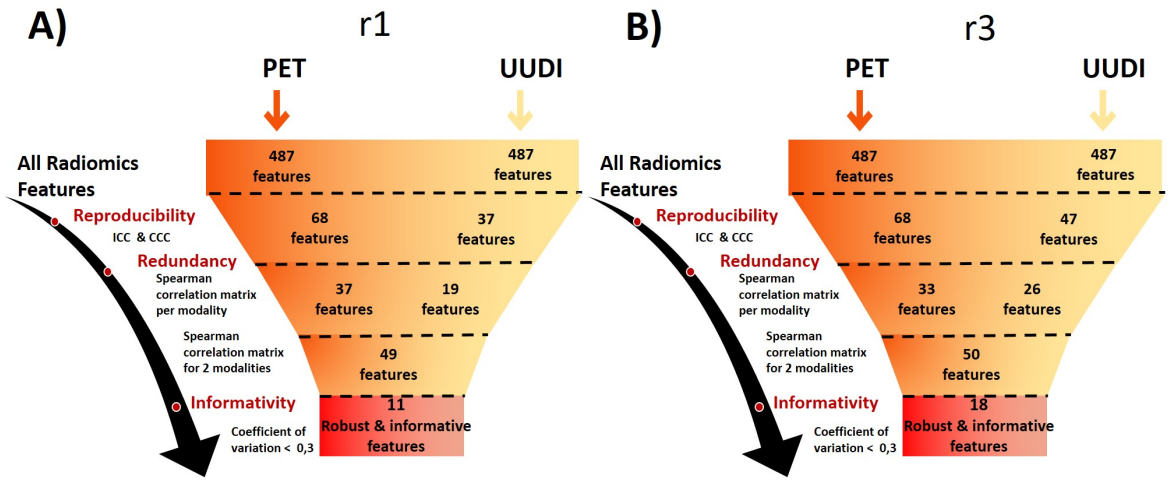

Figure 6.9: Scheme representing the reduction in the number of features after performing all the feature reduction steps for each of the PET and UUDI modalities: A) for tumor sub-region r1 and B) for tumor sub-region r3.

Common Features between r1 and r3

List of the most robust and informative features is presented in Figure 6.10. 6 features were common 1 from CT, 5 from PET and 1 from Doppler.

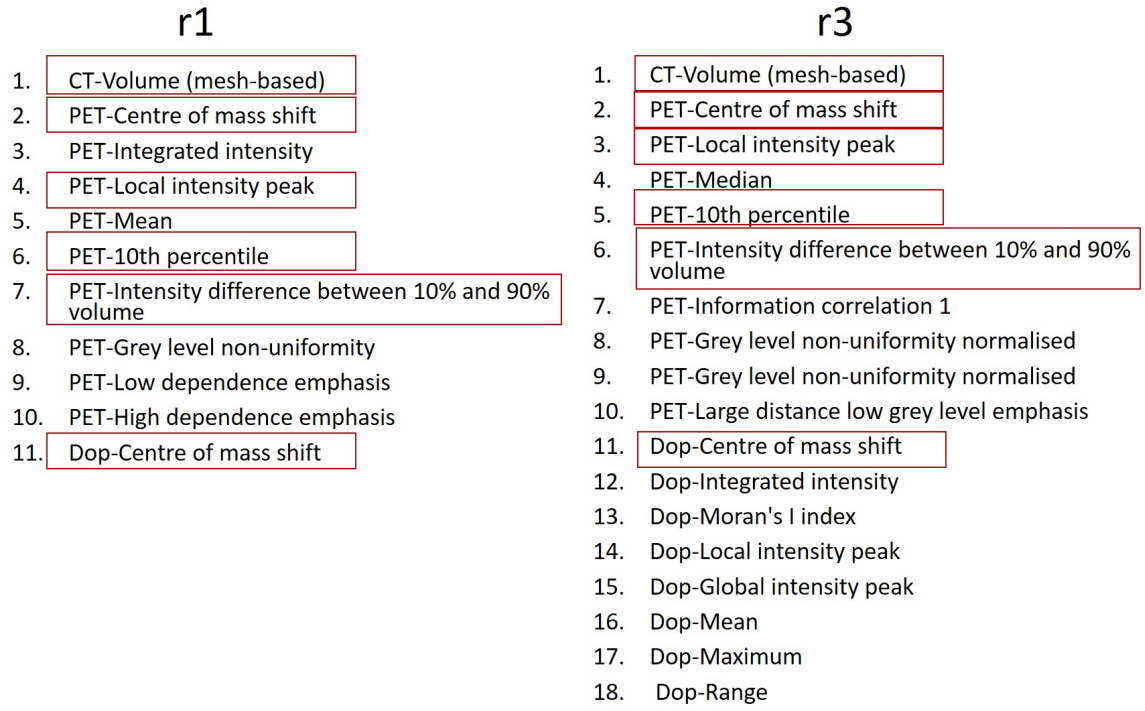

Figure 6.10: List of the most robust and informative radiomics features obtained after feature selection steps for each of tumor sub-regions: A) r1 and B) r3

We investigated potential significant differences for each common radiomics feature between r1 and r3. Notably, the CT-Volume (mesh-based) and PET-Local intensity peak emerged as the most significant features, demonstrating statistical significance with p-values less than or equal to 1E-3. Additionally, the Dop-Centre of mass shift and PET-Intensity difference between 10% and 90% volume exhibited significant differences, with p-values less than or equal to 1E-2. The PET-10th percentile also showed a notable difference between the two regions, reaching statistical significance with a p-value of 0.05. The only feature that did not demonstrate a significant difference between r1 and r3 was PET-Centre of mass shift.

6.3 Discussion

In this chapter, we employed radiomics analysis as a powerful tool to first reevaluate and redefine the treatment response stages within both the control and sunitinib-treated groups. Second, to explore whether specific radiomics features could effectively describe the distinct characteristics of r1 and r3. These tumor sub-regions, as elucidated in Chapter 5, are associated with positive and negative treatment responses, respectively.

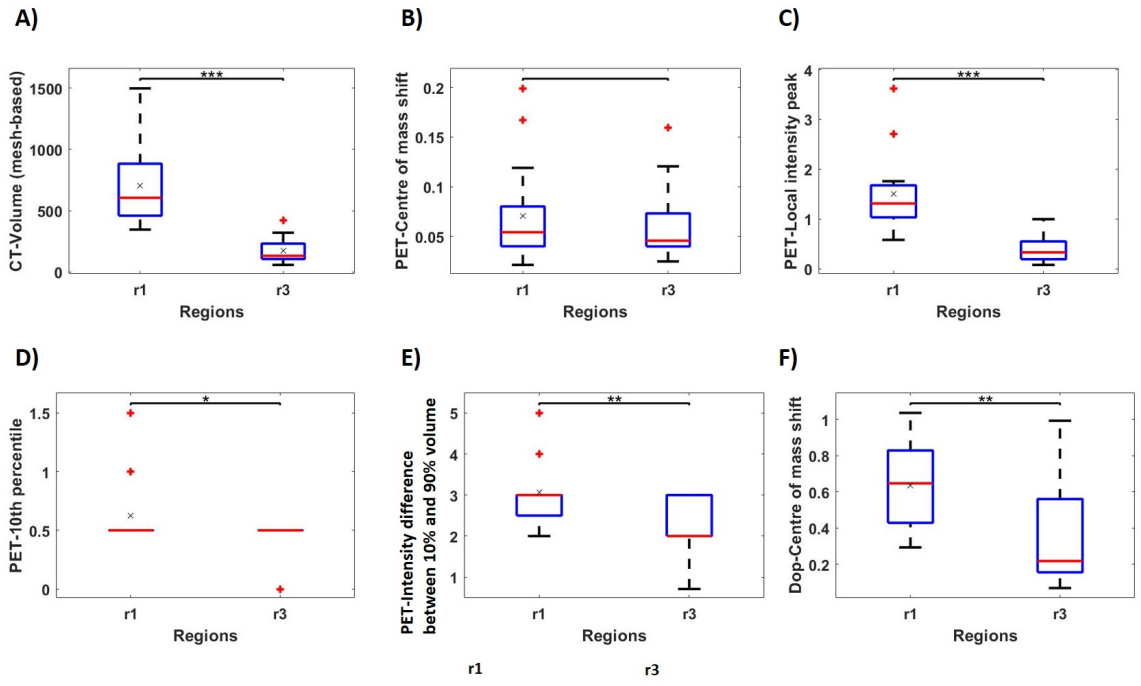

Figure 6.11: Boxplots for each of common radiomics features showing the level of significance of each feature between r1 and r3. * represents p<=0.05, ** represents p<=1E-2, *** represents p<=1E-3

One aspect of our radiomics analysis is the wealth of information it provides regarding the metabolic and vascular characteristics of the tumors. Radiomic features, being quantitative descriptors of tumor texture, shape, and intensity patterns, offer a comprehensive perspective on the intra-tumoral heterogeneity that may not be fully captured by traditional imaging metrics alone.

The interpretation of these radiomic features, we gain access to finer details, allowing us to identify variations in metabolic activity and vascularization within and across treatment response stages. This enhanced insight could prove pivotal in understanding the underlying biological processes at play during treatment.

In the second part of our analysis, we identified six common, reproducible, informative, and redundant radiomic features between r1 (associated with positive treatment response) and r3 (associated with negative treatment response), as established in Chapter 5. Notably, five of these radiomic features have the potential to act as markers, with their levels serving as predictors of treatment response

The ability to extract detailed information from radiomic features holds promising clinical implications. Beyond confirming treatment response stages, the nuanced understanding of metabolic and vascular characteristics opens avenues for more targeted and personalized interventions. Future studies could explore the integration of radiomics into clinical decision-making processes, potentially paving the way for tailored therapeutic strategies based on the unique radiomic profile of each tumor.

In conclusion, our radiomics analysis not only validates our previous findings but also enriches our understanding of treatment responses by providing intricate details regarding tumor metabolic and vascular characteristics. The potential clinical impact of these insights positions radiomics as a valuable addition in the realm of precision medicine for paragangliomas.

Chapter 7

Discussion and Perspectives

7.1 Discussion

Chapters 4 and 5 of our thesis introduced two distinct Machine Learning (ML) methodological approaches aimed at delineating treatment response patterns in PGL (paraganglioma) mice models. These approaches were designed to firstly pinpoint treatment response based on the therapeutic target, specifically focusing on the vascular characteristics, in conjunction with metabolic and morphological hallmarks. The secondary objective was to identify tumor subregions critical for predicting the observed treatment response stages. These methodologies were thoroughly examined and validated in two pivotal studies. The first study, "Machine learning of multi-modal tumor imaging reveals trajectories of response to precision treatment" (Mansouri et al., 2023), highlighted the major results of our investigation. Furthermore, the second study, entitled "Intratumoral Heterogeneity by Molecular-Vascular Profiling for Predicting Drug Resistance" which we are considering for publication, emphasized our effective utilization of intratumor segmentation using a computationally efficient ML framework. The segmentation revealed distinct subregions within the tumor, and these specific areas were pivotal in accurately predicting different stages of treatment response.

In the first study the study of treatment response in PGL mice led to the identification and categorization of three distinct stages: Stage A, subdivided Stage B into B1 and B2, and Stage C. Each stage exhibited unique characteristics in terms of metabolic, vascular, and morphological features. Stage A was representative of an early stage, featuring small and poorly developed tumors with low vascularization and heterogeneous FDG (Fluorodeoxyglucose) uptake, forming cluster C. Stage C, on the other hand, represented an advanced stage, showing large tumors, prominent vessels, and relatively homogeneous FDG uptake, akin to end-stage cancer disease. Between the two intermediate stages, B1 and B2, there were distinctive differences. B1 included small-sized tumors with moderate vascularization and heterogeneity in glucose uptake distribution. Conversely, B2 encompassed moderate-sized tumors with comparatively lower heterogeneity in glucose uptake and moderate vascularization. The amalgamation of features extracted from the three modalities - metabolic, vascular, and morphological - played a crucial role in defining these

distinct stages. Our research highlighted the interdependency of these modalities in characterizing and differentiating the stages of treatment response. Removing any one of these modalities hindered the accurate identification of these stages, emphasizing the need for a comprehensive multi-modal approach. Utilizing Amira software, we conducted a more detailed analysis, revealing a pivotal distinction between the two intermediate stages, B1 and B2, primarily related to vascular morphology. In B1, vessels exhibited characteristics of being short, thin, and proliferative. However, in B2, these vessels were notably larger and longer. This variation in vascular morphology between the two sub-stages under Stage B offered critical insights into the progressive changes occurring within the tumors during the intermediate phases of treatment response. These detailed findings underscore the significance of multi-modal analysis in understanding treatment response stages. The collaboration and interplay of metabolic, vascular, and morphological features provided a comprehensive understanding of the evolution and progression of the tumors, delineating distinct stages crucial for assessing the response to treatments. The observations on vascular morphology within the intermediate stages further shed light on the dynamic changes occurring during the treatment, offering a more nuanced understanding of the responses to therapeutic interventions.

In the second study, the focus was on identifying and characterizing sub-regions within the tumors, resulting in the determination of four distinct sub-regions. Each sub-region displayed varying metabolic and vascular characteristics. What emerged as particularly significant was the observation that one specific region, denoted as r1, was notably prevalent in the advanced Stage C, intermediate in Stage B2, less apparent in Stage B1, and completely absent in Stage A. This pattern indicated that the presence and proportion of region r1, characterized by heightened metabolic and vascular activity, could potentially serve as a predictive marker for treatment resistance or escape. Conversely, another sub-region, r3, characterized by diminished metabolic and vascular activity, was prominently found in Stage A, less frequent in Stages B1 and B2, and completely absent in Stage C. This sub-region, showing a lower metabolic and vascular profile, was strongly associated with a favorable response to treatment. The distinct distribution and prevalence of r3 across the different stages suggested its potential as a biomarker for a positive response of PPGL (pheochromocytoma and paraganglioma) to sunitinib treatment. The findings from this study suggest that the presence or absence of specific sub-regions within the tumor could serve as predictive biomarkers for treatment response. Notably, the contrasting roles played by regions r1 and r3 in predicting treatment outcomes highlight the potential utility of these sub-regions as indicators of the tumor's response to sunitinib therapy. These observations signify a substantial advancement in the identification of specific tumor regions that could potentially guide clinical decision-making, aiding in the prediction of treatment responses and potentially facilitating more tailored and effective treatment strategies for PPGL.

Our research underscores the substantial importance of machine learning in extracting and utilizing handcrafted features from images to predict treatment response. These features allowed us to discern and comprehend treatment response patterns that were challenging to perceive through conventional observation methods. The application of advanced computational approaches in analyzing intricate data patterns was crucial in uncovering these intricate nuances.

Our research underscores the substantial importance of machine learning in extracting and utilizing handcrafted features from images to predict treatment response. These features allowed us to discern and comprehend treatment response patterns that were challenging to perceive through conventional observation methods. The application of advanced computational approaches in analyzing intricate data patterns was crucial in uncovering these intricate nuances.

In spite of utilizing a relatively low number of mice (8 in the sunitinib-treated group), our database was robust due to the longitudinal nature of the study. By consolidating data from 7 time points for each of the 8 mice, we amassed a total of 52 cases (with 2 missing cases). Our methodological approach treated each of the 52 cases as an independent record, significantly enriching the dataset. From a biological standpoint, the coherence achieved with 8 mice sharing the same tumor origin provided more cohesive insights compared to studying 50 patients with diverse mutation origins. This comprehensive and focused approach strengthened the validity and relevance of our findings, offering a profound understanding of treatment response dynamics.

7.2 Perspectives

The applications of our findings open substantial avenues for future research and clinical application. Firstly, the incorporation of machine learning in analyzing tumor characteristics, specifically regarding treatment response, serves as a springboard for further advancements in precision medicine. This aligns with the current trend of leveraging computational methods to refine treatment strategies and improve patient outcomes. Moreover, the emphasis on the therapeutic target, particularly in cancer treatment, holds immense promise. By focusing on specific molecular or vascular aspects of tumors, the development of tailored treatments based on these precise characteristics can revolutionize oncological interventions.

The shift from a macroscopic evaluation of tumors to a finer-grained analysis of their molecular and vascular profiles is an area ripe for further exploration. The use of machine learning algorithms to detect, segment, and predict treatment response from these intricate features is not only a substantial scientific leap but also a potential clinical breakthrough. Further studies could expand the application of these methodologies in larger cohorts, integrating diverse modalities and tumor types to corroborate and broaden the findings established in this thesis.

Additionally, the longitudinal nature of our study, despite its relatively smaller sample size, underscores the significance of a more in-depth examination over time. This approach can be extrapolated to larger populations, promoting more comprehensive and nuanced understandings of treatment response dynamics.

In conclusion, our thesis underscores the promising potential of combining machine learning methodologies with a focus on therapeutic targets in delineating treatment response. The perspectives offered here indicate the wider applications and implications of these findings, providing a robust foundation for further research and potential clinical

implementation in precision medicine.

Chapter 8

LIST OF PUBLICATIONS AND ACCOMPLISHMENTS

1. Mansouri N, Balvay D, Zenteno O, Facchin C, Yoganathan T, Viel T, Herraiz JL, Tavitian B, Pérez-Liva M. Machine learning of multi-modal tumor imaging reveals trajectories of response to precision treatment. Cancers. 2023 Mar 14;15(6):1751.
   status: Journal article published

2. Alejandro Ariza Carrasco, Thulaciga Yoganathan, Nesrin Mansouri, José M. Udías Moinelo, Joaquín L. Herraiz, Bertrand Tavitian and Mailyn Pérez Liva. Remodelling of Cerebral FDG Uptake Kinetics in An Acute Stress-Induced Takotsubo-Type Rat Model. 10th International Conference on Biomedical Engineering and Systems (ICBES). Londres, Reino Unido, agosto 2023. Paper ICBES 131. ISBN: 978-1-990800-26-9. DOI: 10.11159/icbes223.131
   status: Article published

3. Mansouri N, Herraiz JL, Tavitian B, Pérez-Liva M. Analysis of Intratumoral Heterogeneity by Molecular-Vascular Profiling for Predicting Drug Resistance.
   status: Journal article submitted

4. Submitted PATENT application to INSERM transfert: **Title** = Method For Predicting The Tumor Stage of a Subject in a Treatment Phase and Associated Devices, **Reference Number** = 23P0284, **Date** = June 13, 2023.

CONFERENCES

- IEEE International Symposium on Biomedical Imaging (ISBI) 2021 - online - I presented poster presentation
- European Molecular Imaging Meeting (EMIM) 2021 - online - I presented poster presentation
- European Molecular Imaging Meeting (EMIM) Emim 2022- Greece - I presented poster presentation

- European Molecular Imaging Meeting (EMIM) Emim 2023- Austria - I presented poster presentation
- International Conference on Biomedical Engineering and Systems. Oral presentation by Ariza Carrasco

MENTORING

Mentoring 1: Mentoring master 1 student from Biomedical engineering (BME) program à l'Université de Paris. Title: Radiomics Analysis of the Effect of Sunitinib Treatment on SDHb-/- Experimental Paraganglioma;

Mentoring 2: Mentoring master 1 student- Miguel GONZÁLEZ MÁRQUEZ - from Biomedical Physics (BME) program à Complutense University of Madrid. Title: Study of Tumor Heterogenity by Radiomic Analysis

RESEARCH STAYS

Three months abroad collaboration with nuclear physics group at the Complutense University of Madrid, Spain, (July, November, and December, 2022)

SOCIAL CONTRIBUTIONS

Organizer and board member of the first congress of the Early Career Research (ECR) cardiovascular conference, December 2022

Thesis Summary

La thèse s'articule autour de sept chapitres. Le chapitre 1 sert d'introduction, élucidant le contexte et les objectifs de la recherche. Le chapitre 2 procède à un examen exhaustif de la littérature, jetant les bases de l'exploration ultérieure. Le chapitre 3 décrit minutieusement la base de données, en expliquant sa structure et sa méthode d'acquisition. Les chapitres 4, 5 et 6 portent respectivement sur le premier, le deuxième et le troisième projet, chacun apportant un éclairage unique à l'ensemble du récit. Le dernier chapitre, le chapitre 7, s'engage dans une discussion approfondie, combinant les principaux résultats et proposant des orientations pour la recherche future. Cette partie fournit un résumé détaillé de chacun de ces chapitres, dans le but de faciliter une compréhension approfondie de la structure globale de la thèse.

Chapitre 1: Dans le paysage complexe de la recherche sur le cancer, les tumeurs, marquées par une croissance et une prolifération cellulaires incontrôlées, deviennent le point central. Définies par les chercheurs, les caractéristiques du cancer [7] sont des traits clés qui éclairent la nature complexe de la tumorigenèse. En explorant les interconnexions entre ces caractéristiques, nous nous intéressons plus particulièrement à la relation complexe entre les caractéristiques métaboliques et vasculaires des tumeurs. Cette exploration ouvre la voie à une étude approfondie de l'importance de l'hétérogénéité intra-tumorale (métabolique et vasculaire) dans la progression du cancer. Dans le contexte de notre thèse, où l'accent est mis sur les applications de l'IA, nous nous concentrons sur les tumeurs du paragangliome (PGL), en mettant particulièrement l'accent sur le PGL SDHB. L'examen de l'hétérogénéité métabolique et vasculaire au sein de ces tumeurs est crucial, compte tenu de son influence profonde sur la progression du cancer. En parcourant les modalités d'imagerie que sont la tomographie par émission de positons (TEP), la tomodensitométrie (TDM) et l'imagerie ultrasonique Doppler ultrarapide (UUDI) dans le contexte du PGL, nous reconnaissons l'importance de chaque technique pour saisir les facettes uniques des caractéristiques de la tumeur. Cependant, la véritable puissance réside dans la synergie de ces modalités, où la combinaison de la tomodensitométrie, de la TEP et de l'UUDI fournit une vue d'ensemble de la progression de la tumeur et de la réponse au traitement. Cette approche holistique améliore notre capacité à identifier des détails complexes qui peuvent être insaisissables lorsque l'on examine chaque modalité isolément.

À l'ère des progrès technologiques, le rôle de l'intelligence artificielle (IA) occupe une place centrale. Grâce à sa capacité à traiter de grandes quantités de données d'imagerie, l'IA joue un rôle essentiel dans la prédiction de la réponse au traitement. En exploitant

les capacités de l'IA, nous visons non seulement à améliorer notre compréhension du comportement des tumeurs, mais aussi à anticiper et à optimiser les résultats des traitements. L'intégration de l'IA dans le domaine de l'imagerie médicale représente une force de transformation, offrant de nouvelles dimensions dans notre quête pour comprendre, surveiller et combattre la progression du cancer. Dans les chapitres à venir, nous nous embarquons dans un voyage qui combine de manière complexe ces éléments, en essayant de comprendre la complexité de la dynamique du cancer dans le contexte de SDHB PGL.

Alors que nous nous penchons sur l'importance de l'IA, il est important de reconnaître l'évolution du paysage de l'imagerie médicale avec l'émergence de la radiomique. La radiomique, un domaine en plein essor de l'imagerie médicale, implique l'extraction et l'analyse de caractéristiques quantitatives à partir d'images radiographiques, ce qui permet de mieux comprendre les caractéristiques des tumeurs. En utilisant des techniques informatiques avancées, la radiomique va au-delà de l'interprétation qualitative traditionnelle, en quantifiant des modèles subtils dans les images médicales liés à la forme, à la texture et aux relations spatiales de la tumeur. Cette analyse détaillée offre des informations précieuses sur le microenvironnement et le comportement biologique de la tumeur. Les informations dérivées de la radiomique sont prometteuses pour prédire les résultats des patients et les réponses aux traitements, et pour contribuer au développement de stratégies thérapeutiques personnalisées et ciblées dans le traitement du cancer.

Objectif de la thèse: Cette thèse est consacrée à un examen complet des réponses présentées par les tumeurs du paragangliome (PGL) au traitement de précision par le sunitinib, en mettant l'accent sur les techniques avancées d'apprentissage automatique (ML). L'objectif principal est d'utiliser l'imagerie tumorale multimodale et ML pour suivre et comprendre comment les tumeurs PGL évoluent dans le temps en réponse au traitement par le sunitinib. Le deuxième objectif consiste à diviser les tumeurs PGL en sous-régions métaboliquement cohérentes à l'aide d'algorithmes de regroupement, dans le but d'identifier les sous-régions qui entraînent une résistance au sunitinib. Le troisième objectif est de développer et d'appliquer un réseau 3D-U-Net adapté aux exigences spécifiques de l'analyse des tumeurs PGL, automatisant l'identification des sous-régions à haut risque sur la base de l'interaction complexe entre les caractéristiques métaboliques et vasculaires. Enfin, le quatrième objectif est d'explorer l'utilité des caractéristiques radiomiques pour prédire la réponse au traitement dans les tumeurs PGL, en évaluant quelles caractéristiques sont les plus indicatives de la réponse au traitement par le sunitinib et comment elles sont en corrélation avec les changements dans les paramètres métaboliques et vasculaires au fil du temps.

Chapitre 2: Dans ce chapitre, nous présentons une analyse documentaire couvrant des sujets clés, y compris une vue d'ensemble de l'imagerie médicale dans le diagnostic du cancer, avec un accent particulier sur le PGL. En outre, nous nous penchons sur l'intelligence artificielle (IA) dans l'imagerie médicale et explorons l'application de la radiomique dans l'imagerie du cancer. Nous mettons en lumière une étude fondamentale menée par une ancienne étudiante en doctorat, Caterina Facchin, dans notre laboratoire, qui sert de pierre angulaire à notre recherche. Utilisant un modèle murin de tumeurs PGL, l'étude a employé

la co-registration PET/CT/UUDI pour examiner la dynamique des tumeurs Sdhb-/-. Les résultats ont révélé une réponse initiale au traitement par le sunitinib, inhibant efficacement la croissance tumorale et réduisant l'absorption du FDG au cours des premières semaines (W1-2). Cependant, l'imagerie ultérieure a indiqué un échappement au traitement par le sunitinib, marqué par une augmentation de la captation du FDG à W3 et une reprise de la croissance tumorale et du développement vasculaire à W4-5. L'étude a notamment identifié une concentration de vaisseaux sanguins dans les régions tumorales actives, consommatrices de sucre, avec un volume accru pendant la période d'échappement au sunitinib, ce qui suggère une adaptation dynamique de la vascularisation tumorale. Les changements précoces dans la glycolyse totale de la lésion et la longueur maximale des vaisseaux à W1 se sont révélés être des indicateurs prédictifs cruciaux de la résistance au sunitinib, offrant des indications précieuses sur les marqueurs potentiels de la résistance au traitement [69].

Chapitre 3: Les données de cette thèse proviennent d'expériences menées par un ancien candidat au doctorat au sein de notre équipe de recherche, détaillées dans [69]. Vingt-sept souris ont été implantées avec des PGLs déficientes en sous-unité B de la succinate déshydrogénase ($Sdhb^{-/-}$) après avoir obtenu l'approbation sous le numéro de référence 16-098. Les souris porteuses de tumeurs $Sdhb^{-/-}$ ont été divisées au hasard en deux groupes : CON et SUNI, le groupe SUNI recevant le médicament antiangiogénique sunitinib (50 mg/kg/jour) pendant 6 semaines. Dans le groupe SUNI, huit souris ont été affectées à la formation et onze à la validation. Le groupe de formation, composé de 16 souris (8 CON et 8 SUNI), a fait l'objet d'une surveillance hebdomadaire des tumeurs à l'aide de l'instrument PETRUS. PETRUS capture simultanément PET/CT/UUDI [179].

Chapitre 4: Ce chapitre explore les principaux résultats et méthodologies présentés dans l'article "Machine Learning of Multi-Modal Tumor Imaging Reveals Trajectories of Response to Precision Treatment". Dans cette étude, nous utilisons une combinaison d'analyse de regroupement hiérarchique (HCA) et de classificateurs d'ML supervisé pour identifier les différentes étapes de la progression de la tumeur et la réponse des PGL au sunitinib ou aux traitements fictifs. Nous utilisons un ensemble limité de caractéristiques vasculaires, moléculaires et anatomiques élaborées longitudinalement et interprétées directement sur le plan biologique. Étant donné l'existence de plusieurs classificateurs ML classiques avec des modèles simplifiés adaptés aux petites bases de données précliniques comme la nôtre, nous explorons et évaluons plusieurs classificateurs afin de déterminer le plus efficace pour identifier les réponses au traitement par le sunitinib dans les PGL en utilisant des descripteurs multimodaux. Le classificateur sélectionné, sur la base d'une performance optimale, est ensuite utilisé pour la classification généralisée des stades de progression de la tumeur. L'amalgame de ces stades tout au long de la durée des traitements anti-angiogéniques ou des traitements fictifs conduit à l'identification de trajectoires dans l'évolution de la tumeur. De manière remarquable, sans horodatage explicite de la durée du traitement, l'algorithme ML, utilisant des caractéristiques d'imagerie multimodales multiparamétriques, a réussi à identifier des groupes en corrélation avec la progression de la maladie et la réponse au sunitinib.

Dans le groupe traité par simulacre, deux stades de réponse au traitement sont identi-

fiés : Ac et Cc. Ac représente un stade précoce caractérisé par des tumeurs petites et peu développées, une faible vascularisation et une captation hétérogène du FDG, tandis que Cc indique un stade avancé avec des tumeurs de grande taille, des vaisseaux bien développés et une captation élevée et relativement uniforme du FDG, ressemblant à un cancer en phase terminale. Les souris passent rapidement, généralement en trois semaines, du groupe Ac au groupe Cc.

Dans le groupe traité au sunitinib, quatre stades de réponse au traitement sont identifiés : At et Ct, significativement similaires à Ac et Cc, et deux stades tumoraux intermédiaires distinctifs - B1t et B2t - qui n'ont pas été observés dans le groupe traité par sham. B1t comprend des tumeurs de petite taille avec une vascularisation modérée et une hétérogénéité dans la distribution de l'absorption du glucose, tandis que B2t comprend des tumeurs de volume et de vascularisation modérés, avec une faible hétérogénéité dans la distribution de l'absorption du glucose. Ces stades révèlent les effets du sunitinib sur les tumeurs PGL, l'importance des caractéristiques vasculaires étant soulignée par leur absence lorsque les caractéristiques vasculaires dérivées de l'échographie ultrarapide sont exclues de l'analyse. Les tumeurs peuvent passer d'un groupe à l'autre au fil du temps, ce qui indique des trajectoires dans l'évolution de la tumeur liées à la réponse ou à l'évasion du traitement. Certaines tumeurs traitées au sunitinib ont montré une progression similaire à celle des tumeurs traitées par sham, ce qui suggère que les souris entrant dans le groupe Ct au stade avancé pourraient avoir échappé à l'impact prévu du traitement au sunitinib.

En résumé, nos résultats soulignent non seulement la puissance de la ML non supervisée dans la caractérisation de la dynamique tumorale, mais éclairent également l'impact nuancé du traitement anti-angiogénique, en particulier le sunitinib, sur les aspects vasculaires et métaboliques des tumeurs PGL.

Chapitre 5 Dans ce chapitre, nous poursuivons nos recherches sur la dynamique de la réponse au traitement du paragangliome, en nous appuyant sur nos travaux antérieurs qui ont permis d'identifier des stades de réponse distincts dans un modèle de souris traitées au sunitinib. L'accent est maintenant mis sur l'exploration de l'hypothèse de sous-régions tumorales potentielles qui pourraient avoir une valeur prédictive de la réponse au traitement. Les images TEP dynamiques, composées de 31 images temporelles consécutives provenant de 8 souris à sept moments distincts avant le traitement et chaque semaine pendant le traitement, ainsi que les images 3D d'imagerie ultrasonore Doppler (UUDI), ont constitué les données d'entrée de cette étude. L'algorithme K-means avec des valeurs k optimisées a été appliqué pour dériver des régions métaboliques distinctes pour chaque tumeur indépendamment. Les supervoxels délimitant chaque sous-région ont été générés en calculant la moyenne des valeurs TEP dans la sous-région et en extrayant les caractéristiques métaboliques et vasculaires spécifiques des voxels correspondants. Les supervoxels résultants ont été combinés pour le partitionnement intra-tumoral, et l'analyse de regroupement hiérarchique (HCA) a été employée pour identifier les sous-régions communes dans la population. Ensuite, un volume 3D avec des sous-régions étiquetées pour chaque tumeur a été généré, servant de résultat à l'étude. Les images TEP et UUDI, ainsi que le volume étiqueté, ont ensuite été introduits dans le modèle 3D-UNet pour l'entraînement d'un modèle supervisé.

Notre examen a permis d'identifier quatre sous-régions distinctes au sein de la tumeur (r1, r2, r3 et r4), chacune présentant des caractéristiques métaboliques et vasculaires uniques. Notamment, la région r1 était principalement présente au stade avancé C, intermédiaire au stade B2, faible au stade B1 et absente au stade A. Par conséquent, la prévalence de la région r1, caractérisée par des conditions métaboliques et vasculaires accrues, apparaît comme un facteur prédictif potentiel de la résistance au traitement. À l'inverse, la région r3, caractérisée par une faible activité métabolique et vasculaire, était prédominante au stade A, moins répandue aux stades B1 et B2, et absente au stade C, ce qui indique une association avec une réponse favorable au traitement. Ces résultats suggèrent que les sous-régions r1 et/ou r3 pourraient potentiellement servir de biomarqueurs pour prédire la réponse des PPGL au traitement par le sunitinib.

Chapitre 6 Dans ce chapitre, nous explorons la radiomique dans les tumeurs du phéochromocytome et du paragangliome (PGL), avec une double approche, chacune se concentrant sur des objectifs distincts mais interconnectés. Tout d'abord, nous extrayons des caractéristiques radiomiques à partir d'images TEP, TDM et UUDI co-registrées. Cette initiative vise non seulement à valider la reproductibilité des stades de réponse au traitement identifiés, mais aussi à examiner la corrélation entre ces signatures radiomiques et l'efficacité du traitement des tumeurs PGL. Dans la phase initiale du projet, le programme SERA apparaît comme un outil crucial, offrant un accès à un riche répertoire de 487 caractéristiques radiomiques provenant de chaque modalité, à savoir CT, PET et UUDI. Le test méticuleux de paramètres tels que la discrétisation, la taille du voxel et la méthode d'interpolation est systématiquement entrepris pour discerner la configuration la plus robuste. Cette configuration, identifiée à travers une multitude de combinaisons, devient le pivot des analyses ultérieures. L'évaluation approfondie de la reproductibilité des caractéristiques se fait par le biais de mesures statistiques, à savoir la corrélation intra-classe (ICC) et le coefficient de corrélation de concordance (CCC). Ces mesures classent les caractéristiques radiomiques en groupes sur la base de leurs seuils de reproductibilité, ce qui permet de mieux comprendre leur fiabilité dans différentes configurations d'imagerie. La redondance au sein des caractéristiques est traitée au moyen d'une matrice de corrélation complète, où le coefficient de corrélation de Spearman sert d'arbitre. Les caractéristiques fortement corrélées sont identifiées et considérées comme redondantes, ce qui ouvre la voie à un processus de sélection affiné. La rationalisation de l'ensemble des caractéristiques se poursuit par l'élimination de celles dont la variance est minimale, comme l'indique un coefficient de variation inférieur à 0,3. Ce processus judicieux de réduction des caractéristiques permet d'obtenir une sélection de caractéristiques radiomiques informatives et non redondantes, susceptibles d'offrir un aperçu nuancé de la dynamique tumorale du PGL et de la réponse au traitement. Nous avons pu reproduire nos quatre étapes de réponse au traitement, mais cette fois avec des caractéristiques radiomiques.

La deuxième facette du projet se concentre sur des régions spécifiques, r1 et r3, reconnues pour leur corrélation avec les stades de réponse au traitement. Les caractéristiques radiomiques de ces sous-régions sont extraites indépendamment à l'aide du programme SERA. Le processus ultérieur de réduction des caractéristiques appliqué à chaque sous-région vise à distiller des informations clés. L'identification de caractéristiques communes entre r1 et r3 ouvre une nouvelle dimension d'exploration. Ces caractéristiques communes,

au nombre de six au total, sont soumises à des tests rigoureux pour détecter les différences significatives, révélant ainsi leur potentiel en tant que marqueurs. Notamment, cinq de ces caractéristiques radiomiques sont prometteuses en tant que prédicteurs de la réponse au traitement, dévoilant une couche de granularité qui peut améliorer de manière significative notre compréhension du comportement des tumeurs PGL dans différents scénarios de traitement.

Chapitre 7: Les chapitres 4 et 5 de la thèse présentent deux approches distinctes d'apprentissage machine (ML) pour délimiter les schémas de réponse au traitement dans les modèles murins de paragangliome (PGL). La première méthode se concentre sur les caractéristiques vasculaires, métaboliques et morphologiques, tandis que la seconde identifie les sous-régions tumorales critiques pour prédire les étapes de la réponse au traitement. Validées dans deux études fondamentales, ces approches révèlent des stades distincts de réponse au traitement, soulignant l'interdépendance des caractéristiques métaboliques, vasculaires et morphologiques. Les résultats soulignent le potentiel d'une approche multimodale, qui permet de comprendre les changements dynamiques survenant au cours du traitement.

La première étude catégorise trois stades de réponse au traitement (A, B1/B2, C) chez les souris PGL, soulignant l'importance des caractéristiques métaboliques, vasculaires et morphologiques dans la caractérisation précise des stades. La deuxième étude identifie quatre sous-régions (r1-r4), en mettant l'accent sur les régions r1 et r3 en tant que biomarqueurs potentiels de la résistance au traitement et de la réponse favorable, respectivement. Il s'agit d'une avancée substantielle dans la prédiction des résultats du traitement et dans l'adaptation de stratégies thérapeutiques efficaces pour le phéochromocytome et le paragangliome.

La recherche souligne l'importance de l'apprentissage automatique dans l'extraction des caractéristiques des images pour prédire la réponse au traitement. Malgré la petite taille de l'échantillon, la base de données robuste de l'étude longitudinale renforce la validité des résultats. La cohérence avec 8 souris partageant la même origine tumorale donne un aperçu cohérent de la dynamique de la réponse au traitement.

Pour l'avenir, les résultats ouvrent des pistes pour la médecine de précision, où l'apprentissage automatique peut affiner les stratégies de traitement sur la base de caractéristiques moléculaires ou vasculaires spécifiques. Les études futures pourraient étendre ces méthodologies à des cohortes plus importantes, intégrant diverses modalités et types de tumeurs. La nature longitudinale de l'étude encourage des examens plus approfondis au fil du temps, favorisant une compréhension globale de la dynamique de la réponse au traitement. En conclusion, la thèse met en évidence le potentiel de la combinaison de l'apprentissage automatique avec un accent sur les cibles thérapeutiques, offrant des perspectives pour la poursuite de la recherche et la mise en œuvre clinique dans la médecine de précision.

References

[1] Jing-Wen Bai, Si-Qi Qiu, and Guo-Jun Zhang. "Molecular and functional imaging in cancer-targeted therapy: Current applications and future directions". In: *Signal Transduction and Targeted Therapy* 8.1 (2023), p. 89.

[2] Martina Sollini et al. "Artificial intelligence and hybrid imaging: the best match for personalized medicine in oncology". In: *European journal of hybrid imaging* 4.1 (2020), pp. 1–22.

[3] Dow-Mu Koh et al. "Artificial intelligence and machine learning in cancer imaging". In: *Communications Medicine* 2.1 (2022), p. 133.

[4] Song Wu et al. "Evaluating intrinsic and non-intrinsic cancer risk factors". In: *Nature communications* 9.1 (2018), p. 3490.

[5] Joshua D Schiffman, Paul G Fisher, and Peter Gibbs. "Early detection of cancer: past, present, and future". In: *American Society of Clinical Oncology Educational Book* 35.1 (2015), pp. 57–65.

[6] OFFICE FOR NATIONAL STATISTICS. *CANCER SURVIVAL IN ENGLAND: Adult, Stage at Diagnosis and Childhood-Patients Followed Up... to 2018*. DANDY BOOKSELLERS Limited, 2019.

[7] Douglas Hanahan and Robert A Weinberg. "Hallmarks of cancer: the next generation". In: *cell* 144.5 (2011), pp. 646–674.

[8] Sergei I Grivennikov, Florian R Greten, and Michael Karin. "Immunity, inflammation, and cancer". In: *Cell* 140.6 (2010), pp. 883–899.

[9] Annalisa Del Prete et al. "Leukocyte trafficking in tumor microenvironment". In: *Current opinion in pharmacology* 35 (2017), pp. 40–47.

[10] Valerie LeBleu. "Imaging the tumor microenvironment". In: *Cancer journal (Sudbury, Mass.)* 21.3 (2015), p. 174.

[11] Kirill V Korneev et al. "TLR-signaling and proinflammatory cytokines as drivers of tumorigenesis". In: *Cytokine* 89 (2017), pp. 127–135.

[12] Peter Vaupel and Arnulf Mayer. "Hypoxia in tumors: pathogenesis-related classification, characterization of hypoxia subtypes, and associated biological and clinical implications". In: *Oxygen transport to tissue XXXVI* (2014), pp. 19–24.

[13] Christine Feig et al. “Targeting CXCL12 from FAP-expressing carcinoma-associated fibroblasts synergizes with anti–PD-L1 immunotherapy in pancreatic cancer”. In: *Proceedings of the National Academy of Sciences* 110.50 (2013), pp. 20212–20217.

[14] Judith Favier et al. “Rationale for anti-angiogenic therapy in pheochromocytoma and paraganglioma”. In: *Endocrine pathology* 23 (2012), pp. 34–42.

[15] Patricia J Keely. “Mechanisms by which the extracellular matrix and integrin signaling act to regulate the switch between tumor suppression and tumor promotion”. In: *Journal of mammary gland biology and neoplasia* 16 (2011), pp. 205–219.

[16] John D Gordan and M Celeste Simon. “Hypoxia-inducible factors: central regulators of the tumor phenotype”. In: *Current opinion in genetics & development* 17.1 (2007), pp. 71–77.

[17] Paolo E Porporato et al. “Anticancer targets in the glycolytic metabolism of tumors: a comprehensive review”. In: *Frontiers in pharmacology* 2 (2011), p. 49.

[18] Matthew G Vander Heiden, Lewis C Cantley, and Craig B Thompson. “Understanding the Warburg effect: the metabolic requirements of cell proliferation”. In: *science* 324.5930 (2009), pp. 1029–1033.

[19] Judith Favier et al. “Angiogenesis and vascular architecture in pheochromocytomas: distinctive traits in malignant tumors”. In: *The American journal of pathology* 161.4 (2002), pp. 1235–1246.

[20] Nako Maishi et al. “Tumor endothelial heterogeneity in cancer progression”. In: *Cancers* 11.10 (2019), p. 1511.

[21] Janice A Nagy et al. “Heterogeneity of the tumor vasculature”. In: *Seminars in thrombosis and hemostasis*. Vol. 36. 03. © Thieme Medical Publishers. 2010, pp. 321–331.

[22] William R Wilson and Michael P Hay. “Targeting hypoxia in cancer therapy”. In: *Nature Reviews Cancer* 11.6 (2011), pp. 393–410.

[23] Alfred King-yin Lam. “Update on adrenal tumours in 2017 World Health Organization (WHO) of endocrine tumours”. In: *Endocrine pathology* 28 (2017), pp. 213–227.

[24] Jacques WM Lenders et al. “Pheochromocytoma and paraganglioma: an endocrine society clinical practice guideline”. In: *The Journal of Clinical Endocrinology & Metabolism* 99.6 (2014), pp. 1915–1942.

[25] Montserrat Ayala-Ramirez et al. “Treatment with sunitinib for patients with progressive metastatic pheochromocytomas and sympathetic paragangliomas”. In: *The Journal of Clinical Endocrinology & Metabolism* 97.11 (2012), pp. 4040–4050.

[26] Oksana Hamidi et al. “Malignant pheochromocytoma and paraganglioma: 272 patients over 55 years”. In: *The Journal of Clinical Endocrinology & Metabolism* 102.9 (2017), pp. 3296–3305.

[27] Sina Jasim et al. “Phase II trial of pazopanib in advanced/progressive malignant pheochromocytoma and paraganglioma”. In: *Endocrine* 57 (2017), pp. 220–225.

[28] Paola Jimenez et al. “Treatment for malignant pheochromocytomas and paragangliomas: 5 years of progress”. In: *Current oncology reports* 19 (2017), pp. 1–12.

[29] Alejandro Roman-Gonzalez et al. “Impact of surgical resection of the primary tumor on overall survival in patients with metastatic pheochromocytoma or sympathetic paraganglioma”. In: *Annals of surgery* 268.1 (2018), pp. 172–178.

[30] David Taıeb et al. “Modern nuclear imaging for paragangliomas: beyond SPECT”. In: *Journal of Nuclear Medicine* 53.2 (2012), pp. 264–274.

[31] Henri JLM Timmers et al. “Superiority of fluorodeoxyglucose positron emission tomography to other functional imaging techniques in the evaluation of metastatic SDHB-associated pheochromocytoma and paraganglioma”. In: *Journal of Clinical Oncology* 25.16 (2007), pp. 2262–2269.

[32] Laura Remacha et al. “Gain-of-function mutations in DNMT3A in patients with paraganglioma”. In: *Genetics in Medicine* 20.12 (2018), pp. 1644–1651.

[33] Laura Remacha et al. “Recurrent germline DLST mutations in individuals with multiple pheochromocytomas and paragangliomas”. In: *The American Journal of Human Genetics* 104.4 (2019), pp. 651–664.

[34] M Lenglet et al. “New lessons from an old gene: complex splicing and novel cryptic exon in VHL gene cause erythrocytosis and VHL disease”. In: *Blood* 132.5 (2018), pp. 469–83.

[35] Maria Currás-Freixes et al. “PheoSeq: a targeted next-generation sequencing assay for pheochromocytoma and paraganglioma diagnostics”. In: *The Journal of Molecular Diagnostics* 19.4 (2017), pp. 575–588.

[36] Alessio Giubellino et al. “Urinary bladder paragangliomas: How Immunohistochemistry can assist to identify patients with SDHB germ line and somatic mutations”. In: *The American journal of surgical pathology* 39.11 (2015), p. 1488.

[37] Hartmut PH Neumann et al. “Germ-line mutations in nonsyndromic pheochromocytoma”. In: *New England Journal of Medicine* 346.19 (2002), pp. 1459–1466.

[38] Nelly Burnichon et al. “Somatic NF1 inactivation is a frequent event in sporadic pheochromocytoma”. In: *Human molecular genetics* 21.26 (2012), pp. 5397–5405.

[39] Nelly Burnichon et al. “MAX mutations cause hereditary and sporadic pheochromocytoma and paraganglioma”. In: *Clinical cancer research* 18.10 (2012), pp. 2828–2837.

[40] Bruna Calsina et al. “Role of MDH2 pathogenic variant in pheochromocytoma and paraganglioma patients”. In: *Genetics in Medicine* 20.12 (2018), pp. 1652–1662.

[41] Laura Remacha et al. “Targeted exome sequencing of Krebs cycle genes reveals candidate cancer–predisposing mutations in pheochromocytomas and paragangliomas”. In: *Clinical Cancer Research* 23.20 (2017), pp. 6315–6324.

[42] Alexandre Buffet et al. “Germline mutations in the mitochondrial 2-oxoglutarate/malate carrier SLC25A11 gene confer a predisposition to metastatic paragangliomas”. In: *Cancer Research* 78.8 (2018), pp. 1914–1922.

[43] Rodrigo A Toledo et al. “Recurrent mutations of chromatin-remodeling genes and kinase receptors in pheochromocytomas and paragangliomas”. In: *Clinical Cancer Research* 22.9 (2016), pp. 2301–2310.

[44] Laurence Amar et al. “Genetic testing in pheochromocytoma or functional paraganglioma”. In: *Journal of Clinical Oncology* 23.34 (2005), pp. 8812–8818.

[45] Anne-Paule Gimenez-Roqueplo et al. “Mutations in the SDHB gene are associated with extra-adrenal and/or malignant phaeochromocytomas”. In: *Cancer research* 63.17 (2003), pp. 5615–5621.

[46] Nelly Burnichon et al. “The succinate dehydrogenase genetic testing in a large prospective series of patients with paragangliomas”. In: *The Journal of Clinical Endocrinology & Metabolism* 94.8 (2009), pp. 2817–2827.

[47] Laurence Amar et al. “Succinate dehydrogenase B gene mutations predict survival in patients with malignant pheochromocytomas or paragangliomas”. In: *The Journal of Clinical Endocrinology & Metabolism* 92.10 (2007), pp. 3822–3828.

[48] Kathryn S King et al. “Metastatic pheochromocytoma/paraganglioma related to primary tumor development in childhood or adolescence: significant link to SDHB mutations”. In: *Journal of Clinical Oncology* 29.31 (2011), p. 4137.

[49] Segolene Hescot et al. “Prognosis of malignant pheochromocytoma and paraganglioma (MAPP-PronO study): a European network for the study of adrenal tumors retrospective study”. In: *The Journal of Clinical Endocrinology & Metabolism* 104.6 (2019), pp. 2367–2374.

[50] Alexandre Buffet et al. “Positive impact of genetic test on the management and outcome of patients with paraganglioma and/or pheochromocytoma”. In: *The Journal of Clinical Endocrinology & Metabolism* 104.4 (2019), pp. 1109–1118.

[51] Judith Favier et al. “Hereditary paraganglioma/pheochromocytoma and inherited succinate dehydrogenase deficiency”. In: *Hormone Research in Paediatrics* 63.4 (2005), pp. 171–179.

[52] Keiichi Kondo et al. “Inhibition of HIF is necessary for tumor suppression by the von Hippel-Lindau protein”. In: *Cancer cell* 1.3 (2002), pp. 237–246.

[53] Sandip Basu et al. “The basic principles of FDG-PET/CT imaging”. In: *PET clinics* 9.4 (2014), pp. 355–370.

[54] Alejandro Sanchez-Crespo. “Comparison of Gallium-68 and Fluorine-18 imaging characteristics in positron emission tomography”. In: *Applied Radiation and Isotopes* 76 (2013), pp. 55–62.

[55] Redha-alla Abdo et al. “Quantification of hypoxia in human glioblastoma using PET with 18F-FMISO”. In: *Nuclear Medicine and Molecular Imaging* 55 (2021), pp. 107–115.

[56] M Peck et al. “Applications of PET imaging with the proliferation marker [18F]-FLT”. In: *The quarterly journal of nuclear medicine and molecular imaging: official publication of the Italian Association of Nuclear Medicine (AIMN)[and] the International Association of Radiopharmacology (IAR),[and] Section of the Society of...* 59.1 (2015), p. 95.

[57] Peter Laverman et al. “Fluorinated amino acids for tumour imaging with positron emission tomography”. In: *European journal of nuclear medicine and molecular imaging* 29 (2002), pp. 681–690.

[58] Martin A Lodge et al. “Reproducibility of tumor blood flow quantification with 15O-water PET”. In: *Journal of Nuclear Medicine* 49.10 (2008), pp. 1620–1627.

[59] Weijun Wei et al. “ImmunoPET: concept, design, and applications”. In: *Chemical reviews* 120.8 (2020), pp. 3787–3851.

[60] Thomas E Nichols et al. “Best practices in data analysis and sharing in neuroimaging using MRI”. In: *Nature neuroscience* 20.3 (2017), pp. 299–303.

[61] Nicola K Dinsdale et al. “Learning patterns of the ageing brain in MRI using deep convolutional networks”. In: *NeuroImage* 224 (2021), p. 117401.

[62] Andrew Hong et al. “Reliability and accuracy of MRI in orthopedics: a survey of its use and perceived limitations”. In: *Clinical Medicine Insights: Arthritis and Musculoskeletal Disorders* 12 (2019), p. 1179544119872972.

[63] Clyde A Helms et al. *Musculoskeletal mri e-book*. Elsevier Health Sciences, 2008.

[64] Jan Bogaert et al. *Clinical cardiac MRI*. Springer Science & Business Media, 2012.

[65] Felipe Sanchez Tijmes et al. “Cardiac MRI assessment of nonischemic myocardial inflammation: state of the art review and update on myocarditis associated with COVID-19 vaccination”. In: *Radiology: Cardiothoracic Imaging* 3.6 (2021), e210252.

[66] Mickael Tanter and Mathias Fink. “Ultrafast imaging in biomedical ultrasound”. In: *IEEE transactions on ultrasonics, ferroelectrics, and frequency control* 61.1 (2014), pp. 102–119.

[67] Jean Provost et al. “3-D ultrafast Doppler imaging applied to the noninvasive mapping of blood vessels in vivo”. In: *IEEE transactions on ultrasonics, ferroelectrics, and frequency control* 62.8 (2015), pp. 1467–1472.

[68] John M Hudson et al. “Dynamic contrast enhanced ultrasound for therapy monitoring”. In: *European journal of radiology* 84.9 (2015), pp. 1650–1657.

[69] Caterina Facchin et al. “Concurrent imaging of vascularization and metabolism in a mouse model of paraganglioma under anti-angiogenic treatment”. In: *Theranostics* 10.8 (2020), p. 3518.

[70] Thomas E Yankeelov, Richard G Abramson, and C Chad Quarles. "Quantitative multimodality imaging in cancer research and therapy". In: *Nature Reviews Clinical Oncology* 11.11 (2014), pp. 670–680.

[71] Haroon Sheikh, Corien Prins, and Erik Schrijvers. "Artificial Intelligence: Definition and Background". In: *Mission AI: The New System Technology*. Springer, 2023, pp. 15–41.

[72] Issam El Naqa and Martin J Murphy. *What is machine learning?* Springer, 2015.

[73] Leo Breiman. "Random forests". In: *Machine learning* 45 (2001), pp. 5–32.

[74] Carolin Strobl et al. "Conditional variable importance for random forests". In: *BMC bioinformatics* 9 (2008), pp. 1–11.

[75] Jehad Ali et al. "Random forests and decision trees". In: *International Journal of Computer Science Issues (IJCSI)* 9.5 (2012), p. 272.

[76] José Augusto Cadena Moreano and NBLS Palomino. "Global facial recognition using gabor wavelet, support vector machines and 3d face models". In: *Journal of Advances in Information Technology* 11.3 (2020).

[77] R Vijayarajeswari et al. "Classification of mammogram for early detection of breast cancer using SVM classifier and Hough transform". In: *Measurement* 146 (2019), pp. 800–805.

[78] Essam H Houssein et al. "A hybrid barnacles mating optimizer algorithm with support vector machines for gene selection of microarray cancer classification". In: *IEEE Access* 9 (2021), pp. 64895–64905.

[79] S Krishnakumar and K Manivannan. "Effective segmentation and classification of brain tumor using rough K means algorithm and multi kernel SVM in MR images". In: *Journal of Ambient Intelligence and Humanized Computing* 12 (2021), pp. 6751–6760.

[80] Melvin Earl Maron and John Larry Kuhns. "On relevance, probabilistic indexing and information retrieval". In: *Journal of the ACM (JACM)* 7.3 (1960), pp. 216–244.

[81] Hongyi Gao, Xi Zeng, and Chunhua Yao. "Application of improved distributed naive Bayesian algorithms in text classification". In: *The Journal of Supercomputing* 75 (2019), pp. 5831–5847.

[82] Anjan Nikhil Repaka, Sai Deepak Ravikanti, and Ramya G Franklin. "Design and implementing heart disease prediction using naives Bayesian". In: *2019 3rd International conference on trends in electronics and informatics (ICOEI)*. IEEE. 2019, pp. 292–297.

[83] Pradeepa Bandara et al. "Crop recommendation system". In: *International Journal of Computer Applications* 975 (2020), p. 8887.

[84] Daniel Müllner. "Modern hierarchical, agglomerative clustering algorithms". In: *arXiv preprint arXiv:1109.2378* (2011).

[85] M Kuchaki Rafsanjani, Z Asghari Varzaneh, and N Emami Chukanlo. "A survey of hierarchical clustering algorithms". In: *The Journal of Mathematics and Computer Science* 5.3 (2012), pp. 229–240.

[86] Stuart Lloyd. "Least squares quantization in PCM". In: *IEEE transactions on information theory* 28.2 (1982), pp. 129–137.

[87] SM Aqil Burney and Humera Tariq. "K-means cluster analysis for image segmentation". In: *International Journal of Computer Applications* 96.4 (2014).

[88] Nameirakpam Dhanachandra, Khumanthem Manglem, and Yambem Jina Chanu. "Image segmentation using K-means clustering algorithm and subtractive clustering algorithm". In: *Procedia Computer Science* 54 (2015), pp. 764–771.

[89] Kayalvily Tabianan, Shubashini Velu, and Vinayakumar Ravi. "K-means clustering approach for intelligent customer segmentation using customer purchase behavior data". In: *Sustainability* 14.12 (2022), p. 7243.

[90] Rakesh Chandra Balabantaray, Chandrali Sarma, and Monica Jha. "Document clustering using k-means and k-medoids". In: *arXiv preprint arXiv:1502.07938* (2015).

[91] Semi-Supervised Learning. "Semi-Supervised Learning". In: *CSZ2006. html* (2006).

[92] Richard S Sutton and Andrew G Barto. *Reinforcement learning: An introduction*. MIT press, 2018.

[93] Yann LeCun, Yoshua Bengio, and Geoffrey Hinton. "Deep learning". In: *nature* 521.7553 (2015), pp. 436–444.

[94] Ali Bou Nassif et al. "Speech recognition using deep neural networks: A systematic review". In: *IEEE access* 7 (2019), pp. 19143–19165.

[95] Ophir Gozes et al. "Rapid ai development cycle for the coronavirus (covid-19) pandemic: Initial results for automated detection & patient monitoring using deep learning ct image analysis". In: *arXiv preprint arXiv:2003.05037* (2020).

[96] Baris Turkbey and Masoom A Haider. "Artificial intelligence for automated cancer detection on prostate MRI: opportunities and ongoing challenges, from the AJR special series on AI applications". In: *American Journal of Roentgenology* 219.2 (2022), pp. 188–194.

[97] Feng Shi et al. "Review of artificial intelligence techniques in imaging data acquisition, segmentation, and diagnosis for COVID-19". In: *IEEE reviews in biomedical engineering* 14 (2020), pp. 4–15.

[98] Philippe Lambin et al. "Radiomics: extracting more information from medical images using advanced feature analysis". In: *European journal of cancer* 48.4 (2012), pp. 441–446.

[99] Robert J Gillies, Paul E Kinahan, and Hedvig Hricak. "Radiomics: images are more than pictures, they are data". In: *Radiology* 278.2 (2016), pp. 563–577.

[100] Hugo JWL Aerts et al. “Decoding tumour phenotype by noninvasive imaging using a quantitative radiomics approach”. In: *Nature communications* 5.1 (2014), p. 4006.

[101] Joshua D Shur et al. “Radiomics in oncology: a practical guide”. In: *Radiographics* 41.6 (2021), pp. 1717–1732.

[102] Bin Zhang et al. “Machine-learning based MRI radiomics models for early detection of radiation-induced brain injury in nasopharyngeal carcinoma”. In: *BMC cancer* 20 (2020), pp. 1–9.

[103] Dennis Mackin et al. “Measuring CT scanner variability of radiomics features”. In: *Investigative radiology* 50.11 (2015), p. 757.

[104] Camilla Scapicchio et al. “A deep look into radiomics”. In: *La radiologia medica* 126.10 (2021), pp. 1296–1311.

[105] Andreas Bannach et al. “Visual analytics for radiomics: Combining medical imaging with patient data for clinical research”. In: *2017 IEEE Workshop on Visual Analytics in Healthcare (VAHC)*. IEEE. 2017, pp. 84–91.

[106] David A Mankoff. “A definition of molecular imaging”. In: *The Journal of Nuclear Medicine* 48.6 (2007), 18N.

[107] Eugenia Floyd and Teresa M Mcshane. “Development and use of biomarkers in oncology drug development”. In: *Toxicologic pathology* 32.1_suppl (2004), pp. 106–115.

[108] AF Casy. “Applications of nuclear magnetic resonance spectroscopy in medicinal and pharmaceutical chemistry”. In: *Journal of Pharmaceutical Sciences* 56.9 (1967), pp. 1049–1063.

[109] David E Kuhl et al. “The Mark IV system for radionuclide computed tomography of the brain”. In: *Radiology* 121.2 (1976), pp. 405–413.

[110] Peter G Morris et al. “Human whole body line scan imaging by nuclear magnetic resonance”. In: *IEEE Transactions on Nuclear Science* 26.2 (1979), pp. 2817–2820.

[111] Roman P Legocki et al. “Bioluminescence in soybean root nodules: demonstration of a general approach to assay gene expression in vivo by using bacterial luciferase”. In: *Proceedings of the National Academy of Sciences* 83.23 (1986), pp. 9080–9084.

[112] Kyung A Kang et al. “Highly scattering optical system identification via frequency response analysis of NIR-TRS spectra”. In: *Annals of biomedical engineering* 22 (1994), pp. 240–252.

[113] Kenneth R Zasadny et al. “FDG-PET determination of metabolically active tumor volume and comparison with CT”. In: *Clinical positron imaging* 1.2 (1998), pp. 123–129.

[114] John A Viator et al. “Clinical testing of a photoacoustic probe for port wine stain depth determination”. In: *Lasers in Surgery and Medicine: The Official Journal of the American Society for Laser Medicine and Surgery* 30.2 (2002), pp. 141–148.

[115] Andrew M Smith, Michael C Mancini, and Shuming Nie. "Second window for in vivo imaging". In: *Nature nanotechnology* 4.11 (2009), pp. 710–711.

[116] Simone Maurea et al. "Diagnostic imaging in patients with paragangliomas. Computed tomography, magnetic resonance and MIBG scintigraphy comparison." In: *The quarterly journal of nuclear medicine: official publication of the Italian Association of Nuclear Medicine (AIMN)[and] the International Association of Radiopharmacology (IAR)* 40.4 (1996), pp. 365–371.

[117] Vittoria Rufini et al. "Comparison of 123I-MIBG SPECT-CT and 18F-DOPA PET-CT in the evaluation of patients with known or suspected recurrent paraganglioma". In: *Nuclear medicine communications* 32.7 (2011), pp. 575–582.

[118] Jay S Fonte et al. "False-negative 123I-MIBG SPECT is most commonly found in SDHB-related pheochromocytoma or paraganglioma with high frequency to develop metastatic disease". In: *Endocrine-related cancer* 19.1 (2012), p. 83.

[119] Dipti Rao et al. "Impact of 123I-MIBG scintigraphy on clinical decision-making in pheochromocytoma and paraganglioma". In: *The Journal of Clinical Endocrinology & Metabolism* 104.9 (2019), pp. 3812–3820.

[120] Henri JLM Timmers et al. "Comparison of 18F-fluoro-L-DOPA, 18F-fluoro-deoxyglucose, and 18F-fluorodopamine PET and 123I-MIBG scintigraphy in the localization of pheochromocytoma and paraganglioma". In: *The Journal of Clinical Endocrinology & Metabolism* 94.12 (2009), pp. 4757–4767.

[121] BRUCE H BRUNDAGE, STUART RICH, and DIMITRIOS SPIGOS. "Computed tomography of the heart and great vessels: present and future". In: *Annals of internal medicine* 101.6 (1984), pp. 801–809.

[122] Jana Cebulla et al. "Multiscale and multi-modality visualization of angiogenesis in a human breast cancer model". In: *Angiogenesis* 17 (2014), pp. 695–709.

[123] CA Cuenod and D Balvay. "Perfusion and vascular permeability: basic concepts and measurement in DCE-CT and DCE-MRI". In: *Diagnostic and interventional imaging* 94.12 (2013), pp. 1187–1204.

[124] JWM Lenders. "Biochemical diagnosis of pheochromocytoma and paraganglioma". In: *Annales d'endocrinologie*. Vol. 70. 3. Elsevier. 2009, pp. 161–165.

[125] Martin O Leach et al. "The assessment of antiangiogenic and antivascular therapies in early-stage clinical trials using magnetic resonance imaging: issues and recommendations". In: *British journal of cancer* 92.9 (2005), pp. 1599–1610.

[126] Yun-Zhi Dang et al. "High VEGFR1/2 expression levels are predictors of poor survival in patients with cervical cancer". In: *Medicine* 96.1 (2017).

[127] Minjian Zhao et al. "Expression of angiogenic growth factors VEGF, bFGF and ANG1 in colon cancer after bevacizumab treatment in vitro: A potential self-regulating mechanism". In: *Oncology reports* 37.1 (2017), pp. 601–607.

[128] Jianhua Zhou et al. “VEGFR2-targeted three-dimensional ultrasound imaging can predict responses to antiangiogenic therapy in preclinical models of colon cancer”. In: *Cancer research* 76.14 (2016), pp. 4081–4089.

[129] Suzanne C van Es et al. “89Zr-bevacizumab PET: potential early indicator of everolimus efficacy in patients with metastatic renal cell carcinoma”. In: *Journal of Nuclear Medicine* 58.6 (2017), pp. 905–910.

[130] Jürgen K Willmann et al. “US imaging of tumor angiogenesis with microbubbles targeted to vascular endothelial growth factor receptor type 2 in mice”. In: *Radiology* 246.2 (2008), pp. 508–518.

[131] Iain D Campbell and Martin J Humphries. “Integrin structure, activation, and interactions”. In: *Cold Spring Harbor perspectives in biology* 3.3 (2011), a004994.

[132] Oliver Schnell et al. “Imaging of integrin $\alpha v\beta 3$ expression in patients with malignant glioma by [18F] Galacto-RGD positron emission tomography”. In: *Neuro-oncology* 11.6 (2009), pp. 861–870.

[133] André Briguet et al. *Imagerie médicale à base de champs magnétiques et d’ultrasons*. Hermes-Lavoisier, 2014.

[134] PN Burns et al. “Ultrasonic Doppler studies of the breast.” In: *BRITISH JOURNAL OF RADIOLOGY*. Vol. 54. 642. BRITISH INST RADIOLOGY 36 PORTLAND PLACE, LONDON, ENGLAND W1N 4AT. 1981, pp. 549–550.

[135] Michael S Gee et al. “Doppler ultrasound imaging detects changes in tumor perfusion during antivascular therapy associated with vascular anatomic alterations”. In: *Cancer research* 61.7 (2001), pp. 2974–2982.

[136] Wei Tse Yang et al. “Correlation between color power Doppler sonographic measurement of breast tumor vasculature and immunohistochemical analysis of microvessel density for the quantitation of angiogenesis”. In: *Journal of ultrasound in medicine* 21.11 (2002), pp. 1227–1235.

[137] Alexandra Eichten et al. “Rapid decrease in tumor perfusion following VEGF blockade predicts long-term tumor growth inhibition in preclinical tumor models”. In: *Angiogenesis* 16 (2013), pp. 429–441.

[138] N Lassau et al. “Selection of an early biomarker for vascular normalization using dynamic contrast-enhanced ultrasonography to predict outcomes of metastatic patients treated with bevacizumab”. In: *Annals of Oncology* 27.10 (2016), pp. 1922–1928.

[139] CF Dietrich et al. “An EFSUMB introduction into Dynamic Contrast-Enhanced Ultrasound (DCE-US) for quantification of tumour perfusion”. In: *Ultraschall in der Medizin-European Journal of Ultrasound* (2012), pp. 344–351.

[140] Nathalie Lassau et al. “Validation of dynamic contrast-enhanced ultrasound in predicting outcomes of antiangiogenic therapy for solid tumors: the French multicenter support for innovative and expensive techniques study”. In: *Investigative radiology* 49.12 (2014), p. 794.

[141] Nathalie Lassau et al. “Standardization of dynamic contrast-enhanced ultrasound for the evaluation of antiangiogenic therapies: the French multicenter Support for Innovative and Expensive Techniques Study”. In: *Investigative radiology* 47.12 (2012), pp. 711–716.

[142] Rakesh K Jain. “Normalization of tumor vasculature: an emerging concept in antiangiogenic therapy”. In: *Science* 307.5706 (2005), pp. 58–62.

[143] RD Hunter. “World Health Organization (WHO) handbook for reporting results of cancer treatment”. In: *WHO, Geneva, Switzerland* (1979).

[144] Patrick Therasse et al. “New guidelines to evaluate the response to treatment in solid tumors”. In: *Journal of the National Cancer Institute* 92.3 (2000), pp. 205–216.

[145] Alejandro Forner et al. “Evaluation of tumor response after locoregional therapies in hepatocellular carcinoma: are response evaluation criteria in solid tumors reliable?” In: *Cancer* 115.3 (2009), pp. 616–623.

[146] Richard L Wahl et al. “From RECIST to PERCIST: evolving considerations for PET response criteria in solid tumors”. In: *Journal of nuclear medicine* 50.Suppl 1 (2009), 122S–150S.

[147] Gabriel Chartrand et al. “Deep learning: a primer for radiologists”. In: *Radiographics* 37.7 (2017), pp. 2113–2131.

[148] Jürgen Schmidhuber. “Deep learning in neural networks: An overview”. In: *Neural networks* 61 (2015), pp. 85–117.

[149] Marvin Minsky and Seymour A Papert. *Perceptrons, reissue of the 1988 expanded edition with a new foreword by Léon Bottou: an introduction to computational geometry*. MIT press, 2017.

[150] Martina Sollini et al. “Towards clinical application of image mining: a systematic review on artificial intelligence and radiomics”. In: *European journal of nuclear medicine and molecular imaging* 46 (2019), pp. 2656–2672.

[151] Wenya Linda Bi et al. “Artificial intelligence in cancer imaging: clinical challenges and applications”. In: *CA: a cancer journal for clinicians* 69.2 (2019), pp. 127–157.

[152] Martina Sollini, Francesco Bandera, and Margarita Kirienko. “Quantitative imaging biomarkers in nuclear medicine: from SUV to image mining studies. Highlights from annals of nuclear medicine 2018”. In: *European Journal of Nuclear Medicine and Molecular Imaging* 46.13 (2019), pp. 2737–2745.

[153] A Ibrahim et al. “Radiomics for precision medicine: Current challenges, future prospects, and the proposal of a new framework”. In: *Methods* 188 (2021), pp. 20–29.

[154] Shigao Huang et al. “Mining prognosis index of brain metastases using artificial intelligence”. In: *Cancers* 11.8 (2019), p. 1140.

[155] Stephen Baek et al. “Deep segmentation networks predict survival of non-small cell lung cancer”. In: *Scientific reports* 9.1 (2019), p. 17286.

[156] Yong Liu. “Application of artificial intelligence in clinical non-small cell lung cancer”. In: *Artificial Intelligence in Cancer* 1.1 (2020), pp. 19–30.

[157] Benjamin Q Huynh, Natasha Antropova, and Maryellen L Giger. “Comparison of breast DCE-MRI contrast time points for predicting response to neoadjuvant chemotherapy using deep convolutional neural network features with transfer learning”. In: *Medical imaging 2017: computer-aided diagnosis*. Vol. 10134. SPIE. 2017, pp. 207–213.

[158] Kenny H Cha et al. “Bladder cancer treatment response assessment in CT using radiomics with deep-learning”. In: *Scientific reports* 7.1 (2017), p. 8738.

[159] Michael Höckel et al. “Intratumoral pO2 predicts survival in advanced cancer of the uterine cervix”. In: *Radiotherapy and Oncology* 26.1 (1993), pp. 45–50.

[160] Zhaohai Yang, Laura H Tang, and David S Klimstra. “Effect of tumor heterogeneity on the assessment of Ki67 labeling index in well-differentiated neuroendocrine tumors metastatic to the liver: implications for prognostic stratification”. In: *The American journal of surgical pathology* 35.6 (2011), pp. 853–860.

[161] Rhea Chitalia et al. “Functional 4-D clustering for characterizing intratumor heterogeneity in dynamic imaging: evaluation in FDG PET as a prognostic biomarker for breast cancer”. In: *European journal of nuclear medicine and molecular imaging* 48 (2021), pp. 3990–4001.

[162] Janet F Eary et al. “Spatial heterogeneity in sarcoma 18F-FDG uptake as a predictor of patient outcome”. In: *Journal of Nuclear Medicine* 49.12 (2008), pp. 1973–1979.

[163] Jia Wu et al. “Robust intratumor partitioning to identify high-risk subregions in lung cancer: a pilot study”. In: *International Journal of Radiation Oncology* Biology* Physics* 95.5 (2016), pp. 1504–1512.

[164] Dmitry Cherezov et al. “Revealing tumor habitats from texture heterogeneity analysis for classification of lung cancer malignancy and aggressiveness”. In: *Scientific reports* 9.1 (2019), p. 4500.

[165] Hui Xu et al. “Subregional radiomics analysis of PET/CT imaging with intratumor partitioning: application to prognosis for nasopharyngeal carcinoma”. In: *Molecular Imaging and Biology* 22 (2020), pp. 1414–1426.

[166] Balaji Ganeshan et al. “Tumour heterogeneity in non-small cell lung carcinoma assessed by CT texture analysis: a potential marker of survival”. In: *European radiology* 22 (2012), pp. 796–802.

[167] Issam El Naqa et al. “Exploring feature-based approaches in PET images for predicting cancer treatment outcomes”. In: *Pattern recognition* 42.6 (2009), pp. 1162–1171.

[168] Fei Yang et al. “Temporal analysis of intratumoral metabolic heterogeneity characterized by textural features in cervical cancer”. In: *European journal of nuclear medicine and molecular imaging* 40 (2013), pp. 716–727.

[169] Gary JR Cook et al. "Are pretreatment 18F-FDG PET tumor textural features in non–small cell lung cancer associated with response and survival after chemoradiotherapy?" In: *Journal of nuclear medicine* 54.1 (2013), pp. 19–26.

[170] Hao Zhang et al. "Modeling pathologic response of esophageal cancer to chemoradiation therapy using spatial-temporal 18F-FDG PET features, clinical parameters, and demographics". In: *International Journal of Radiation Oncology* Biology* Physics* 88.1 (2014), pp. 195–203.

[171] Ukihide Tateishi et al. "Contrast-enhanced dynamic computed tomography for the evaluation of tumor angiogenesis in patients with lung carcinoma". In: *Cancer: Interdisciplinary International Journal of the American Cancer Society* 95.4 (2002), pp. 835–842.

[172] Chan Kyo Kim et al. "Neoangiogenesis and sinusoidal capillarization in hepatocellular carcinoma: correlation between dynamic CT and density of tumor microvessels". In: *Radiology* 237.2 (2005), pp. 529–534.

[173] Koichi Hayano et al. "Fractal analysis of contrast-enhanced CT images to predict survival of patients with hepatocellular carcinoma treated with sunitinib". In: *Digestive diseases and sciences* 59 (2014), pp. 1996–2003.

[174] Xiaoping Yi et al. "Radiomics improves efficiency for differentiating subclinical pheochromocytoma from lipid-poor adenoma: a predictive, preventive and personalized medical approach in adrenal incidentalomas". In: *EPMA Journal* 9 (2018), pp. 421–429.

[175] Xiaoping Yi et al. "Adrenal incidentaloma: machine learning-based quantitative texture analysis of unenhanced CT can effectively differentiate sPHEO from lipid-poor adrenal adenoma". In: *Journal of Cancer* 9.19 (2018), p. 3577.

[176] Catherine Ansquer et al. "Usefulness of FDG-PET/CT-based radiomics for the characterization and genetic orientation of pheochromocytomas before surgery". In: *Cancers* 12.9 (2020), p. 2424.

[177] Paul Workman et al. "Minimally invasive pharmacokinetic and pharmacodynamic technologies in hypothesis-testing clinical trials of innovative therapies". In: *Journal of the National Cancer Institute* 98.9 (2006), pp. 580–598.

[178] Nesrin Mansouri et al. "Machine learning of multi-modal tumor imaging reveals trajectories of response to precision treatment". In: *Cancers* 15.6 (2023), p. 1751.

[179] Jean Provost et al. "Simultaneous positron emission tomography and ultrafast ultrasound for hybrid molecular, anatomical and functional imaging". In: *Nature biomedical engineering* 2.2 (2018), pp. 85–94.

[180] Laura E Boucheron. *Object-and spatial-level quantitative analysis of multispectral histopathology images for detection and characterization of cancer*. University of California at Santa Barbara, 2008.

[181] Mailyn Perez-Liva et al. “Performance evaluation of the PET component of a hybrid PET/CT-ultrafast ultrasound imaging instrument”. In: *Physics in Medicine & Biology* 63.19 (2018), 19NT01.

[182] Adam M Alessio and Paul E Kinahan. “Improved quantitation for PET/CT image reconstruction with system modeling and anatomical priors”. In: *Medical physics* 33.11 (2006), pp. 4095–4103.

[183] Charlie Demené et al. “3-D longitudinal imaging of tumor angiogenesis in mice in vivo using ultrafast Doppler tomography”. In: *Ultrasound in Medicine & Biology* 45.5 (2019), pp. 1284–1296.

[184] Rafael Molina, Javier Mateos, and Aggelos K Katsaggelos. “Blind deconvolution using a variational approach to parameter, image, and blur estimation”. In: *IEEE Transactions on Image Processing* 15.12 (2006), pp. 3715–3727.

[185] Ingrid Wu et al. “Optimal definition of biological tumor volume using positron emission tomography in an animal model”. In: *EJNMMI research* 5 (2015), pp. 1–10.

[186] E Laffon et al. “Variability of average SUV from several hottest voxels is lower than that of SUVmax and SUVpeak”. In: *European radiology* 24 (2014), pp. 1964–1970.

[187] Alejandro F Frangi et al. “Multiscale vessel enhancement filtering”. In: *Medical Image Computing and Computer-Assisted Intervention—MICCAI’98: First International Conference Cambridge, MA, USA, October 11–13, 1998 Proceedings 1*. Springer. 1998, pp. 130–137.

[188] Danilo Babin et al. “Skeletonization method for vessel delineation of arteriovenous malformation”. In: *Computers in Biology and Medicine* 93 (2018), pp. 93–105.

[189] Danilo Babin et al. “Brain blood vessel segmentation using line-shaped profiles”. In: *Physics in Medicine & Biology* 58.22 (2013), p. 8041.

[190] Isabelle Guyon and André Elisseeff. “An introduction to variable and feature selection”. In: *Journal of machine learning research* 3.Mar (2003), pp. 1157–1182.

[191] Fanny Orlhac et al. “Tumor texture analysis in 18F-FDG PET: relationships between texture parameters, histogram indices, standardized uptake values, metabolic volumes, and total lesion glycolysis”. In: *Journal of Nuclear Medicine* 55.3 (2014), pp. 414–422.

[192] Robert Tibshirani, Guenther Walther, and Trevor Hastie. “Estimating the number of clusters in a data set via the gap statistic”. In: *Journal of the Royal Statistical Society: Series B (Statistical Methodology)* 63.2 (2001), pp. 411–423.

[193] Bernard L Welch. “The generalization of ‘STUDENT’S’problem when several different population varlances are involved”. In: *Biometrika* 34.1-2 (1947), pp. 28–35.

[194] Nitesh V Chawla et al. “SMOTE: synthetic minority over-sampling technique”. In: *Journal of artificial intelligence research* 16 (2002), pp. 321–357.

[195] Carolin Strobl et al. "Bias in random forest variable importance measures: Illustrations, sources and a solution". In: *BMC bioinformatics* 8.1 (2007), pp. 1–21.

[196] William H Kruskal and W Allen Wallis. "Use of ranks in one-criterion variance analysis". In: *Journal of the American statistical Association* 47.260 (1952), pp. 583–621.

[197] NHC Au et al. "Evaluation of immunohistochemical markers in non-small cell lung cancer by unsupervised hierarchical clustering analysis: a tissue microarray study of 284 cases and 18 markers". In: *The Journal of Pathology: A Journal of the Pathological Society of Great Britain and Ireland* 204.1 (2004), pp. 101–109.

[198] Sugi Lee et al. "A deep learning and similarity-based hierarchical clustering approach for pathological stage prediction of papillary renal cell carcinoma". In: *Computational and structural biotechnology journal* 18 (2020), pp. 2639–2646.

[199] Rivka R Colen et al. *Radiomics to predict response to pembrolizumab in patients with advanced rare cancers.* 2020.

[200] Laurène Ben Aim et al. "Targeted next-generation sequencing detects rare genetic events in pheochromocytoma and paraganglioma". In: *Journal of medical genetics* 56.8 (2019), pp. 513–520.

[201] Simon Lloyd et al. "British Skull Base Society clinical consensus document on management of head and neck paragangliomas". In: *Otolaryngology–Head and Neck Surgery* 163.3 (2020), pp. 400–409.

[202] Laurence Amar et al. "International consensus on initial screening and follow-up of asymptomatic SDHx mutation carriers". In: *Nature Reviews Endocrinology* 17.7 (2021), pp. 435–444.

[203] Masabumi Shibuya. "Vascular endothelial growth factor (VEGF) and its receptor (VEGFR) signaling in angiogenesis: a crucial target for anti-and pro-angiogenic therapies". In: *Genes & cancer* 2.12 (2011), pp. 1097–1105.

[204] Lindsey Oudijk et al. "Vascular pattern analysis for the prediction of clinical behaviour in pheochromocytomas and paragangliomas". In: *PloS one* 10.3 (2015), e0121361.

[205] Farshad Moradi Kashkooli et al. "A spatiotemporal multi-scale computational model for FDG PET imaging at different stages of tumor growth and angiogenesis". In: *Scientific reports* 12.1 (2022), p. 10062.

[206] Prateek Katiyar et al. "Spectral clustering predicts tumor tissue heterogeneity using dynamic 18F-FDG PET: a complement to the standard compartmental modeling approach". In: *Journal of Nuclear Medicine* 58.4 (2017), pp. 651–657.

[207] Saeed Ashrafinia. "Quantitative nuclear medicine imaging using advanced image reconstruction and radiomics". PhD thesis. The Johns Hopkins University, 2019.

[208] Afef Bouchouicha. "Radiomics of metastatic cell-clear renal cancer". PhD thesis. Sorbonne Paris Cité, 2018.